The Pennsylvania State University

The Graduate School

Department of Chemistry

PROTON-COUPLED ELECTRON TRANSFER REACTION IN SOYBEAN LIPOXYGENASE

A Thesis in

Chemistry

by

Elizabeth Hatcher

Submitted in Partial Fulfillment
of the Requirements
for the Degree of

Doctorate of Philosophy

December 2006

The thesis of Elizabeth Hatcher was reviewed and approved* by the following:

Sharon Hammes-Schiffer
Professor of Chemistry
Thesis Advisor
Chair of Committee

Mark Maroncelli
Professor of Chemistry

Michael Green
Assistant Professor of Chemistry

J. Martin Bollinger Jr.
Assistant Professor of Biochemistry and Molecular Biology
Assistant Professor of Chemistry

Ayusman Sen
Professor and Head of the Department of Chemistry

*Signatures are on file in the Graduate School

ABSTRACT

The proton-coupled electron transfer (PCET) reaction catalyzed by soybean lipoxygenase-1 is studied with a multistate continuum theory that represents the transferring hydrogen nucleus as a quantum mechanical wavefunction. Both classical and quantum mechanical treatments of the proton donor-acceptor vibrational motion are presented. The temperature dependence of the calculated rates and kinetic isotope effects is in agreement with the experimental data. The temperature dependence of the kinetic isotope effect is strongly influenced by the proton donor-acceptor distance. Thus, the proton donor-acceptor vibrational motion plays a vital role in facilitating the proton-coupled electron transfer reaction.

A general theoretical formulation for proton-coupled electron transfer reactions is presented. The solute is represented by a multistate valence bond model, and the active electrons and transferring proton(s) are treated quantum mechanically. This formulation enables the classical or quantum mechanical treatment of the proton donor-acceptor vibrational mode, as well as the dynamical treatment of the proton donor-acceptor mode and the solvent. Nonadiabatic rate expressions are presented for PCET reactions in a number of well-defined limits for both dielectric continuum and molecular representations of the environment. The dynamical rate expressions account for correlations between the fluctuations of the proton donor-acceptor distance and the nonadiabatic PCET coupling. The significance of the quantum and dynamical effects of the proton donor-acceptor mode is illustrated with applications to model PCET systems.

The dynamical aspects of a model proton-coupled electron transfer (PCET) reaction in solution are analyzed with molecular dynamics simulations. The rate constant for nonadiabatic PCET reactions is expressed in terms of a time-dependent probability flux correlation function. The impact of the proton donor-acceptor mode and solvent dynamics on the probability flux is examined. The analysis of PCET reactions is compared to previous analyses of single electron and proton transfer reactions.

Fundamental aspects of PCET reactions in solution are analyzed with molecular dynamics simulations for a series of model systems. The analysis addresses the impact of

the solvent reorganization energy, the proton donor-acceptor mode vibrational frequency, and the distance dependence of the nonadiabatic coupling on the dynamics of the reaction and the magnitude of the rate. The approximations underlying a previously derived analytical PCET rate expression are also investigated.

The dynamical behavior and the temperature dependence of the kinetic isotope effects are examined for the PCET reaction catalyzed by the enzyme soybean lipoxygenase. The calculations are based on a vibronically nonadiabatic formulation that includes the quantum mechanical effects of the active electrons and the transferring proton, as well as the motions of all atoms in the complete solvated enzyme system. The calculations reproduce the experimentally observed magnitude and temperature dependence of the kinetic isotope effect for the soybean lipoxygenase reaction without fitting any parameters directly to the experimental kinetic data.

TABLE OF CONTENTS

LIST OF FIGURES

LIST OF TABLES

ACKNOWLEDGEMENTS

I would like to acknowledge my research advisor, Prof. Sharon Hammes-Schiffer, for being a wonderful mentor. Her knowledge and passion for the science influenced me in so many ways. I appreciate the opportunity to work with her. Her advice and instruction has made me the scientist that I am today. I would also like to thank my committee members, Prof. Mark Maroncelli, Prof. Mike Green and Prof. Martin Bollinger, for their commitment to helping me when I needed it and support throughout my graduate career.

I would also like to acknowledge my research group, especially Dr. Alexander Soudackov for all of his insightful discussions and for his help with my research studies. He taught me so much and was so supportive with many of my decisions, so I would like to thank him for being so helpful.

I owe my family a debt of gratitude for being the motivating force behind my graduate career. Without their support, I would not have been able to get as far as I have. They taught me that determination is the key to a successful career, so I want to thank them all for everything.

Chapter 1

Introduction

Charge transfer processes are ubiquitous in nature. Proton-coupled electron transfer (PCET) reactions are a particular type of charge transfer process that involves the simultaneous transfer of an electron and a proton. PCET reactions play a significant role in biological systems such as DNA, photosynethic reaction centers, and enzymes. Lipoxygenase is an enzyme that breaks down fatty acid chains to ultimately form hydroperoxides. Lipoxygenase has recently become a topic of interest due to its medicinal relevance. This enzyme plays a role in the production of leukotrienes and lipoxins, which govern immune response; therefore, inhibition of this enzyme can aid in the treatment of diseases such as asthma and psoriasis.[1] Moreover, studies have shown that inhibitors of this enzyme can also be used in the prevention of cancer.[2-5]

Soybean lipoxygenase-1 is a non-heme iron metalloenzyme that is made up of approximately 840 amino acid residues. In our studies, we chose to model the soybean lipoxygenase-1 system because of the abundance of experimental data. The iron cofactor within the active site of the enzyme contains an iron surrounded by three histidine residues, an asparagine residue, an isoleucine residue, and a hydroxyl/water molecule. In the first step of the enzymatic reaction, a lone pair centered on the oxygen of the hydroxyl ligand abstracts the pro-*S* proton from the C11 carbon of linoleic acid, which is the natural substrate for soybean lipoxygenase-1, and π-electrons from the linoleic acid backbone reduce Fe(III). This step was determined to be a PCET mechanism based on a DFT orbital analysis[6] and a thermochemical analysis.[7]

Klinman and coworkers studied the kinetics of the PCET reaction in soybean lipoxygenase and determined that this step is the rate determining step at room

temperature. The deuterium kinetic isotope effect of the PCET step measured at 303K was determined to be 81, which is unusually large.[8] The deuterium kinetic isotope effect of the human form of lipoxygenase has also been determined to be very large.[9] Moreover, Klinman and co-workers observed a weak temperature dependence of the rates and kinetic isotope effects in the temperature range of 278K-313K.[8] With the combination of both of these observations, they hypothesized that hydrogen tunneling and a proton donor-acceptor vibrational mode play very important roles in this PCET mechanism. The proton donor-acceptor mode is the vibrational mode between the proton donor and proton acceptor. This vibrational mode has be shown to be very important in many proton transfer reactions. The significance of this mode is that it modulates the proton transfer barrier. The modulation of the proton transfer barrier facilitates the proton transfer reaction by affecting the overlap of the vibrational wavefunctions, thereby affecting the amount of tunneling.

Due to the importance of PCET reactions in biological systems, many theoretical studies have been performed to elucidate the physical and chemical nature of these types of reactions.[10-13] To accurately describe these types of reactions, many theoretical challenges must be surmounted. These theoretical challenges include the description of the quantum behavior of the light particles, the variability of timescales involved in these types of reactions, and the complex coupling among the transferring electron, the transferring proton, the solute and the solvent modes. PCET reactions are typically nonadiabatic because the electron transfer distance is usually fairly large and because the overlap of the proton nuclear wavefunctions is usually fairly small, leading to a small coupling between vibronic states.

The Hammes-Schiffer group previously developed a multistate continuum model to describe PCET systems.[14,15] In this formulation, the solvent is treated as a dielectric continuum using the frequency resolved cavity model (FRCM)[16] developed by Basilevsky and co-workers. The solute is treated quantum mechanically using a multistate empirical valence bond (EVB)[17] model, and the transferring hydrogen is treated quantum mechanically as a hydrogen vibrational wavefunction. This formulation is related to Marcus electron transfer theory[18], but includes an added dimension for the

proton transfer. Using the PCET formulation, reactant and product vibronic free energy surfaces are obtained as a function of the electron transfer and proton transfer collective solvent coordinates. These surfaces are used to calculate inputs for a nonadiabatic PCET rate expression that was previously developed in the Hammes-Schiffer group.[15] This nonadiabatic rate expression is based on Fermi's golden rule. Rates and kinetic isotope effects of PCET reactions can be calculated with this formulation. In addition, the temperature dependence of these rates and kinetic isotope effect can be calculated.

The goal of this thesis is to study the PCET mechanism in soybean lipoxygenase and elucidate the phenomenon that leads to the unusually large kinetic isotope effect and the weak temperature dependence of the rates and kinetic isotope effects. A more general goal of this thesis is to analyze the importance of the proton donor-acceptor vibrational mode, which was not included in the previous theoretical formulation, and to gain a better understanding of the dynamical aspects of this mode. A methodological aim of this thesis is the development of theoretical methods that include the proton donor-acceptor vibrational mode.[7,19]

The goal of the first part of this thesis is to use the multistate continuum model with the inclusion of the proton donor-acceptor mode to reproduce the temperature dependence of the rates and kinetic isotope effects of the PCET reaction in soybean lipoxygenase. The results of this method were used to understand the magnitude of the kinetic isotope effect and the importance of the proton donor-acceptor mode. The goal of the second part of this thesis is to develop an explicit solvent model that accounts for the dynamical correlations of the proton donor-acceptor mode and the solvent modes.[19] In the explicit solvent model, the dynamics of the proton donor-acceptor mode and the solvent/protein are included using molecular dynamics simulations. In addition, a dynamical nonadiabatic rate expression is derived for PCET reactions.[19] The goal of the third part of this thesis is to analyze model PCET systems using the dynamical PCET formulation. An investigation is performed to study how different aspects of PCET reactions affect the dynamical behavior. Furthermore, approximations made for the derivation of this formulation are tested with the model systems. Lastly, the PCET reaction in lipoxygenase is studied using the dynamical nonadiabatic PCET formulation

in conjunction with molecular dynamics simulations of the entire solvated enzyme. The dynamical behavior of the PCET reaction in lipoxygenase is examined. Moreover, the temperature dependence of the kinetic isotope effect is calculated from this formulation.

References

(1) Samuelsson, B.; Dahlen, S.-E.; Lindgren, J.; Rouzer, C. A.; Serhan, C. N. *Science* 1987, *237*, 1171.

(2) Steele, V. E.; Holmes, C. A.; Hawk, E. T.; Kopelovich, L.; Lubet, R. A.; Crowell, J. A.; Sigman, C. C.; Kelloff, G. J. *Cancer, Epidemiology, Biomarkers, & Prevention* 1999, *8*, 467.

(3) Rioux, N.; Castonguay, A. *Carcinogenesis* 1998, *19*, 1393.

(4) Nie, D.; Hillman, G. G.; Geddes, T.; Tang, K.; Pierson, C.; Grignon, D. J.; Honn, K. V. *Cancer Research* 1998, *58*, 4047.

(5) Ghosh, J.; Myers, C. E. *Proc. Natl. Acad. Sci. USA* 1998, *95*, 13182.

(6) Lehnert, N.; Solomon, E. L. *J. Biol. Inorg. Chem.* 2003, *8*, 294.

(7) Hatcher, E.; Soudackov, A. V.; Hammes-Schiffer, S. *Journal of the American Chemical Society* 2004, *126*, 5763.

(8) Knapp, M. J.; Rickert, K. W.; Klinman, J. P. *Journal of the American Chemical Society* 2002, *124*, 3865.

(9) Holman, T. R.; Zhou, J.; Solomon, E. L. *Journal of the American Chemical Society* 1998, *120*, 12564.

(10) Cukier, R. I. *Journal of Physical Chemistry* 1996, *100*, 15428.

(11) Cukier, R. I. *Journal of Physical Chemistry* 1994, *98*, 2377.

(12) Cukier, R. I. *Journal of Physical Chemistry A* 1999, *103*, 5989.

(13) Cukier, R. I. *Biochimica et Biophysica Acta-Bioenergetics* 2004, *1655*, 37.

(14) Soudackov, A.; Hammes-Schiffer, S. *Journal of Chemical Physics* 1999, *111*, 4672.

(15) Soudackov, A.; Hammes-Schiffer, S. *Journal of Chemical Physics* 2000, *113*, 2385.

(16) Basilevsky, M. V.; Rostov, I. V.; Newton, M. D. *Chemical Physics* 1998, *232*, 189.

(17) Warshel, A. *Computer Modeling of Chemical Reactions in Enzymes and Solutions*; John Wiley & Sons, Inc.: New York, 1991.

(18) Marcus, R. A. *Annual Reviews of Physical Chemistry* 1964, *15*, 155.

(19) Soudackov, A. V.; Hatcher, E.; Hammes-Schiffer, S. *Journal of Chemical Physics* 2005, *122*, 014505.

Chapter 2

Proton-Coupled Electron Transfer in Soybean Lipoxygenase-1

Reproduced in part with permission form E. Hatcher, A. Soudackov, S. Hammes-Schiffer, *Journal of American Chemical Society*, **2004**, 126, 5763-5775.

Introduction

Lipoxygenases catalyze the oxidation of unsaturated fatty acids and have a wide range of biomedical applications. In mammals, lipoxygenases aid in the production of leukotrienes and lipoxins, which regulate responses in inflammation and immunity.[1] Thus, lipoxygenase inhibitors have been used as drug agents to treat inflammatory diseases such as asthma, atherosclerosis, and psoriasis.[1,2] In addition, lipoxygenase inhibitors have been proposed as promising cancer chemopreventive agents.[3-6] Numerous kinetic studies of lipoxygenases have been carried out using soybean lipoxygenase-1 (SLO)[7] and human lipoxygenase[8] with the substrate linoleic acid.[9] As shown in Figure **1**, the pro-*S* hydrogen atom from carbon atom C11 of linoleic acid is transferred to the Fe(III)–OH cofactor, forming a radical intermediate substrate and Fe(II)–OH_2.[7] Subsequent reaction with molecular oxygen eventually leads to hydroperoxyoctadecadienoic acid and Fe(III)–OH.

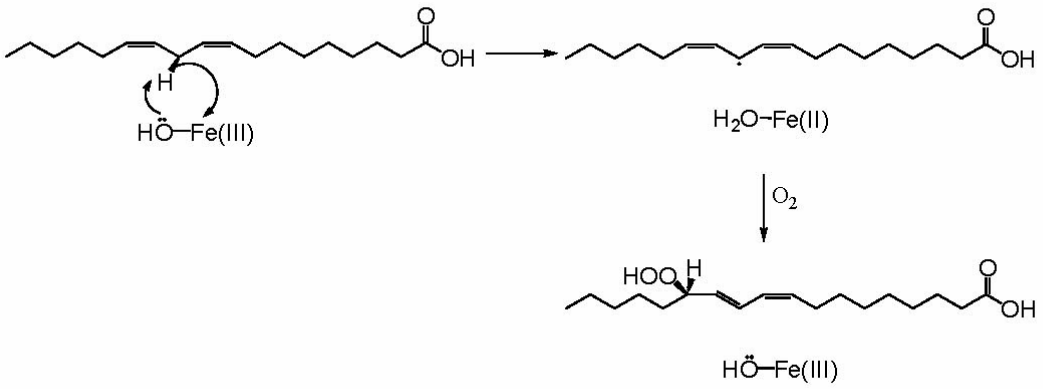

Figure **1**: Proposed mechanism of soybean lipoxygenase.[7] This paper focuses on the first step, which involves the net hydrogen atom transfer from the linoleic acid substrate to the Fe(III)–OH cofactor.

The hydrogen transfer step in SLO has been investigated with a wide range of experimental and theoretical techniques. Kinetic studies have shown that this step is rate limiting above 32° C for SLO.[10] Quantum mechanical calculations indicate that the electron transfers from the π system of the linoleic acid to an orbital localized on the Fe(III) center, and the proton transfers from the donor carbon to the oxygen acceptor.[11] Thus, although the reaction involves a net hydrogen atom transfer, the electron and proton are transferred between distinct donors and acceptors. Moreover, analysis of the thermodynamic properties of the single proton transfer (PT) and electron transfer (ET) reactions, as well as the concerted proton-coupled electron transfer (PCET) mechanism, indicates that the single PT and ET reactions are significantly endothermic, whereas the PCET reaction is exothermic.[11,12] Based on these analyses, the proposed mechanism for this reaction is a PCET in which the electron and proton transfer simultaneously between different donors and acceptors.

The deuterium kinetic isotope effect (KIE) on the catalytic rate for SLO has been measured to be as high as 81 at room temperature.[7,12-15] Large KIEs have also been

measured for human lipoxygenase.[8] The temperature dependence of the KIEs has been analyzed in terms of various tunneling models.[7,13] These theoretical studies suggest that hydrogen tunneling plays a central role in this reaction. The importance of gating, which is defined in terms of vibrational modes that modulate the hydrogen transfer distance, has also been discussed.[12] In addition, a number of mutants of SLO have been studied experimentally and theoretically.[12,16]

In this paper, we investigate the PCET reaction in SLO with a multistate continuum theory.[17-19] In this theoretical formulation, the PCET reaction is described in terms of the four charge transfer states involving the proton and the electron, and the transferring hydrogen nucleus is represented by a quantum mechanical wavefunction. The conformations of the linoleic acid bound to SLO are investigated with docking calculations. The reorganization energy of the iron complex is examined with density functional theory methods, and the reorganization energy of the protein environment is calculated within the dielectric continuum approximation using the frequency resolved cavity model.[20,21] The multistate continuum theory calculations reproduce the experimentally observed temperature dependence of the rates and KIEs. An analysis of the results elucidates the detailed mechanism of the PCET reaction and provides an explanation for the unusually large magnitude and observed temperature dependence of the KIE.

Theory

PCET reactions have been studied with a variety of theoretical methods.[17-19,22-24] The theoretical formulation used to describe ET and PCET reactions in this paper is based primarily on the recently developed multistate continuum theory.[17-19] In this formulation, the solute is described by a multistate valence bond model, the transferring hydrogen nucleus is treated quantum mechanically, and the solvent is represented as a dielectric continuum. This theory may be used to calculate the free energy surfaces for PCET as functions of two collective solvent coordinates corresponding to PT and ET,

respectively. The multistate continuum theory also provides rate expressions for PCET reactions.[18]

The PCET reaction catalyzed by lipoxygenase may be described in terms of the following four electronic diabatic states:

($1a$) CH $\cdots$ $^{-}$OH-Fe(III)

($1b$) C^{-} $\cdots$ HOH-Fe(III)

($2a$) CH^{+} $\cdots$ $^{-}$OH-Fe(II)

($2b$) C $\cdots$ HOH-Fe(II)

where 1 and 2 denote the ET state, and a and b denote the PT state. The proton is transferred from the C11 carbon atom of the linoleic acid to the oxygen atom of the Fe-bound OH ligand, and the electron is transferred from the π-system of the linoleic acid to the iron. Within this notation, $1a \rightarrow 1b$ represents PT, $1a \rightarrow 2a$ represents ET, and $1a \rightarrow 2b$ represents EPT (where both the proton and the electron are transferred).

As shown in Ref. 17, the free energy surfaces for PCET reactions may be calculated as functions of two collective solvent coordinates z_p and z_e, corresponding to PT and ET, respectively. For the systems studied in this paper, the PT reaction is electronically adiabatic, while the ET/EPT reactions are assumed to be electronically nonadiabatic.[25] In this case, the ET diabatic free energy surfaces corresponding to ET states 1 and 2 are calculated as mixtures of the a and b PT states. The reactants (I) are mixtures of the $1a$ and $1b$ states, and the products (II) are mixtures of the $2a$ and $2b$ states. The proton vibrational states are calculated for both the reactant (I) and product (II) ET diabatic surfaces, resulting in two sets of two-dimensional vibronic free energy surfaces that may be approximated as paraboloids. In this theoretical formulation, the PCET reaction is described in terms of nonadiabatic transitions from the reactant (I) to the product (II) ET diabatic surfaces. Thus, the ET diabatic states I and II, respectively, may be viewed as the reactant and product PCET states. Note that EPT refers to a transition between pure diabatic states $1a$ and $2b$, whereas PCET refers to a transition between mixed ET diabatic states I ($1a$/$1b$) and II ($2a$/$2b$). For the system studied in this paper, the lowest energy PCET reactant state I is predominantly $1a$, and the lowest energy PCET product state II is predominantly $2b$.

The unimolecular rate expression derived in Ref. 18 for PCET is given in Eq. **1**

$$k^{\mathrm{PCET}} = \frac{2\pi}{\hbar}\sum_{\mu} P_{\mathrm{I}\mu}\sum_{\nu}\left|V_{\mu\nu}\right|^2\left(4\pi\lambda_{\mu\nu}k_{\mathrm{B}}T\right)^{-1/2}\exp\left(\frac{-\Delta G^{\dagger}_{\mu\nu}}{k_{\mathrm{B}}T}\right) \qquad \text{Eq. } \mathbf{1}$$

where $\sum_{\mu}$ and $\sum_{\nu}$ indicate summations over vibrational states associated with ET states 1 and 2, respectively, $P_{\mathrm{I}\mu}$ is the Boltzmann probability for state Iμ, and $\Delta G^{\dagger}_{\mu\nu}$ is the free energy barrier defined in Eq. **2** .

$$\Delta G^{\dagger}_{\mu\nu} = \frac{\left(\Delta G^{\mathrm{o}}_{\mu\nu} + \lambda_{\mu\nu}\right)^2}{4\lambda_{\mu\nu}} \qquad \text{Eq. } \mathbf{2}$$

In this expression the free energy of reaction is shown in Eq. **3**

$$\Delta G^{\mathrm{o}}_{\mu\nu} = \varepsilon^{\mathrm{II}}_{\nu}\left(\bar{z}^{\mathrm{II}\nu}_{\mathrm{p}}, \bar{z}^{\mathrm{II}\nu}_{\mathrm{e}}\right) - \varepsilon^{\mathrm{I}}_{\mu}\left(\bar{z}^{\mathrm{I}\mu}_{\mathrm{p}}, \bar{z}^{\mathrm{I}\mu}_{\mathrm{e}}\right) \qquad \text{Eq. } \mathbf{3}$$

where $\left(\bar{z}^{\mathrm{I}\mu}_{\mathrm{p}}, \bar{z}^{\mathrm{I}\mu}_{\mathrm{e}}\right)$ and $\left(\bar{z}^{\mathrm{II}\nu}_{\mathrm{p}}, \bar{z}^{\mathrm{II}\nu}_{\mathrm{e}}\right)$ are the solvent coordinates for the minima of the ET diabatic free energy surfaces $\varepsilon^{\mathrm{I}}_{\mu}\left(z_{\mathrm{p}}, z_{\mathrm{e}}\right)$ and $\varepsilon^{\mathrm{II}}_{\nu}\left(z_{\mathrm{p}}, z_{\mathrm{e}}\right)$, respectively. Moreover, in the high-temperature approximation for uncoupled solute modes, the total reorganization energy, given in Eq. **4** , is expressed as the sum of the outer-sphere (solvent) and inner-sphere (solute) contributions:

$$\lambda_{\mu\nu} = \left(\lambda_{\mathrm{o}}\right)_{\mu\nu} + \lambda_{\mathrm{in}} \qquad \text{Eq. } \mathbf{4}$$

where the outer-sphere reorganization energy is defined in Eq. **5** .

$$\left(\lambda_{\mathrm{o}}\right)_{\mu\nu} = \varepsilon^{\mathrm{I}}_{\mu}\left(\bar{z}^{\mathrm{II}\nu}_{\mathrm{p}}, \bar{z}^{\mathrm{II}\nu}_{\mathrm{e}}\right) - \varepsilon^{\mathrm{I}}_{\mu}\left(\bar{z}^{\mathrm{I}\mu}_{\mathrm{p}}, \bar{z}^{\mathrm{I}\mu}_{\mathrm{e}}\right) = \varepsilon^{\mathrm{II}}_{\nu}\left(\bar{z}^{\mathrm{I}\mu}_{\mathrm{p}}, \bar{z}^{\mathrm{I}\mu}_{\mathrm{e}}\right) - \varepsilon^{\mathrm{II}}_{\nu}\left(\bar{z}^{\mathrm{II}\nu}_{\mathrm{p}}, \bar{z}^{\mathrm{II}\nu}_{\mathrm{e}}\right) \qquad \text{Eq. } \mathbf{5}$$

The inner-sphere reorganization energy λ_{in} will be discussed below. The coupling $V_{\mu\nu}$ in the PCET rate expression (Eq. **6**) is defined as

$$V_{\mu\nu} = \left\langle \phi_\mu^{\mathrm{I}} \left| V\left(r_{\mathrm{p}}, z_{\mathrm{p}}^{\dagger}\right) \right| \phi_\nu^{\mathrm{II}} \right\rangle_{\mathrm{p}} \qquad \text{Eq. } \mathbf{6}$$

where the subscript of the angular brackets indicates integration over r_{p}, $z_{\mathrm{p}}^{\dagger}$ is the value of z_{p} in the intersection region, and ϕ_μ^{I} and ϕ_ν^{II} are the proton vibrational wavefunctions for the reactant and product ET diabatic states, respectively.

Recently the multistate continuum theory has been extended to include the motion between the proton donor and acceptor.[26] For the classical treatment of the donor-acceptor vibrational mode *R*, we use the following expression (Eq. **7**) to calculate the total rate:

$$k_{\mathrm{gating}}^{\mathrm{PCET}} = \frac{2\pi}{\hbar} \int_0^\infty dR \sum_\mu P_{\mathrm{l}\mu}(R) \sum_\nu \left| V_{\mu\nu}(R) \right|^2 \left[4\pi\lambda_{\mu\nu}(R) k_{\mathrm{B}} T \right]^{-1/2} \exp\left[\frac{-\Delta G_{\mu\nu}^{\dagger}(R)}{k_{\mathrm{B}} T} \right] \qquad \text{Eq. } \mathbf{7}$$

where all of the quantities are defined analogously as for Eq. **1** and are evaluated at a particular proton donor-acceptor distance *R*. (Note that this thermal averaging is based on the assumption that a Boltzmann distribution is maintained for the proton donor-acceptor vibrational mode.) Thus, the two-dimensional vibronic free energy surfaces and the corresponding PCET rates are calculated for a series of proton donor-acceptor distances along a grid, and the integral in Eq. **7** is evaluated numerically. Note that the normalization constant for the Boltzmann probability $P_{\mathrm{l}\mu}(R)$ is calculated by integrating over *R* as well as summing over reactant vibronic states μ. For the quantum mechanical treatment of the donor-acceptor vibrational mode *R*, we use the general form of the rate expression given in Eq. **1** in conjunction with two-dimensional vibrational wavefunctions that depend on the hydrogen coordinate *r* and the proton donor-acceptor distance *R*.

The inner-sphere reorganization energy for the PCET reaction due to the Fe-ligand bonds is approximated in Eq. **8** [27]

$$\lambda_{\mathrm{in}} = \sum_j \frac{f_j^{\mathrm{r}} f_j^{\mathrm{p}}}{f_j^{\mathrm{r}} + f_j^{\mathrm{p}}} \left(\Delta q_j \right)^2 \qquad \text{Eq. } \mathbf{8}$$

where the summation is over the six Fe-ligand modes (assumed to be harmonic), f_j^{r} and f_j^{p} are the equilibrium force constants of the *j*th mode in the reactant and product, respectively, and Δq_j is the difference in the reactant and product equilibrium bond lengths for the *j*th mode. For the system studied in this paper, the inner-sphere reorganization energy is calculated between the diabatic states 1*a* and 2*b* because these diabatic states are dominant in the reactant and product PCET states.

Calculation of Input Quantities

Within the framework of this theoretical formulation,[17-19] the calculation of the rates and KIEs requires the inner-sphere reorganization energy, the solvent reorganization energy matrix elements, and the gas phase valence bond matrix elements. For the classical treatment of the donor-acceptor mode, the calculation of the rates involves the following three steps. In the first step of the procedure, the two-dimensional free energy surfaces $\varepsilon_\mu^{\mathrm{I}}\left(z_{\mathrm{p}}, z_{\mathrm{e}}\right)$ and $\varepsilon_\nu^{\mathrm{II}}\left(z_{\mathrm{p}}, z_{\mathrm{e}}\right)$ corresponding to the solvated reactant and product vibronic states are calculated for a series of proton donor-acceptor distances *R* along a grid. These surfaces are calculated from the gas phase valence bond matrix elements and the solvent reorganization energy matrix elements using the analytical expressions given in Ref. 17. In the second step, the free energy difference $\Delta G_{\mu\nu}^{\mathrm{o}}$ and the solvent reorganization energy $\left(\lambda_{\mathrm{o}}\right)_{\mu\nu}$ is determined for each pair of vibronic states using Eq. **3** and Eq. **5** , respectively, at each grid point for *R*. The coupling $V_{\mu\nu}$ for each pair of vibronic states is determined from the associated vibrational wavefunctions and the off-diagonal gas phase valence bond matrix elements using Eq. **6** . In the third step, these quantities and the inner-sphere reorganization energy are used to calculate the total PCET rate with Eq. **7** (or Eq. **1** for a fixed value of *R*).

Thus, this theoretical formulation requires three types of input quantities. The inner-sphere (solute) reorganization energy λ_{in} may be calculated from the equilibrium

force constants and bond lengths. In this paper, the outer-sphere (solvent) reorganization energy matrix elements are calculated with an electrostatic dielectric continuum model. In practice, the gas phase valence bond matrix elements are represented by molecular mechanical terms fit to electronic structure calculations or experimental data.[28]

Inner-sphere reorganization energy

The inner-sphere reorganization energy due to the Fe-ligand bonds was determined from Eq. **8** . The force constants were obtained from experimental measurements on model compounds.[27] Specifically, the force constants for $[Fe(NH_3)_6]^{2+}$ and $[Fe(NH_3)_6]^{3+}$ of 148 and 232 kcal mol^{-1} $Å^{-2}$ are used for the three histidines (His499, His504, His690) and the force constants for $[Fe(H_2O)_6]^{2+}$ and $[Fe(H_2O)_6]^{3+}$ of 230 and 366 kcal mol^{-1} $Å^{-2}$ are used for Asn694, Ile839 and Wat842. The values for Δq_j are determined from geometry optimizations with density functional theory (DFT) at the B3LYP/LanL2DZ level[29-32] for the model system depicted in Figure **2**. All electronic structure calculations in this paper were performed with Gaussian98.[33] In this model, the amino acids are represented by the relevant fragments: histidines by imidazole rings, asparagine by a formamide molecule, and isoleucine by a formic anion. We performed optimizations for Fe(III) and Fe(II) complexes with both a water and a hydroxide ligand. Table **1** gives the Fe-ligand bond lengths for the four different complexes. These results are consistent with previous calculations on the Fe(III)OH and $Fe(II)OH_2$ model complexes.[34] The calculated Fe-ligand distances were used to estimate the inner-sphere reorganization energy to be 19 kcal/mol.

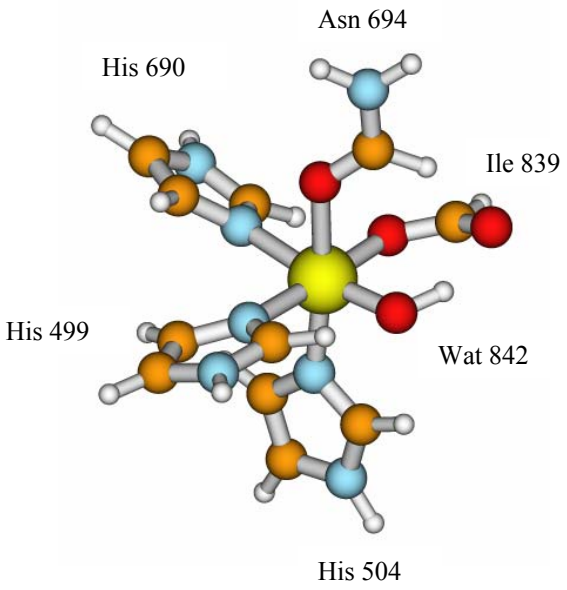

Figure **2**: Model iron complex used for the DFT B3LYP calculations with the geometry optimized for the Fe(III)–OH state.

Table **1**: DFT B3LYP results for the Fe-ligand distances for the four diabatic states of the model system in Figure **2**.

	Fe(III) – OH	Fe(III) – OH_2	Fe(II) – OH	Fe(II) – OH_2
Fe – His499 Nε2	2.16	2.11	2.24	2.18
Fe – His504 Nε2	2.14	2.11	2.21	2.19
Fe – His690 Nε2	2.18	2.08	2.27	2.14
Fe – Asn694 Oδ1	2.18	2.05	2.30	2.22
Fe – Ile839 O1	2.05	2.02	2.22	2.23
Fe – Wat842 O	1.86	2.13	1.97	2.17

Outer-sphere reorganization energy

The solvent reorganization energies are calculated with the frequency-resolved cavity model (FRCM) developed by Newton, Rostov, and Basilevsky.[20,21] This approach

allows for distinct effective solute cavities pertaining to the optical and inertial solvent response. The cavities are formed from spheres centered on all of the atoms. The two effective radii for the solute atoms are defined as $r_\infty = \kappa r_{\mathrm{vdW}}$ and $r_{\mathrm{in}} = r_\infty + \delta$, where r_{vdW} is the van der Waals radius, κ is a universal scaling factor, and δ is a constant specific to the particular solvent. In our calculations, κ = 0.9 and δ = 0.9, as determined for cations in water.[21] The static dielectric constant for the protein was chosen to be $\varepsilon_o = 4.0$,[35] and the optical dielectric constant was chosen to be $\varepsilon_\infty = 1.78$, as for water. The solvation properties are calculated with the model shown in Figure **3**, which includes all atoms of the linoleic acid and an iron complex. The charge density of each diabatic (i.e., valence bond) state is defined by assigning appropriate partial charges to all atoms. The reorganization energy matrix element between diabatic states *i* and *j* is determined by calculating the interaction of the charge density of state *i* with the dielectric continuum solvent response to the charge density of state *j*.

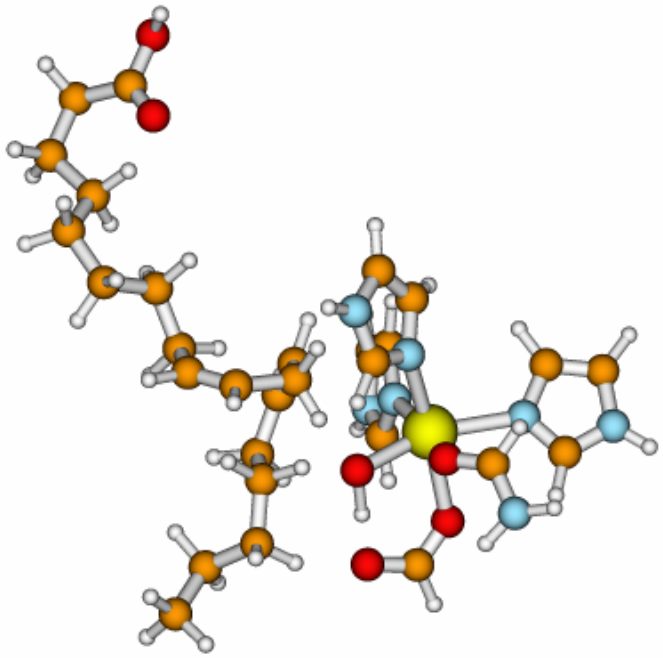

Figure **3**: Conformation of linoleic acid and the iron cofactor obtained from docking calculations that included the entire SLO protein.

The atomic coordinates utilized for the FRCM calculations were obtained from docking calculations on linoleic acid and SLO. We used the AutoDock 3.0.5 program[36] to perform these docking calculations. In these calculations, the protein (including the Fe(III)–OH cofactor) is fixed at the crystal structure coordinates obtained from the Brookhaven Protein Data Bank (pdb code 1F8N).[37] During the docking procedure, the linoleic acid is flexible within a grid of dimensions 30×15×15 Å spanning the cavity region. We generated 1000 different conformations. We chose several suitable conformations based on the C–O distance and the CHO angle. One of the suitable conformations is depicted in Figure **3**. This conformation has a C–O distance of 2.83 Å and a CHO angle of 152 degrees, and the carboxylate group of the linoleic acid is

oriented opposite to the isoleucine ligand as found in the purple bacteria.[38] This conformation was used to calculate the solvent reorganization energy matrix elements. We calculated the solvent reorganization energy matrix elements for this conformation and for two other conformations with C–O distances of 3.0 and 3.2 Å, respectively. We found that the solvent reorganization energies are not sensitive to the specific choice of conformation.

The atomic charges for the diabatic states used for the FRCM calculations in this paper were designated as follows. The iron atom was assigned a charge of +2 or +3 corresponding to the appropriate oxidation state. The atomic charges on the His499, His504, His690, Asn694, and Ile839 ligands were obtained with the CHELPG method[39] based on DFT B3LYP/6-31G** calculations for each individual ligand with the crystal structure coordinates. The atomic charges for the water ligand were obtained with the CHELPG method based on DFT B3LYP/6-31G** calculations for an optimized isolated water molecule. The atomic charges for the hydroxide ligand were determined by assigning the same charge (+0.36) for the hydrogen as determined for the water ligand and assigning the remainder of the –1 charge to the oxygen atom. The atomic charges on the linoleic acid were obtained by applying the CHELPG method with DFT B3LYP/6-31G** for the conformation determined from the docking calculations. The atomic charge for the transferring hydrogen was assigned +0.36 for diabatic states 1*a* and 2*a*, and the atomic charge for C11 was adjusted to obtain the correct overall charge for each of the four diabatic states. Note that the solvent quantities are approximated to be independent of the proton donor-acceptor distance *R* within the relevant range.

Gas-phase valence bond matrix elements

The gas-phase valence bond matrix elements for the PCET reaction are based on a linear, five-site model:

$$\pi_D - C_D - H - O_A - Fe_A$$

where the D and A subscripts denote donor and acceptor, respectively. The proton is transferred from the carbon atom (C_D) of the linoleic acid to the oxygen atom (O_A) of the Fe-bound OH ligand. The electron is transferred from the π-system of the linoleic acid (π_D) to the iron (Fe_A). The gas phase valence bond matrix elements are represented by molecular mechanical terms fit to electronic structure calculations and experimental data. We emphasize that this five-site model is used only to provide molecular mechanical functional forms for the gas-phase matrix elements. The carbon, hydrogen, oxygen, and iron atoms are not linear in the conformation obtained from the docking procedure, but the linear model provides a qualitatively reasonable potential for fitting to experimental data. As described above, all atoms of the complex are included in the conformations obtained from the docking procedure for the calculation of solvation properties.

The diagonal matrix elements of the gas phase Hamiltonian are expressed in Eq. **9**

.

$$
\begin{aligned}
\left(h_o\right)_{1a,1a} &= U_a^{\mathrm{LEPS}} + U_{\pi\mathrm{C}}^{\mathrm{harm}} + U_{\mathrm{FeO}}^{\mathrm{harm}} \\
\left(h_o\right)_{1b,1b} &= U_b^{\mathrm{LEPS}} + U_{\pi\mathrm{C}}^{\mathrm{harm}} + U_{\mathrm{FeO}}^{\mathrm{harm}} + \Delta E_{1b} \\
\left(h_o\right)_{2a,2a} &= U_a^{\mathrm{LEPS}} + U_{\pi\mathrm{C}}^{\mathrm{harm}} + U_{\mathrm{FeO}}^{\mathrm{harm}} + \Delta E_{2a} \\
\left(h_o\right)_{2b,2b} &= U_b^{\mathrm{LEPS}} + U_{\pi\mathrm{C}}^{\mathrm{harm}} + U_{\mathrm{FeO}}^{\mathrm{harm}} + \Delta E_{2b}
\end{aligned}
\qquad \text{Eq. } \mathbf{9}
$$

These diagonal terms represent the potential energy for the unperturbed diabatic states. Note that the positions of the π_D and Fe_A sites are fixed, and these matrix elements depend on the positions of the C_D, H, and O_A sites. The proton transfer interface C_DHO_A is described by a LEPS potential, shown in Eq. **10** [40-42]

$$
\begin{aligned}
U_a^{\mathrm{LEPS}} &= Q_{\mathrm{CH}} + Q_{\mathrm{OH}} + Q_{\mathrm{CO}} - \frac{1}{2}\left(J_{\mathrm{CO}} + J_{\mathrm{OH}}\right) + J_{\mathrm{CH}} \\
U_b^{\mathrm{LEPS}} &= Q_{\mathrm{CH}} + Q_{\mathrm{OH}} + Q_{\mathrm{CO}} - \frac{1}{2}\left(J_{\mathrm{CO}} + J_{\mathrm{CH}}\right) + J_{\mathrm{OH}}
\end{aligned}
\qquad \text{Eq. } \mathbf{10}
$$

where the Coulomb and exchange terms (Eq. **11**) are

$$Q_{XY} = \frac{E^1_{XY}\left(1+k_{XY}\right)+E^3_{XY}\left(1-k_{XY}\right)}{2\left(1+k_{XY}\right)}$$
$$J_{XY} = \frac{E^1_{XY}\left(1+k_{XY}\right)-E^3_{XY}\left(1-k_{XY}\right)}{2\left(1+k_{XY}\right)} \qquad \text{Eq. } \mathbf{11}$$

and the Morse and anti-Morse potentials (Eq. **12**)are

$$E^1_{XY} = D_{XY}\left(e^{-2\beta_{XY}\left(R_{XY}-R^o_{XY}\right)}-2e^{-\beta_{XY}\left(R_{XY}-R^o_{XY}\right)}\right)$$
$$E^3_{XY} = \frac{1}{2}D_{XY}\left(e^{-2\beta_{XY}\left(R_{XY}-R^o_{XY}\right)}+2e^{-\beta_{XY}\left(R_{XY}-R^o_{XY}\right)}\right) \qquad \text{Eq. } \mathbf{12}$$

For simplicity, the empirical Sato parameter k_{XY} was set to 0.5 for all pairs of atoms, similar to the value used previously.[41] The values for D_{CH} and D_{OH} were determined to be 77 and 82 kcal/mol based on the bond dissociation energies discussed in Appendix A. The values for β_{CH} and β_{OH} were determined to be 2.068 and 2.442 Å^{-1} to reproduce the typical experimentally measured C–H and O–H frequencies of 2900 and 3500 cm^{-1}. The values for R^o_{CH} and R^o_{OH} were determined to be 1.09 and 0.96 Å from typical experimentally measured bond lengths.[28] In the first model studied, the C–O Morse parameters were chosen as follows: R^o_{CO} = 2.83 Å, the distance in a conformation obtained from docking; D_{CO} = 8 kcal/mol, as used in related LEPS potentials;[41] and β_{CO} = 2.5 Å^{-1}, corresponding to a Morse frequency of 415 cm^{-1} for a reduced mass of 6.86 g/mol, to be consistent with the harmonic frequencies of the Fe–O and the carbon atom C11 motions discussed below. In the Results section, we discuss the dependence of the results on the C–O Morse parameters R^o_{CO} and β_{CO} and present the results for an alternative model in which R^o_{CO} = 3.0 Å and β_{CO} = 1.8 Å^{-1}.

The harmonic terms are included in Eq. **9** to confine the carbon and oxygen atoms between the electron donor and acceptor in a physically reasonable manner. In the first model studied, the force constant for U^{harm}_{FeO} was chosen to be of 366 kcal mol^{-1} Å^{-2}, corresponding to the experimentally measured value for $[Fe(H_2O)_6]^{3+}$.[27] The equilibrium

distance for $U_{\mathrm{FeO}}^{\mathrm{harm}}$ was chosen to be the value determined from the DFT B3LYP calculations for the Fe(III)-OH state, as given in Table **1** . The force constant of 117 kcal mol^{-1} Å^{-2} for $U_{\pi\mathrm{C}}^{\mathrm{harm}}$ was determined from a DFT B3LYP/6-31G** frequency calculation on an optimized structure for linoleic acid, where the scaling factor[43] of 0.96 was applied to the frequency (339 cm^{-1}) of the mode representing the relevant vibrational motion of carbon atom C11. The equilibrium distance for $U_{\pi\mathrm{C}}^{\mathrm{harm}}$ was chosen to be 1.0 Å. Based on the equilibrium distances, the π_{D}–$\mathrm{Fe_A}$ distance was fixed at 5.69 Å for all diabatic states. Note that the frequency of the C–O vibrational motion is determined mainly by these harmonic frequencies in this model. In the alternative model mentioned above, the force constants for $U_{\mathrm{FeO}}^{\mathrm{harm}}$ and $U_{\pi\mathrm{C}}^{\mathrm{harm}}$ are chosen to be 100 and 25 kcal mol^{-1} Å^{-2}, respectively, and the frequency of the C–O vibrational motion is determined mainly by the Morse parameter β_{CO}.

The constants ΔE_{1b}, ΔE_{2a}, and ΔE_{2b} are fit to reproduce the experimentally determined driving forces (i.e., reaction free energies) for PT, ET, and PCET, respectively. As shown in Appendix A, the resulting reaction free energies are estimated to be:

$$\begin{aligned} \Delta G_{1a\to 1b}^{\mathrm{o\,PT}} &= 32 \text{ kcal/mol} \\ \Delta G_{1a\to 2a}^{\mathrm{o\,ET}} &= 43 \text{ kcal/mol} \quad . \\ \Delta G_{1a\to 2b}^{\mathrm{o\,EPT}} &= -5.4 \text{ kcal/mol} \end{aligned}$$

The parameterized constants ΔE_{1b}, ΔE_{2a}, and ΔE_{2b} are 36.07, 37.26, and –20.42 kcal/mol, respectively.

In this paper, the couplings are of the form given in Eq. **13**

$$\begin{aligned} \left(h_{\mathrm{o}}\right)_{1a,1b} &= \left(h_{\mathrm{o}}\right)_{2a,2b} = -V^{\mathrm{PT}} e^{-\alpha\left(R_{\mathrm{CO}}-R_{\mathrm{CO}}^{\mathrm{o}}\right)} \\ \left(h_{\mathrm{o}}\right)_{1a,2a} &= \left(h_{\mathrm{o}}\right)_{1b,2b} = V^{\mathrm{ET}} \\ \left(h_{\mathrm{o}}\right)_{1a,2b} &= \left(h_{\mathrm{o}}\right)_{1b,2a} = V^{\mathrm{ET}}\sigma \end{aligned} \qquad \text{Eq. } \mathbf{13}$$

where the overlap integral σ = 0.5, as in the standard two-state LEPS model for triatomic collinear systems.[44] The exponential factor α = 1 Å^{-1} was chosen to reproduce the R_{CO}-dependence of the LEPS off-diagonal term (Eq. **14**) for larger C–O distances.

$$\left(h_{o}\right)_{1a,1b} = \left(h_{o}\right)_{2a,2b} \approx \frac{1}{2}\left(Q_{CH} + Q_{OH} + Q_{CO}\right) - J_{CO} + \frac{1}{2}\left(J_{CH} + J_{OH}\right) \qquad \text{Eq. } \mathbf{14}$$

The coupling V^{ET} = 0.019 kcal/mol was determined by fitting to the experimental rate for the PCET reaction at T = 303 K. The coupling V^{PT} = 19.5 kcal/mol was chosen to be similar in magnitude to the couplings used in other related EVB models and was refined to fit the experimental KIE for the PCET reaction at T = 303 K.

We emphasize that the gas phase potential energy surface for each ET diabatic state is a mixture of the PT diabatic states. Specifically, the gas phase potential energy surface for ET diabatic state 1 is a mixture of the diagonal terms 1*a* and 1*b* given in Eq. **9** , where the degree of mixing is determined by the off-diagonal terms. Moreover, each diabatic state is a combination of LEPS potentials and additional harmonic terms. Thus, typically the equilibrium bond lengths and frequencies for the overall gas phase potential energy surface are different from the corresponding input parameters for the Morse potentials. The gas phase potential energy surfaces are depicted in Figure **4**.

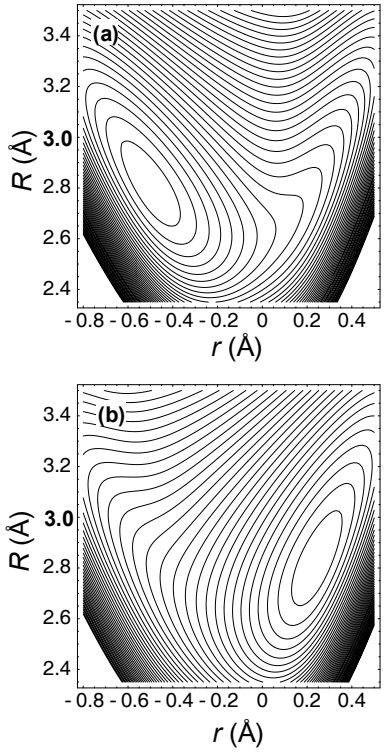

Figure **4**: Gas phase EVB potential energy surface as a function of the hydrogen coordinate *r* and the proton donor-acceptor distance *R* for (a) ET state I, which is a mixture of diabatic states 1*a* and 1*b*, and (b) ET state II, which is a mixture of diabatic states 2*a* and 2*b*.

Results and Discussion

Reorganization energies

The inner-sphere reorganization energy due to the Fe-ligand bonds was calculated from Eq. **8** , where the force constants were obtained from experimental data and the bond length changes were determined from density functional theory calculations on model compounds. The resulting inner-sphere reorganization energy is 19.1 kcal/mol.

As indicated in Table **1** , the dominant contribution to this inner-sphere reorganization energy arises from the difference in the Fe(III)–OH and the Fe(II)–OH_2 bond lengths.[45,46] Note that this calculation provides only an estimate of the total inner-sphere reorganization energy. The inner-sphere reorganization energy due to the Fe-ligand bonds is expected to be somewhat smaller in the protein than in the gas phase. Moreover, the reorganization of the linoleic acid substrate may also contribute to the total inner-sphere reorganization energy. At the end of this section we discuss the dependence of the results on the inner-sphere reorganization energy and show that the temperature dependence of the KIE is reproduced qualitatively for inner-sphere reorganization energies of 10–30 kcal/mol, but the temperature dependence of the rates increases as the inner-sphere reorganization energy increases mainly due to an increase in the free energy barrier.

We calculated the outer-sphere reorganization energies due to the protein with the FRCM method for conformations with C–O distances of 2.83, 3.0, and 3.2 Å. The calculated diabatic outer-sphere reorganization energies for PT ($1a \rightarrow 1b$), ET ($1a \rightarrow 2a$), and EPT ($1a \rightarrow 2b$) are 1.8, 3.8, and 2.4 kcal/mol, respectively, for the conformation with a C–O distance of 2.83 Å. The calculated diabatic solvent reorganization energy for EPT varied by less than 0.3 kcal/mol for the three different conformations, so we concluded that the solvent reorganization energies are not sensitive to the specific choice of conformation. These outer-sphere reorganization energies are small compared to those calculated for analogous reactions in polar solvents because the dielectric constant for the protein is relatively small. Furthermore, the outer-sphere reorganization energy is smaller for EPT than for ET because the electron and proton are transferred in the same direction. The EPT reaction corresponds to a net hydrogen atom reaction, which involves a smaller change in the solute charge distribution than does the ET reaction.

Classical treatment of donor-acceptor motion

We calculated the rates and KIEs for the overall PCET reaction using the multistate continuum theory. The first step was to generate the two-dimensional free energy surfaces corresponding to the solvated reactant and product vibronic states as functions of the solvent coordinates z_p and z_e for a series of donor-acceptor distances R along a grid. Using the parameters given in the previous section, the equilibrium C–O distance and frequency are $R_l^o = 2.88$ Å and $\omega_l^o = 511$ cm^{-1} at the minimum of the lowest energy reactant free energy surface. This frequency is calculated from the second derivative with respect to R using a reduced mass of 6.86 g/mol corresponding to carbon and oxygen. Note that this frequency represents the local vibrational motion of the carbon and oxygen atoms and is not directly related to a "gating" frequency of the protein as discussed in Ref. 12. Nevertheless, the protein motion is expected to influence the local proton donor-acceptor vibrational motion.

As discussed above, five parameters were fit to five experimentally determined quantities. Specifically, the relative energies ΔE_{1b}, ΔE_{2a}, and ΔE_{2b} were fit to the experimentally determined reaction free energies, and the couplings V^{ET} and V^{PT} were fit to the experimental rate and KIE at T = 303 K. No other parameters were adjusted. The temperature dependence of the rates was calculated from Eq. **7** . (For simplicity, all input quantities were assumed to be independent of temperature.) The resulting temperature dependences of the hydrogen and deuterium rates, as well as the KIE, are depicted in Figure **5**. This figure illustrates that the calculated rates and KIEs agree with the experimental data. The dependence of these results on the parameters in the model is discussed below.

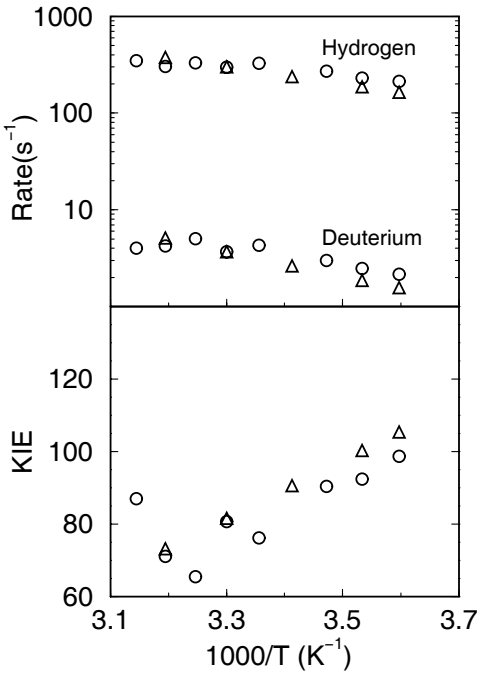

Figure **5**: Temperature dependence of the rates and KIEs for multistate continuum theory calculations with a classical treatment of the proton donor-acceptor vibrational motion. The experimental data are denoted with circles, and the theoretical results are denoted with triangles. The calculations use the original parameter set. The equilibrium C–O distance and frequency are $R_{\mathrm{I}}^{\mathrm{o}} = 2.88$ Å and $\omega_{\mathrm{I}}^{\mathrm{o}} = 511$ cm^{-1} and the dominant C–O distance is $R_{\mathrm{dom}} = 2.69$ Å.

We examined the origin of the unusually large KIE for this reaction. We found that the dominant contribution to the rate in Eq. **7** arises from the lowest energy reactant and product vibronic states. The hydrogen potential energy curves and the associated proton vibrational wavefunctions for these vibronic states are depicted in Figure **6**. The relatively small overlap between these two wavefunctions leads to a large KIE. As discussed previously,[47] the KIE for each pair of states is approximately proportional to the square of the ratio of the overlap for hydrogen to the overlap for deuterium. This ratio increases as the vibrational wavefunction overlap decreases. Moreover, since the

vibrational overlap is smallest for the reactive channel involving the lowest energy reactant and product vibronic states, the overall KIE decreases as the contributions from channels involving higher energy vibronic states increase. Thus, the unusually large KIE for lipoxygenase is due to the relatively small overlap of the vibrational wavefunctions and the dominance of the lowest energy reactant and product vibronic states in the tunneling process.

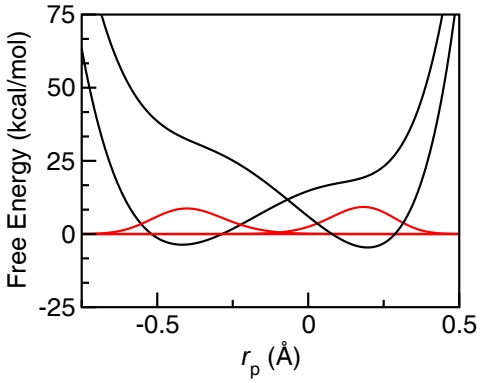

Figure **6**: Reactant and product proton potential energy curves and the associated proton vibrational wavefunctions for the lowest energy reactant and product states at the lowest energy intersection point of the two-dimensional free energy surfaces for R = 2.69 Å. The overlap of these hydrogen vibrational wavefunctions is 0.0093, and the corresponding overlap of the deuterium vibrational wavefunctions is 0.00086.

We investigated the importance of the proton donor-acceptor vibrational motion to the PCET rate. As mentioned above, the equilibrium proton donor-acceptor distance is R_l^o = 2.88 Å for the lowest energy reactant free energy surface. In contrast, the dominant contribution to the overall PCET rate (Eq. **7**) at T = 303 K arises from a proton donor-acceptor distance of R_{dom} = 2.69 Å, as illustrated in Figure **7**a. The dominant proton donor-acceptor distance is ~0.02 Å smaller for deuterium than for hydrogen and varies by ~0.02 Å over the temperature range studied. Figure **7**a indicates that the contribution from the equilibrium donor-acceptor distance of R_l^o = 2.88 Å to the overall PCET rate is negligible. We analyzed the various terms in the rate expression to understand the origin

of this phenomenon. The reaction free energies and the reorganization energies do not depend strongly on the proton donor-acceptor distance. As illustrated in Figure **7**b, the coupling $V_{\mu\nu}$ given in Eq. **6** increases significantly as the proton donor-acceptor distance decreases. This increase in the coupling is due mainly to the increase in the overlap between the reactant and product proton vibrational wavefunctions as R decreases. On the other hand, the Boltzmann probability $P_{\mathrm{I}\mu}(R)$ has a maximum at $R \approx 2.88$ Å, as depicted in Figure **7**b. The dominant proton donor-acceptor distance for the overall PCET reaction is determined by a balance between the larger coupling and the smaller Boltzmann probability as the distance decreases.

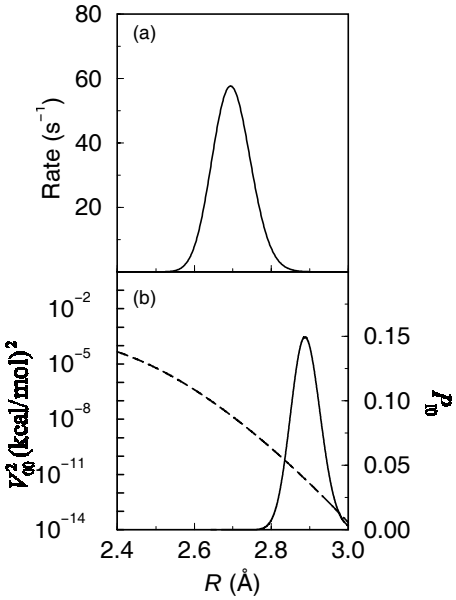

Figure **7**: Analysis of the theoretical calculations with a classical treatment of the proton donor-acceptor vibrational motion. (a) Contribution to the overall rate as a function of the proton donor-acceptor distance R. The overall rate is obtained by integration of this function. The dominant contribution to the overall PCET rate corresponds to the distance $R_{\mathrm{dom}} = 2.69$ Å. (b) The square of the coupling V_{00}^2 (dashed) and the Boltzmann probability $P_{\mathrm{I}0}$ (solid) for the lowest energy reactant and product states as functions of the proton donor-acceptor distance R. The equilibrium donor-acceptor distance on the lowest energy reactant free energy surface is $R_{\mathrm{I}}^{\mathrm{o}} = 2.88$ Å.

Fixed donor-acceptor distance

To further analyze the role of the proton donor-acceptor vibrational mode, we calculated the rates and KIEs for fixed donor-acceptor distances of R = 2.7 and 2.8 Å using Eq. **1** . As for the previous calculations, the relative energies of the four diabatic states were fit to the experimentally determined reaction free energies, and the couplings V^{ET} and V^{PT} were fit to the experimental rate and KIE, respectively, at T = 303 K, but no other parameters were adjusted. Figure **8** illustrates that the experimental temperature dependence of the rates and KIEs can be reproduced for the fixed proton donor-acceptor distance of R = 2.7 Å. Note that this donor-acceptor distance is similar to the distance corresponding to the dominant contribution to the overall PCET rate calculated with Eq. **7** but is considerably smaller than the equilibrium donor-acceptor distance for this model.

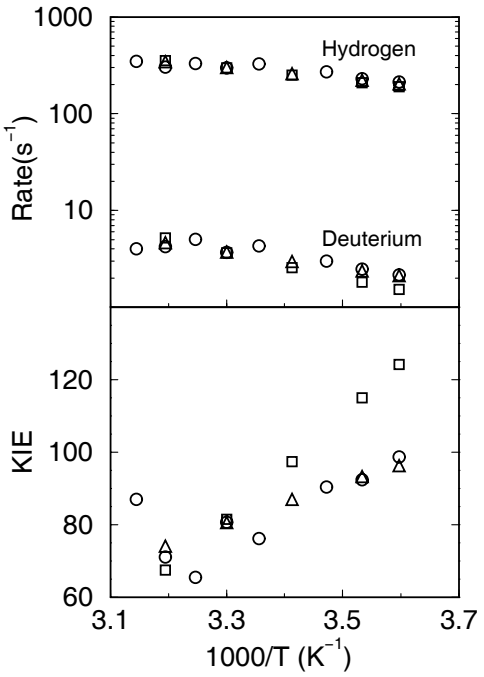

Figure **8**: Temperature dependence of the rates and KIEs for multistate continuum theory calculations with a fixed proton donor-acceptor distance. The experimental data are denoted with circles. The theoretical results were generated with fixed proton donor-acceptor distances of R = 2.7 Å (triangles), and 2.8 Å (squares).

Figure **8** also illustrates that the experimental temperature dependence of the KIEs is not reproduced for the fixed proton donor-acceptor distance R = 2.8 Å. Specifically, the slope of the KIE as a function of 1/T is much larger for R = 2.8 Å. For shorter proton donor-acceptor distances, the temperature dependence of the KIE is weaker than the experimentally observed temperature dependence. For the fixed proton donor-acceptor distance of R = 2.6 Å, we were unable to reproduce the high KIE of 81 at T=303 K due to the large overlap between the reactant and product hydrogen vibrational wavefunctions at this shorter distance. Analysis of the terms in the rate expression indicates that at larger proton donor-acceptor distances, the excited vibronic states contribute more significantly to the overall rate. In general, the relative contributions of the vibronic states are

determined by a competition between the coupling, which favors the higher states, and the free energy barrier, which favors the lower states in the normal Marcus region. As the proton donor-acceptor distance increases, the coupling for the lowest energy reactant and product states decreases due to the averaging over the reactant and product vibrational wavefunctions, thereby leading to greater contributions from the excited vibronic states. Moreover, the relative contributions of the excited states are different for hydrogen and deuterium and depend strongly on the temperature. This analysis suggests that the proton donor-acceptor vibrational motion plays a vital role in decreasing the dominant proton donor-acceptor distance relative to its equilibrium value to facilitate the reaction.

Quantum treatment of donor-acceptor motion

We have also performed multistate continuum theory calculations in which the donor-acceptor vibrational motion is treated quantum mechanically.[26] In this case, the vibrational wavefunctions depend on the hydrogen coordinate r and the proton donor-acceptor distance R, and the rate expression has the same general form as Eq. **1** . Figure **9** depicts the results obtained with the quantum treatment of the donor-acceptor mode for two different parameter sets. For the original parameter set used to generate Figure **5** with the classical treatment of the donor-acceptor mode, the quantum treatment slightly overestimates the rates and underestimates the KIEs, but the temperature dependence of the rates and KIE agrees well with the experimental data and the classical treatment of the donor-acceptor mode. When the couplings V^{ET} and V^{PT} were adjusted slightly (V^{ET} = 0.022 kcal/mol and V^{PT} = 18.25 kcal/mol) to fit the experimental rate and KIE at T = 303 K, the results obtained with the quantum treatment of the donor-acceptor mode agree well with the experimental data.

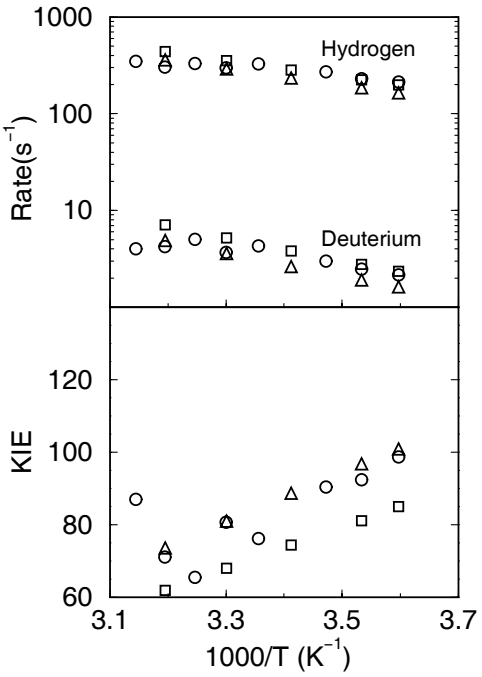

Figure **9**: Temperature dependence of the rates and KIEs for multistate continuum theory calculations with a quantum treatment of the proton donor-acceptor vibrational motion. The experimental data are denoted with circles. The theoretical results were generated with two different parameter sets: the same parameters as were used to generate Figure **5** (squares) and the same parameters except that the couplings were slightly modified so that these quantum results reproduced the experimental rate and KIE at 303 K (triangles).

Parameter dependence

We investigated the dependence of the results on the reorganization energies. As mentioned above, the outer-sphere reorganization energy was calculated with the FRCM method for several different conformations corresponding to proton donor-acceptor distances of R = 2.8-3.2 Å. The diabatic outer-sphere reorganization energies for EPT were found to be the same to within 0.3 kcal/mol for these different conformations. The

calculation of the inner-sphere reorganization energy of 19.1 kcal/mol is not straightforward because it is based on relatively small changes in bond lengths for DFT calculations and neglects the inner-sphere reorganization energy of the linoleic acid. Figure **10** depicts the rates and KIEs for inner-sphere reorganization energies of λ_{in} = 10 kcal/mol and λ_{in} = 30 kcal/mol. The temperature dependence of the KIE is reproduced reasonably well for inner-sphere reorganization energies in the range λ_{in} = 10-30 kcal/mol, although the slope increases slightly as the inner-sphere reorganization energy increases. The magnitude of the slope of the temperature dependence of the rates increases as the inner-sphere reorganization energy increases mainly due to an increase in the free energy barrier.

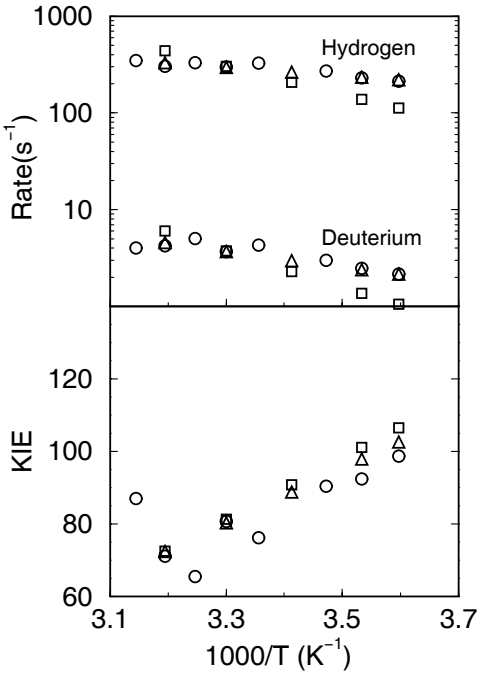

Figure **10**: Temperature dependence of the rates and KIEs for multistate continuum theory calculations with a classical treatment of the proton donor-acceptor vibrational motion. The experimental data are denoted with circles. The theoretical calculations use the original parameter set with the inner-sphere reorganization energy modified to be λ_{in} = 10 kcal/mol (triangles) and λ_{in} = 30 kcal/mol (squares). The equilibrium C–O distance and frequency are R_I^o = 2.88 Å and ω_I^o = 511 cm^{-1} and the dominant C–O distance is R_{dom} = 2.69 Å.

We also investigated the dependence of the results on the gas phase EVB potential parameters. The C–H and O–H Morse parameters are determined by experimentally determined frequencies, bond lengths, and dissociation energies. Variation of these parameters within the physically reasonable range does not significantly influence the results. On the other hand, the results are sensitive to the C–O equilibrium distances and frequencies on the free energy surfaces representing the reactant and product vibronic states. These properties of the free energy surfaces are determined mainly by the Fe–O and π–C force constants and the C–O Morse parameters.

We emphasize that the C–O equilibrium distances and frequencies on the free energy surfaces are not determined solely by the C–O Morse parameters but rather are strongly influenced by the other terms in the EVB potential such as the Fe–O and π–C frequencies. We performed a detailed analysis based on systematic variation of these parameters.

For the first model studied, the Fe–O and π–C force constants were chosen to correspond to physically reasonable frequencies for those types of modes. For these parameter values, the results were relatively insensitive to the choice of the C–O Morse parameter β_{CO} because the Fe–O and π–C force constants dominated the overall C–O frequency. The temperature dependence of the rates and KIEs are reproduced for β_{CO} = 1.21-3.62 $Å^{-1}$, which corresponds to C–O Morse frequencies of 200-600 cm^{-1} and C–O frequencies on the free energy surfaces of ω_I^o = 460-580 cm^{-1}. Although the results are relatively insensitive to β_{CO} for these Fe–O and π–C force constants, the results are very sensitive to the value of the C–O Morse parameter R_{CO}^o, which influences the equilibrium C–O distance. Figure **11** illustrates that the slope of the temperature dependence of the KIE is too large for R_{CO}^o = 3.0 Å, which corresponds to an equilibrium C–O distance on the free energy surface of R_I^o = 3.05 Å. In this case, the dominant proton donor-acceptor distance contributing to the rate is R_{dom} = 2.79 Å, which is significantly larger than the dominant distance of R_{dom} = 2.69 Å for the original parameter set. We found that the slope of the temperature dependence of the KIE increases as the dominant proton donor-acceptor distance increases because the contributions of the excited vibronic states increase for larger distances. The physical basis for this observation is described above in the discussion of the calculations with fixed proton donor-acceptor distances.

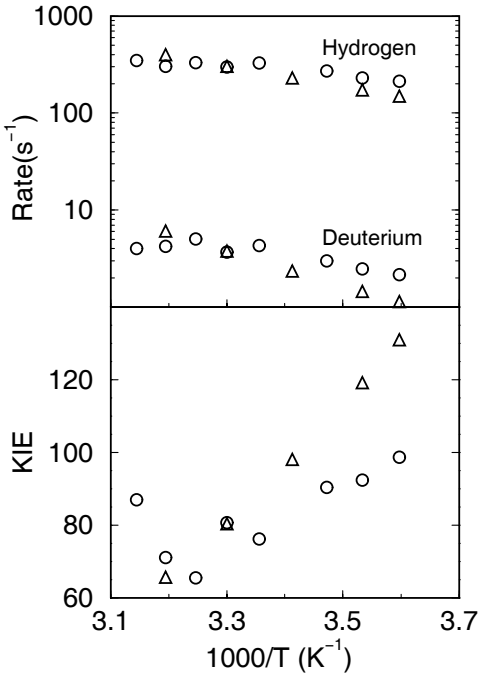

Figure **11**: Temperature dependence of the rates and KIEs for multistate continuum theory calculations with a classical treatment of the proton donor-acceptor vibrational motion. The experimental data are denoted with circles. The theoretical calculations use the original parameter set with the C–O Morse parameter R_{CO}^{o} modified to be R_{CO}^{o} = 3.0 Å (triangles). In all cases, the couplings V^{ET} and V^{PT} were fit to the experimental rate and KIE at T=303 K. The equilibrium C–O distance and frequency are R_{I}^{o} = 3.02 Å and ω_{I}^{o} = 519 cm^{-1} and the dominant C–O distance is R_{dom} = 2.79 Å.

Alternative model

We have also developed an alternative model that allows larger equilibrium C–O distances. As discussed above, the equilibrium C–O distance and frequency are R_{I}^{o} = 2.88 Å and ω_{I}^{o} = 511 cm^{-1} in the first model studied. This equilibrium C–O distance of R_{I}^{o} = 2.88 Å is significantly smaller than the sum of the corresponding van der Waals radii of

~3.2 Å. In the alternative model, the harmonic terms $U_{\mathrm{FeO}}^{\mathrm{harm}}$ and $U_{\pi\mathrm{C}}^{\mathrm{harm}}$ are chosen to be relatively small and are not associated with any physical properties. In this case, the equilibrium C–O frequency on the free energy surface is determined mainly by the frequency associated with the C–O Morse potential (i.e., the parameter β_{CO}) and represents an effective frequency resulting from motions of the substrate, protein, and iron complex. We found that the equilibrium C–O frequency must be decreased significantly to fit the data for larger equilibrium C–O distances. The outer-sphere reorganization energies were calculated for a conformation with a C–O distance of 3.0 Å. The couplings V^{ET} and V^{PT} were fit to the experimental rate and KIE, respectively, at T = 303 K. Figure **12** depicts the results obtained with this alternative model, in which the equilibrium C–O distance and frequency are $R_{\mathrm{I}}^{\mathrm{o}}$ = 3.05 Å and $\omega_{\mathrm{I}}^{\mathrm{o}}$ = 284 cm^{-1}, respectively, on the lowest energy reactant free energy surface. The dominant proton donor-acceptor distance contributing to the rate is R_{dom} = 2.69 Å, which is identical to the dominant distance for the smaller equilibrium C–O distance of $R_{\mathrm{I}}^{\mathrm{o}}$ = 2.88 Å. These results indicate that the temperature dependence of the KIE can be reproduced by larger equilibrium C–O distances if the C–O frequency is low enough to allow the dominant distance contributing to the rate to be $R_{\mathrm{dom}} \approx 2.7$ Å. As discussed above, the dominant distance is determined by a balance between the coupling and the Boltzmann probability.

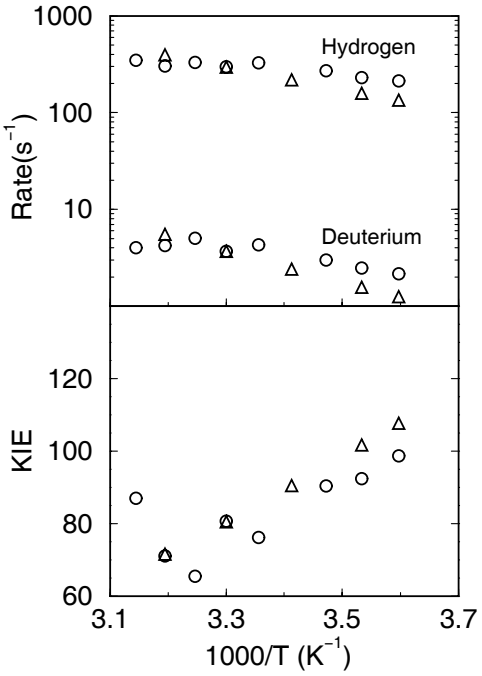

Figure **12**: Temperature dependence of the rates and KIEs for multistate continuum theory calculations with a classical treatment of the proton donor-acceptor vibrational motion. The experimental data are denoted with circles, and the theoretical results are denoted with triangles. The calculations use the original parameter set with the following modifications: the solvent reorganization energies are calculated for a conformation with a C–O distance of 3.0 Å, R_{CO}^{o} = 3.0 Å, β_{CO} = 1.8 Å^{-1} corresponding to a C–O Morse frequency of 299 cm^{-1}, Fe–O force constant of 25 kcal mol^{-1} Å^{-2}, π–C force constant of 100 kcal mol^{-1} Å^{-2}, and the couplings V^{ET} and V^{PT} were fit to the experimental rate and KIE at T=303 K. The equilibrium C–O distance and frequency are R_{l}^{o} = 3.05 Å and ω_{l}^{o} = 284 cm^{-1} and the dominant C–O distance is R_{dom} = 2.69 Å.

Comparison to previous calculations

Previously Klinman and coworkers[12] applied a simpler tunneling theory to this reaction. This previous application used an equation[48] based on Marcus theory for ET with only two electronic states, rather than the four diabatic electronic states used in the multistate continuum theory for PCET. In the two-state formulation,[22,23] the

reorganization energies and reaction free energies are assumed to be the same for all pairs of vibronic states, and the electronic coupling is separable from the proton vibrational wavefunctions. In the four-state formulation,[17,18] the reorganization energies and reaction free energies differ for each pair of vibronic states because of variations in the relative weights of the PT diabatic states, and the electronic coupling is not rigorously separable from the proton vibrational wavefunctions because it depends on the proton coordinate.

The present approach differs from Klinman and coworkers' approach in the treatment of the proton coordinate. In Klinman and coworkers' approach,[12] the proton potential is assumed to be harmonic with the same frequency for both the reactant and product. Thus, the overlap reduces to an integral over harmonic oscillator wavefunctions, and the energies of the proton vibrational states are assumed to be equally spaced. This previous approach neglects changes in the shape of the proton potential (i.e., the tunneling barrier) due to the proton donor-acceptor vibrational motion. In the present approach, however, each diabatic state includes a Morse potential for the donor-hydrogen or acceptor-hydrogen motion, and the overall potential energy surface is a mixture of these diabatic states. Thus, the potential energy surface includes the anharmonicity of the hydrogen motion and provides a physically reasonable description of the dependence of the barrier on the proton donor-acceptor distance. Moreover, in the present formulation the coupling is calculated by numerical integration of Eq. **6** and includes the dependence of the electronic coupling on the proton coordinate as well as the anharmonic effects in the vibrational wavefunctions. The reorganization energies and reaction free energies are calculated numerically for each vibronic state without the assumption of equal spacing for the energies of the hydrogen vibrational states.

The present approach also differs significantly from Klinman and coworkers' approach in the treatment of the proton donor-acceptor mode, which is denoted the "gating" coordinate in Ref. 12. In Klinman and coworkers' approach,[12] only the Franck-Condon overlap term depends on the gating coordinate, and the motion of the gating coordinate is assumed to be harmonic. In the present formulation, the overall free energy surfaces depend on the proton donor-acceptor distance because diagonal and off-diagonal gas phase valence bond matrix elements depend on the donor-acceptor coordinate. Thus,

the reorganization energies, reaction free energies, and couplings in the rate expression depend on the proton donor-acceptor distance. Moreover, the anharmonicity of the donor-acceptor motion is included by using a Morse potential to describe the proton donor-acceptor motion in the diabatic states. In addition, Klinman and coworkers treated the gating mode classically, whereas we performed calculations with both classical and quantum treatments of the proton donor-acceptor mode.

The parameterization of the potential energy term describing the donor-acceptor motion also differs for the two approaches. Klinman and coworkers[12] represent the gating mode with a mass of 110 g/mol, corresponding to the mass of an amino acid, and a frequency of 400 cm^{-1}. The present calculations represent the donor-acceptor mode with a mass of 6.86 g/mol, corresponding to the reduced mass of carbon and oxygen, and a frequency of 300-500 cm^{-1}. The force constant used in Klinman and coworkers' calculations is more than a factor of ten larger than the effective force constant based on the second derivative of the free energy surface with respect to the donor-acceptor distance used in the present calculations. Thus, the motion is much stiffer for the gating mode in Klinman's calculations than for the donor-acceptor mode in the present calculations. As a result of this stiffer motion of the gating mode, the equilibrium tunneling distance (defined in Ref. 12 as the separation between the minima of the donor and acceptor wells along the hydrogen coordinate) is required to be smaller in Klinman and coworkers' calculations than in the present calculations. Klinman and coworkers' calculations required a donor-acceptor distance of 2.8 Å, whereas we are able to reproduce the experimental temperature dependence with an equilibrium donor-acceptor distance of 3.1 Å in conjunction with an equilibrium donor-acceptor frequency of 300 cm^{-1}. Moreover, the equilibrium donor-acceptor distance can be increased further if the frequency is decreased within the framework of our theoretical formulation.

Many of the conclusions in the present paper are similar to those of Klinman and coworkers.[12] To fit the experimental kinetic data, Klinman and coworkers used a total reorganization energy of 19.5 kcal/mol, which is similar to our calculated value of 21.0 kcal/mol for the lowest energy reactant and product PCET states. Note that we calculated the inner-sphere and outer-sphere reorganization energies independently with quantum

mechanical methods. Klinman and coworkers were also able to fit the temperature dependence of the KIE without inclusion of the proton donor-acceptor vibrational motion if they used a shorter hydrogen transfer distance.

Several central conclusions from the work of Klinman and coworkers[12] differ substantially from the conclusions of the present work. Klinman and coworkers conclude that the rates and KIEs will become more temperature dependent as the gating frequency decreases because a larger range of donor-acceptor distances will be thermally accessible for lower frequencies. According to Ref. 12, decreasing the frequency of the gating mode increases the temperature dependence of the tunneling distance, which is different for hydrogen and deuterium, leading to a greater temperature-dependence of the KIE. Their model indicates that an extremely stiff gating frequency is required to reproduce the experimental data for wild-type SLO (i.e., gating does not significantly modulate the hydrogen transfer distance). Thus, they conclude that the active site for wild-type SLO is highly preorganized with a relatively short proton donor-acceptor distance. In the present work, the temperature dependence of the KIE is found to be strongly influenced by the donor-acceptor distance with the dominant contribution to the overall rate. The KIE becomes more temperature dependent as this dominant distance increases because excited vibronic states play a greater role at larger distances. The relative contributions of these excited states depend strongly on temperature and vary for hydrogen and deuterium. Within the framework of our theoretical formulation, the dominant distance depends on the equilibrium donor-acceptor distance and frequency. For a physically reasonable equilibrium donor-acceptor distance, the temperature dependence of the KIE increases as the frequency increases because the dominant donor-acceptor distance increases (i.e., smaller donor-acceptor distances are not thermally accessible). We are able to reproduce the experimental data for wild-type SLO with a larger equilibrium donor-acceptor distance by decreasing the corresponding frequency. We conclude that the relatively low-frequency donor-acceptor vibrational motion is critical in SLO to decrease the donor-acceptor distance from its equilibrium value to allow hydrogen tunneling.

Solomon and Lehnert also used computational methods to study this reaction.[11] As mentioned above, their density functional theory calculations indicate that the reaction

occurs through a PCET mechanism in which the electron transfers from the π system of the substrate to the iron as the proton transfers from the carbon to the oxygen. This conclusion is consistent with the thermodynamic analysis presented in the appendices. Solomon and Lehnert also observed that the calculated energy barriers for this process depend strongly on the proton donor-acceptor distance. The calculated barrier for hydrogen transfer is 30 kcal/mol at the stated crystallographic donor-acceptor distance of 3.0 Å, but protein fluctuations are expected to decrease the distance and thereby lower the barrier. Solomon and Lehnert hypothesize that the hydrogen transfer reaction in SLO occurs at a donor-acceptor distance of ~2.7 Å with a barrier of 15 kcal/mol including zero point energy corrections. A simple hydrogen tunneling model is used to explain the small activation energy that was observed experimentally. The hydrogen transfer donor-acceptor distance proposed by Solomon and Lehnert[11] is consistent with the results of the present work.

Conclusions

In this paper, we applied a multistate continuum theory to the PCET reaction catalyzed by the enzyme SLO. The inner-sphere reorganization energy of the iron cofactor for the PCET reaction was estimated to be ~19 kcal/mol based on DFT B3LYP calculations on a model system. The diabatic outer-sphere reorganization energy of the protein for EPT was calculated to be 2.4 kcal/mol with the frequency resolved cavity model for a conformation obtained from docking simulations. These calculations indicate that the inner-sphere reorganization energy is significantly larger than the outer-sphere reorganization energy of the protein for this process. The free energy of reaction for PCET was estimated to be −5.4 kcal/mol from experimentally determined thermodynamic properties. In contrast, the free energies of reaction for ET and PT were estimated to be substantially endothermic. This thermodynamic analysis implies that the electron and proton transfer simultaneously rather than sequentially. The reorganization

energies and estimated reaction free energies were used in conjunction with the multistate continuum theory to calculate the rates and KIEs for the PCET reaction.

The temperature dependence of the calculated rates and KIEs is in agreement with the experimental data. A detailed analysis of the terms in the PCET rate expression provides further insight into the mechanism. The lowest energy reactant and product vibronic states were found to represent the dominant contribution to the overall rate. The weak temperature dependence of the rates is due to a relatively small free energy barrier, which derives from a balance between the total reorganization energy and the reaction free energy. The temperature dependence of the rates was found to increase for larger values of the inner-sphere reorganization energy mainly due to an increase in the free energy barrier. The unusually high KIE of 81 results from the small overlap of the reactant and product proton vibrational wavefunctions and the dominance of the lowest energy reactant and product vibronic states in the hydrogen tunneling process.

We also investigated the role of the proton donor-acceptor vibrational motion in this PCET reaction. The effects of the proton donor-acceptor vibrational motion were examined with both a classical treatment involving thermal averaging over the donor-acceptor distances and a quantum mechanical treatment of the donor-acceptor mode. The results obtained from the classical and quantum treatments were qualitatively similar. Thus, the quantum mechanical effects associated with the donor-acceptor mode are not critical for the description of the temperature dependence of the rates and KIEs. For the classical treatment, the dominant contribution to the overall PCET rate was found to correspond to a proton donor-acceptor distance that is considerably smaller than the equilibrium donor-acceptor distance in this model. Analysis of the results indicates that the dominant proton donor-acceptor distance is determined by a balance between the larger coupling and the smaller Boltzmann probability as the distance decreases. For comparison, we also performed calculations for fixed proton donor-acceptor distances. We found that the temperature dependence of the rates and KIEs could be reproduced with a fixed proton donor-acceptor distance that is similar to the dominant distance in the calculations including the proton donor-acceptor vibrational motion. On the other hand, we were unable to reproduce the temperature dependence of the KIEs with the larger

equilibrium proton donor-acceptor distance for this model. Our analysis indicates that the experimental temperature dependence cannot be reproduced with the proton donor-acceptor distance fixed at its equilibrium value due to the increased contributions of the excited vibronic states for the larger donor-acceptor distances. The relative contributions of these excited states are different for hydrogen and deuterium and vary significantly with temperature.

Thus, this study illustrates that the proton donor-acceptor vibrational motion plays a vital role in decreasing the dominant donor-acceptor distance relative to its equilibrium value to facilitate the PCET reaction. We reproduced the experimentally determined temperature dependence of the rates and KIEs with two different models. In the first model, the equilibrium C–O distance and frequency are 2.9 Å and 500 cm^{-1}, respectively. In the second model, the equilibrium C–O distance and frequency are 3.1 Å and 300 cm^{-1}, respectively. For both models, the proton donor-acceptor distance with the dominant contribution to the overall rate is 2.7 Å. For the range of temperatures studied, the temperature dependence of the KIE is determined largely by this dominant donor-acceptor distance. The dominant distance is determined by numerous factors, including the equilibrium donor-acceptor distance and frequency. Within the framework of this theoretical formulation, the frequency of the donor-acceptor vibrational mode must be decreased as the equilibrium donor-acceptor distance is increased to maintain the same dominant donor-acceptor distance for the overall rate.

These calculations lead to several general predictions concerning the rates and KIEs of PCET reactions in enzymes. The temperature dependence of the rates is determined mainly by the free energy barrier, which depends on the reorganization energy and the reaction free energy. The magnitude of the KIE increases as the overlap between the reactant and product hydrogen vibrational wavefunctions decreases and the contributions of excited vibronic states decrease. As the proton donor-acceptor distance increases, typically the overlap between the reactant and product hydrogen vibrational wavefunctions decreases and the contributions of excited vibronic states increase. Thus, the magnitude of the KIE is determined by a complex balance of numerous factors, including the dominant proton donor-acceptor distance, the reorganization energy, the

reaction free energy, and the electronic couplings. Similarly, the temperature dependence of the KIE is strongly influenced by the dominant proton donor-acceptor distance but also depends on other factors such as the reorganization energy, reaction free energy, and electronic couplings.

Although these model calculations provide insight into the fundamental principles of the PCET reaction catalyzed by SLO, a number of important issues remain unresolved. The detailed mechanism by which the protein environment facilitates the PCET reaction is not well understood. Moreover, the role of dynamical effects in this reaction has not been investigated. Hybrid quantum/classical molecular dynamics simulations including the explicit protein can be used to address these issues. In addition, these types of simulations may be used to elucidate the impact of enzyme mutations on the overall reaction.

References

(1) Samuelsson, B.; Dahlen, S.-E.; Lindgren, J.; Rouzer, C. A.; Serhan, C. N. *Science* **1987**, *237*, 1171.

(2) Holman, T. R.; Zhou, J.; Solomon, E. L. *Journal of the American Chemical Society* **1998**, *120*, 12564.

(3) Steele, V. E.; Holmes, C. A.; Hawk, E. T.; Kopelovich, L.; Lubet, R. A.; Crowell, J. A.; Sigman, C. C.; Kelloff, G. J. *Cancer, Epidemiology, Biomarkers, & Prevention* **1999**, *8*, 467.

(4) Rioux, N.; Castonguay, A. *Carcinogenesis* **1998**, *19*, 1393.

(5) Nie, D.; Hillman, G. G.; Geddes, T.; Tang, K.; Pierson, C.; Grignon, D. J.; Honn, K. V. *Cancer Research* **1998**, *58*, 4047.

(6) Ghosh, J.; Myers, C. E. *Proc. Natl. Acad. Sci. USA* **1998**, *95*, 13182.

(7) Rickert, K. W.; Klinman, J. P. *Biochemistry* **1999**, *38*, 12218.

(8) Lewis, E. R.; Johansen, E.; Holman, T. R. *Journal of the American Chemical Society* **1999**, *121*, 1395.

(9) 0001.

(10) Glickman, M. H.; Klinman, J. P. *Biochemistry* **1995**, *34*, 14077.

(11) Lehnert, N.; Solomon, E. L. *J. Biol. Inorg. Chem.* **2003**, *8*, 294.

(12) Knapp, M. J.; Rickert, K. W.; Klinman, J. P. *Journal of the American Chemical Society* **2002**, *124*, 3865.

(13) Jonsson, T.; Glickman, M. H.; Sun, S.; Klinman, J. P. *Journal of the American Chemical Society* **1996**, *118*, 10319.

(14) Glickman, M. H.; Wiseman, J. S.; Klinman, J. P. *Journal of the American Chemical Society* **1994**, *116*, 793.

(15) Hwang, C.-C.; Grissom, C. B. *Journal of the American Chemical Society* **1994**, *116*, 795.

(16) Knapp, M. J.; Seebeck, F. P.; Klinman, J. P. *Journal of the American Chemical Society* **2001**, *123*, 2931.

(17) Soudackov, A.; Hammes-Schiffer, S. *Journal of Chemical Physics* **1999**, *111*, 4672.

(18) Soudackov, A.; Hammes-Schiffer, S. *Journal of Chemical Physics* **2000**, *113*, 2385.

(19) Hammes-Schiffer, S. *Accounts of Chemical Research* **2001**, *34*, 273.

(20) Basilevsky, M. V.; Rostov, I. V.; Newton, M. D. *Chemical Physics* **1998**, *232*, 189.

(21) Newton, M. D.; Basilevsky, M. V.; Rostov, I. V. *Chemical Physics* **1998**, *232*, 201.

(22) Cukier, R. I. *Journal of Physical Chemistry* **1996**, *100*, 15428.

(23) Cukier, R. I.; Nocera, D. G. *Annual Reviews of Physical Chemistry* **1998**, *49*, 337.

(24) Mayer, J. M.; Hrovat, D. A.; Thomas, J. L.; Borden, W. T. *Journal of the American Chemical Society* **2002**, *124*, 11142.

(25) 0002.

(26) Soudackov, A. V.; Hatcher, E.; Hammes-Schiffer, S. *Journal of Chemical Physics* **2005**, *122*, 014505.

(27) Zhou, Z.; Khan, S. U. M. *Journal of Physical Chemistry* **1989**, *93*, 5292.

(28) Warshel, A. *Computer Modeling of Chemical Reactions in Enzymes and Solutions*; John Wiley & Sons, Inc.: New York, 1991.

(29) Lee, C.; Yang, W.; Parr, P. G. *Physical Review B* **1988**, *45*, 785.

(30) Becke, A. D. *Journal of Chemical Physics* **1993**, *98*, 5648.

(31) Dunning, J., T. H.; Hay, P. J. *Modern Theoretical Chemistry*; Plenum: New York, 1976; Vol. 3.

(32) Hay, P. J.; Wadt, W. R. *Journal of Chemical Physics* **1984**, *82*, 270.

(33) Frisch, M. J.; Trucks, G. W.; Schlegel, H. B.; Scuseria, G. E.; Robb, M. A.; Cheeseman, J. R.; Zakrzewski, V. G.; Montgomery, J., J. A.; Stratmann, R. E.; Burant, J. C.; Dapprich, S.; Millam, J. M.; Daniels, A. D.; Kudin, K. N.; Strain, M. C.; Farkas, O.; Tomasi, J.; Barone, V.; Cossi, M.; Cammi, R.; Mennucci, B.; Pomelli, C.; Adamo, C.; Clifford, S.; Ochterski, J.; Petersson, G. A.; Ayala, P. Y.; Cui, Q.; Morokuma, K.; Malick, D. K.; Rabuck, A. D.; Raghavachari, K.; Foresman, J. B.; Cioslowski, J.; Ortiz, J. V.; Babou, A. G.; Stefanov, B. B.; Liu, G.; Liashenko, A.; Piskorz, P.; Komaromi, I.; Gomperts, R.; Martin, R. L.; Fox, D. J.; Keith, T.; Al-Laham, M. A.; Peng, C. Y.; Nanayakkara, A.; Gonzalez, C.; Challacombe, M.; Gill, P. M. W.; Johnson, B.; Chen, W.; Wong, M. W.; Andres, J. L.; Gonzales, C.; Head-Gordon, M.; Replogle, E. S.; Pople, J. A. Gaussian 98, Revision A.7; Gaussian, Inc.: Pittsburgh, PA, 1998.

(34) Borowski, T.; Krol, M.; Chruszcz, M.; Broclawik, E. *Journal of Physical Chemistry B* **2001**, *105*, 12212.

(35) Olson, M. A.; Reinke, L. T. *Proteins: Structure, Function, and Genetics* **2000**, *38*, 115.

(36) Morris, G. M.; Goodsell, D. S.; Halliday, R. S.; Huey, R.; Hart, W. E.; Belew, R. K.; Olson, A. J. *Journal of Computational Chemistry* **1998**, *19*, 1639.

(37) Tomchick, D. R.; Phan, P.; Cymbrowski, M.; Minor, W.; Holman, T. R. *Biochemistry* **2001**, *40*, 7509.

(38) Skrzypczak-Jankun, E.; Bross, R. A.; Carroll, R. T.; Dunham, W. R.; Funk, J. M. O. *Journal of the American Chemical Society* **2001**, *123*, 10814.

(39) Breneman, C. M.; Wiberg, K. B. *Journal of Computational Chemistry* **1990**, *11*, 361.

(40) Kuntz, P. J.; Nemeth, E. M.; Polanyi, J. C.; Rosner, S. D.; Young, C. E. *Journal of Chemical Physics* **1966**, *44*, 1168.

(41) Kim, Y.; Truhlar, D. G.; Kreevoy, M. M. *Journal of the American Chemical Society* **1991**, *113*, 7837.

(42) Basilevsky, M. V.; Soudackov, A. V.; Vener, M. V. *Chemical Physics* **1995**, *200*, 87.

(43) Scott, A. P.; Radom, L. *Journal of Physical Chemistry* **1996**, *100*, 16502.
(44) Glasstone, S.; Laidler, K. J.; Eyring, H. *The Theory of Rate Processes*; McGraw-Hill: New York, 1941.
(45) 0003.
(46) Bu, Y.; Liu, S.; Song, X. *Chemical Physics Letters* **1994**, *227*, 121.
(47) Iordanova, N.; Hammes-Schiffer, S. *Journal of the American Chemical Society* **2002**, *124*, 4848.
(48) Kuznetsov, A. M.; Ulstrup, J. *Canadian Journal of Chemistry* **1999**, *77*, 1085.

Chapter 3

Quantum and Dynamical Effects of Proton Donor-Acceptor Vibrational Motion in Nonadiabatic Proton-Coupled Electron Transfer Reactions

Introduction

Proton-coupled electron transfer (PCET) reactions continue to attract attention from experimentalists and theoreticians working in many areas of modern chemistry, biochemistry, and chemical physics. Processes involving PCET as one of the key steps are being studied extensively in enzymes,[1-4] photosynthetic reaction centers[5] and various biomimetic reaction systems.[6-12] From a theoretical perspective, PCET represents an important class of multiple charge transfer reactions in condensed phases. Despite many similarities to well-studied electron transfer (ET) and proton transfer (PT) processes, a theoretical description of PCET reactions presents unique challenges due to the quantum nature of the transferring particles (i.e., the electron and proton), the importance of nonadiabatic effects, and the wide range of timescales associated with the reaction.

Theoretical models of PCET reactions[13-20] address these fundamental issues and provide a theoretical foundation for the interpretation of experimental data. In our multistate continuum theory for PCET reactions,[17,18] the active electrons and transferring proton(s) are treated quantum mechanically, and the environment is represented by a dielectric continuum. This approach has provided insight into experimental data on the mechanisms and rates for a wide variety of chemically relevant PCET systems, including biomimetic metal complexes[21-24] and biological systems.[25-27] Until recently,[27] our

applications have not included the effects of the proton donor-acceptor vibrational motion, although this motion is known to strongly influence PT reactions.

The impact of the donor-acceptor distance on PT reactions is illustrated by the two-dimensional potential energy surface depicted in Figure **13**. The reaction path connecting the reactant and product minima through the saddle point is characterized by significant curvature, leading to strong dynamical coupling between the transferring proton and donor-acceptor coordinates in PT reactions. In addition, the characteristics of the PT profiles depend strongly on the donor-acceptor separation R. Specifically, the PT barrier decreases as the proton donor-acceptor distance R decreases. One of the most important implications of this feature is that the modulation of the PT barrier by the proton donor-acceptor vibrational motion significantly impacts the proton tunneling probability. In vibrationally nonadiabatic PT reactions, the nonadiabatic coupling between the reactant and product proton vibrational states depends strongly on the donor-acceptor distance. For these reasons, the effects of the proton donor-acceptor vibrational motion have been explicitly included in theoretical models for PT reactions in the condensed phase.[28-34]

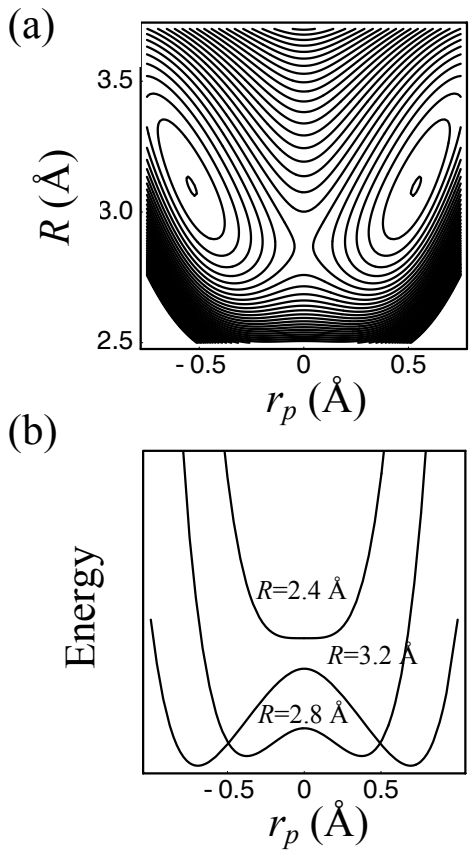

Figure **13**: (a) Two-dimensional potential energy surface for a typical proton transfer system as a function of the proton coordinate r_p and the proton donor-acceptor distance R. (b) Slices of this surface along the proton coordinate r_p at three different values of R.

In this paper, we present an extension of the multistate continuum theory for PCET reactions to include the effects of the proton donor-acceptor vibrational motion. Nonadiabatic PCET rate expressions are presented for the limits of a slow classical and a fast quantum donor-acceptor mode. An analytical nonadiabatic PCET rate expression that includes the dynamical fluctuations of the nonadiabatic PCET coupling is derived. The quantities in this rate expression can be determined from the gas phase potential energy surface and a dielectric continuum model. In addition, our theoretical formulation for PCET is generalized to a molecular representation of the environment, and the

corresponding dynamical nonadiabatic PCET rate expression involving time correlation functions is derived. Under specified well-defined conditions, this rate expression enables the calculation of the PCET rate with molecular dynamics simulations of the full solvent or protein system in the reactant state.

An outline of the paper is as follows. In Section II, we review a general formulation of the multistate PCET theory. Section III is devoted to the derivation of the nonadiabatic rate expressions for PCET in various limits for both the explicit molecular and the dielectric continuum representations of the environment. We present illustrative rate calculations for a series of model PCET systems in Section IV and provide concluding remarks in Section V.

General Theoretical Formulation

A general PCET system is comprised of a solute immersed in a polar environment. The solute is characterized by coupled proton transfer (PT) and electron transfer (ET) reaction subsystems, and the polar environment may be a solvent or a complex protein. PCET systems involve a wide range of timescales associated with the motions of active electrons (i.e., the transferring electron in the ET subsystem and the bonding electrons in the PT subsystem), transferring proton(s), donor and acceptor groups, and solvent/protein electrons and nuclei.

In the present formulation, we restrict ourselves to the most important degrees of freedom in the system: the coordinates of the active electrons of the ET and PT subsystems ($\mathbf{r}_e$), the coordinates characterizing the PT interface (proton coordinate r_p and proton donor-acceptor separation R for a linear interface), and the set of coordinates corresponding to the solvent degrees of freedom (ξ). The electron donor and acceptor are assumed to be fixed in space, which is a reasonable approximation for systems in which the electron donor and acceptor consist of heavy groups such as metal complexes. Here we omit the coordinates corresponding to the uncoupled intramolecular vibrations of the solute, but the effects of these degrees of freedom are easily included at a later stage.[18, 35,

[36, 37] The solvent degrees of freedom can be further separated into fast electronic motions and slower inertial motions that correspond mainly to the nuclear degrees of freedom. In the present formulation, we adopt the Born-Oppenheimer approach,[38] which assumes that the solvent electronic degrees of freedom are infinitely fast and adiabatically separated from all other degrees of freedom.

The total Hamiltonian for the PCET system can be written as (Eq. **15**)

$$H_{\text{tot}} = T_p + T_R + T_\xi + H_{\text{el}}\left(r_p, R, \xi\right) \qquad \text{Eq. } \mathbf{15}$$

where T_p, T_R, and T_ξ are the kinetic energy operators for the coordinates r_p, R, and ξ, respectively, and H_{el} is an electronic Hamiltonian parametrically depending on these coordinates. The electronic Hamiltonian has the following form (Eq. **16**)

$$H_{\text{el}} = h_0\left(r_p, R\right) + W_{ss}\left(\xi\right) + W_\infty\left(r_p, R\right) + W_s\left(r_p, R, \xi\right) \qquad \text{Eq. } \mathbf{16}$$

where $h_0\left(r_p, R\right)$ is the gas-phase electronic Hamiltonian of the solute, $W_{ss}\left(\xi\right)$ accounts for the solvent-solvent interactions, $W_\infty\left(r_p, R\right)$ accounts for the interaction of the solute with the solvent electronic degrees of freedom (within the Born-Oppenheimer approximation), and $W_s\left(r_p, R, \xi\right)$ accounts for all interactions of the solute with the solvent inertial degrees of freedom (i.e., electrostatic and short-range interactions).

In our theoretical formulation for PCET,[17] the electronic structure of the solute is described in the framework of a four-state valence bond (VB) model. Four diabatic electronic basis states correspond to the charge transfer states in the coupled ET and PT subsystems. These four states are defined in Eq. **17**

$$\begin{aligned}
&(1a)\quad \mathrm{D_e^-}\cdots\cdots\mathrm{D_pH^+}\cdots\cdots\mathrm{A_p}\cdots\cdots\mathrm{A_e}\\
&(1b)\quad \mathrm{D_e^-}\cdots\cdots\mathrm{D_p}\cdots\cdots{}^{+}\mathrm{HA_p}\cdots\cdots\mathrm{A_e}\\
&(2a)\quad \mathrm{D_e}\cdots\cdots\mathrm{D_pH^+}\cdots\cdots\mathrm{A_p}\cdots\cdots\mathrm{A_e^-}\\
&(2b)\quad \mathrm{D_e}\cdots\cdots\mathrm{D_p}\cdots\cdots{}^{+}\mathrm{HA_p}\cdots\cdots\mathrm{A_e^-}
\end{aligned} \qquad \text{Eq. } \mathbf{17}$$

Given these four VB states, PT processes can be described as $1a \rightarrow 1b$ and $2a \rightarrow 2b$ transitions, ET processes as $1a \rightarrow 2a$ and $1b \rightarrow 2b$ transitions, and EPT processes as $1a \rightarrow 2b$ and $1a \rightarrow 2a$ transitions. Here EPT processes refer to concerted electron and proton transfer.

The general formulation for PCET can be represented in terms of a dielectric continuum environment or an explicit molecular environment. In both representations, the free energy of the PCET system can be calculated in terms of the solute coordinates r_p and R and two scalar solvent coordinates z_p and z_e corresponding to the PT and ET reactions, respectively. In both cases, the gas phase solute energy and the interaction of the solute with the electronic solvent polarization are represented in the four-state VB basis by the [4×4] matrix $\mathbf{H}_0\left(r_p, R\right)$, which has elements $\left(H_0\right)_{ij} = \left\langle \psi_i^{\mathrm{el}} \middle| h_0 + W_\infty \middle| \psi_j^{\mathrm{el}} \right\rangle$, where ψ_{1a}^{el}, ψ_{1b}^{el}, ψ_{2a}^{el}, and ψ_{2b}^{el} are the wavefunctions corresponding to the VB states defined in Eq. **17** . In this paper, we present formulations for both the continuum and the molecular representations of the environment.

In the dielectric continuum model for the environment, the solvent or protein is represented as a dielectric continuum characterized by the electronic (ε_∞) and inertial (ε_0) dielectric constants. The scalar solvent coordinates z_p and z_e represent the differences in electrostatic interaction energies of the charge densities $\rho_i\left(\mathbf{r}\right)$ (i = 1a, 1b, 2a, 2b) corresponding to the VB basis states involved in the PT and ET reactions, respectively, with the inertial polarization potential $\Phi_{\mathrm{in}}\left(\mathbf{r}\right)$ of the solvent. The scalar solvent coordinates z_p and z_e are given in Eq. **18**

$$\begin{aligned} z_p &= \int d\mathbf{r}\left[\rho_{1b}\left(\mathbf{r}\right) - \rho_{1a}\left(\mathbf{r}\right)\right]\Phi_{\mathrm{in}}\left(\mathbf{r}\right) \\ z_e &= \int d\mathbf{r}\left[\rho_{2a}\left(\mathbf{r}\right) - \rho_{1a}\left(\mathbf{r}\right)\right]\Phi_{\mathrm{in}}\left(\mathbf{r}\right) \end{aligned} \quad . \qquad \text{Eq. } \mathbf{18}$$

In general, these solvent coordinates depend on the solute coordinates r_p and R, but this dependence is usually very weak and can be neglected. Moreover, in the dielectric

continuum model, the short-range solute-solvent interactions are neglected. Using linear response theory, the VB matrix corresponding to the free energy is expressed in Eq. **19** [17]

$$\mathbf{H}_{\text{cont}} = S\left(z_p, z_e\right)\mathbf{I} + \mathbf{H}_0\left(r_p, R\right) + \begin{bmatrix} 0 & 0 & 0 & 0 \\ 0 & z_p & 0 & 0 \\ 0 & 0 & z_e & 0 \\ 0 & 0 & 0 & z_p + z_e \end{bmatrix}. \qquad \text{Eq. } \mathbf{19}$$

In the first term, **I** is the [4×4] unit matrix, and $S\left(z_p, z_e\right)$ is the transformed self-energy of the inertial solvent polarization. The self-energy is quadratic in z_p and z_e, and typically the dependence on the solute coordinates can be neglected. The second term $\mathbf{H}_0\left(r_p, R\right)$ includes the gas phase solute energy and the interaction of the solute with the electronic solvent polarization. The last term in Eq. **19** corresponds to the interaction between the solute and the inertial polarization of the solvent, with the elimination of the interaction of VB state 1*a* because this interaction is contained in the first term due to a coordinate transformation. As a result of the representation of the many solvent degrees of freedom by two collective solvent coordinates that depend on the inertial solvent polarization field potential, Eq. **19** corresponds to free energy rather than potential energy.[31] Since the dependence of z_p, z_e, and S on the solute coordinates is weak and therefore neglected, however, the matrix given in Eq. **19** can be regarded as the VB representation of the electronic Hamiltonian that provides the adiabatic potential energy surfaces for the solute nuclei. The adiabatic free energy surfaces for the solvent coordinates z_p and z_e can be obtained by diagonalization of the matrix in Eq. **19** .

In the molecular description of the solvent, the scalar coordinates z_p and z_e , given in Eq. **20** , are functions of the solvent coordinates ξ and can be defined in terms of the solute-solvent interaction potential $W_s\left(r_p, R, \xi\right)$ as:

$$\begin{aligned} z_p\left(\xi\right) &= \left\langle \psi_{1b}^{\text{el}} \middle| W_s \middle| \psi_{1b}^{\text{el}} \right\rangle - \left\langle \psi_{1a}^{\text{el}} \middle| W_s \middle| \psi_{1a}^{\text{el}} \right\rangle \\ z_e\left(\xi\right) &= \left\langle \psi_{2a}^{\text{el}} \middle| W_s \middle| \psi_{2a}^{\text{el}} \right\rangle - \left\langle \psi_{1a}^{\text{el}} \middle| W_s \middle| \psi_{1a}^{\text{el}} \right\rangle \end{aligned}. \qquad \text{Eq. } \mathbf{20}$$

This representation includes both electrostatic and short-range solute-solvent interactions. The electronic Hamiltonian within this description, shown in Eq. **21** , can be expressed in terms of the following matrix in the basis of the four VB states.[39]

$$\mathbf{H}_{\mathrm{mol}} = \left[W_{ss}(\xi) + \left\langle \psi_{1a}^{\mathrm{el}} \middle| W_s \middle| \psi_{1a}^{\mathrm{el}} \right\rangle \right] \mathbf{I} + \mathbf{H}_0(r_p, R) + \begin{bmatrix} 0 & 0 & 0 & 0 \\ 0 & z_p(\xi) & 0 & 0 \\ 0 & 0 & z_e(\xi) & 0 \\ 0 & 0 & 0 & z_p(\xi) + z_e(\xi) \end{bmatrix}. \quad \text{Eq. 21}$$

This Hamiltonian provides the adiabatic potential energy surfaces for all solute and solvent nuclei in the system and can be used in molecular dynamics simulations.[39] The adiabatic free energy surfaces as functions of the solvent coordinates z_p and z_e can be obtained by the calculation of the potential of mean force along these coordinates.

We have developed a theoretical formulation for the special case of PCET systems with nonadiabatic ET/EPT and electronically adiabatic PT. For these types of PCET systems, the electronic couplings between the PT states (1*a*/1*b* and 2*a*/2*b*) are larger than the thermal energy (i.e., $k_{\mathrm{B}}T$, where k_{B} is the Boltzmann constant and T is the temperature), whereas the electronic couplings between the ET states (1*a*/2*a* and 1*b*/2*b*) and between the EPT states (1*a*/2*b* and 1*b*/2*a*) are smaller than the thermal energy. In this case, we can adopt an ET-diabatic representation by splitting the [4×4] matrix $\mathbf{H}$ defined by Eq. **19** or Eq. **21** into two [2×2] matrices $\mathbf{H}^{\mathrm{I}}$ and $\mathbf{H}^{\mathrm{II}}$ corresponding to the 1*a*/1*b* and 2*a*/2*b* blocks, respectively. The reactant and product quantum states are then defined as eigenfunctions of the total Hamiltonian with H_{el} represented by matrices $\mathbf{H}^{\mathrm{I}}$ and $\mathbf{H}^{\mathrm{II}}$, respectively. Note that in this representation the reactant and product states correspond to distinct ET diabatic states (i.e., the transferring electron is localized on the donor for the reactant states and is localized on the acceptor for the product states). In this framework, the nonadiabatic PCET reaction is described in terms of nonadiabatic transitions between these reactant and product quantum states.

Rate Expression for Nonadiabatic PCET

In this section, we consider different treatments of the standard Golden Rule rate expression for various characteristics of the *R*-mode, thereby enabling us to derive analytical expressions for a wide range of nonadiabatic PCET reactions.

Thermodynamic averaging over a slow *R*-mode

First we consider the case in which the *R*-mode is characterized by a low frequency and is not dynamically coupled to the fluctuations of the solvent. The system is assumed to maintain an equilibrium distribution along the *R*-coordinate. In this case, we can exclude the *R*-mode from the dynamical description and consider an equilibrium ensemble of PCET systems with fixed proton donor-acceptor distances. The electrons and transferring proton are assumed to be adiabatic with respect to the *R*-coordinate and solvent coordinates within the reactant and product states. Thus, the reaction is described in terms of nonadiabatic transitions between two sets of intersecting free energy surfaces $\varepsilon_{\mu}^{\mathrm{I}}\left(R,z_{\mathrm{p}},z_{\mathrm{e}}\right)$ and $\varepsilon_{\nu}^{\mathrm{II}}\left(R,z_{\mathrm{p}},z_{\mathrm{e}}\right)$ corresponding to the reactant and product electron-proton vibronic states for fixed *R*. These electron-proton vibronic states are eigenfunctions of T_p+H_{el}, where H_{el} is represented by $\mathbf{H}^{\mathrm{I}}$ and $\mathbf{H}^{\mathrm{II}}$ for the reactant and product, respectively. The methodology for calculating these electron-proton vibronic free energy surfaces in a manner that includes the electron-proton nonadiabatic effects is described in Ref. 17. A pair of these surfaces for fixed *R* is depicted schematically in Figure **14** . The solvent coordinates $\left(\overline{z}_{\mathrm{p}}^{\mathrm{I}\mu},\overline{z}_{\mathrm{e}}^{\mathrm{I}\mu}\right)$ and $\left(\overline{z}_{\mathrm{p}}^{\mathrm{II}\nu},\overline{z}_{\mathrm{e}}^{\mathrm{II}\nu}\right)$ correspond to the minima of the free energy surfaces $\varepsilon_{\mu}^{\mathrm{I}}\left(R,z_{\mathrm{p}},z_{\mathrm{e}}\right)$ and $\varepsilon_{\nu}^{\mathrm{II}}\left(R,z_{\mathrm{p}},z_{\mathrm{e}}\right)$, respectively, for fixed *R*. For the derivation of the analytical rate expression, these two-dimensional surfaces are assumed to be harmonic along the z_p and z_e coordinates. For each fixed value of *R*, we recover

the nonadiabatic rate expression derived in our previous work (Eq. **22**) for the high-temperature limit of a Debye solvent:[18]

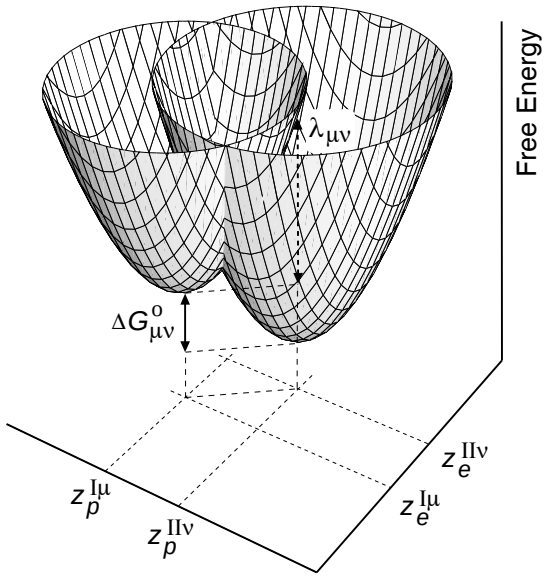

Figure **14**: Two-dimensional free energy surfaces corresponding to a pair of reactant and product electron-proton vibronic states as functions of the two scalar solvent coordinates z_p and z_e. The reorganization energy $\lambda_{\mu\nu}$ and the equilibrium free energy difference $\Delta G^0_{\mu\nu}$ are indicated.

$$k(R) = \frac{1}{\hbar}\sum_{\mu}^{\{\mathrm{I}\}} P_{\mu}^{\mathrm{I}}(R)\sum_{\nu}^{\{\mathrm{II}\}}\left|V_{\mu\nu}^{\neq}(R)\right|^2\sqrt{\frac{\pi\beta}{\lambda_{\mu\nu}(R)}}\exp\left\{-\frac{\beta\left[\Delta G^0_{\mu\nu}(R)+\lambda_{\mu\nu}(R)\right]^2}{4\lambda_{\mu\nu}(R)}\right\}. \qquad \text{Eq. } \mathbf{22}$$

Note that this expression has a similar form as the conventional rate expression for single ET.[40-46]

The quantities in Eq. **22** can be calculated from the two sets of free energy surfaces. The summations are over the electron-proton vibronic states associated with ET states 1 and 2, respectively, and P_{μ}^{I} is the Boltzmann probability for state $\mathrm{I}\mu$ defined in Eq. **23**

$$P_{\mu}^{\mathrm{I}}\left(R\right)=e^{-\beta\varepsilon_{\mu}^{\mathrm{I}}\left(R,\bar{z}_{p}^{\mathrm{I}\mu},\bar{z}_{e}^{\mathrm{I}\mu}\right)}\Big/\sum_{\nu}^{\{\mathrm{I}\}}e^{-\beta\varepsilon_{\nu}^{\mathrm{I}}\left(R,\bar{z}_{p}^{\mathrm{I}\nu},\bar{z}_{e}^{\mathrm{I}\nu}\right)}. \qquad \text{Eq. } \mathbf{23}$$

The reaction free energies $\Delta G_{\mu\nu}^{\mathrm{o}}$ and the solvent reorganization energies $\lambda_{\mu\nu}$ are calculated for each pair of reactant and product vibronic states. The reaction free energy is defined in Eq. **24**

$$\Delta G_{\mu\nu}^{0}\left(R\right)=\varepsilon_{\nu}^{\mathrm{II}}\left(R,\bar{z}_{\mathrm{p}}^{\mathrm{II}\nu},\bar{z}_{\mathrm{e}}^{\mathrm{II}\nu}\right)-\varepsilon_{\mu}^{\mathrm{I}}\left(R,\bar{z}_{\mathrm{p}}^{\mathrm{I}\mu},\bar{z}_{\mathrm{e}}^{\mathrm{I}\mu}\right), \qquad \text{Eq. } \mathbf{24}$$

and the solvent reorganization energy is defined in Eq. **25**

$$\lambda_{\mu\nu}\left(R\right)=\varepsilon_{\mu}^{\mathrm{I}}\left(R,\bar{z}_{\mathrm{p}}^{\mathrm{II}\nu},\bar{z}_{\mathrm{e}}^{\mathrm{II}\nu}\right)-\varepsilon_{\mu}^{\mathrm{I}}\left(R,\bar{z}_{\mathrm{p}}^{\mathrm{I}\mu},\bar{z}_{\mathrm{e}}^{\mathrm{I}\mu}\right)=\varepsilon_{\nu}^{\mathrm{II}}\left(R,\bar{z}_{\mathrm{p}}^{\mathrm{I}\mu},\bar{z}_{\mathrm{e}}^{\mathrm{I}\mu}\right)-\varepsilon_{\nu}^{\mathrm{II}}\left(R,\bar{z}_{\mathrm{p}}^{\mathrm{II}\nu},\bar{z}_{\mathrm{e}}^{\mathrm{II}\nu}\right). \qquad \text{Eq. } \mathbf{25}$$

The coupling $V_{\mu\nu}^{\neq}\left(R\right)$, expressed in Eq. **26** , is evaluated at the crossing points $z_{p}^{\neq},z_{e}^{\neq}$ along the straight line connecting the minima of the reactant and product surfaces and are assumed to be independent of solvent coordinates (i.e., the Condon approximation):

$$V_{\mu\nu}^{\neq}\left(R\right)=\left\langle \Phi_{\mu}^{\mathrm{I}}\left(\mathbf{r}_{e},r_{p}\mid R,z_{p}^{\neq},z_{e}^{\neq}\right)\middle|T_{p}+H_{\mathrm{el}}\middle|\Phi_{\nu}^{\mathrm{II}}\left(\mathbf{r}_{e},r_{p}\mid R,z_{p}^{\neq},z_{e}^{\neq}\right)\right\rangle , \qquad \text{Eq. } \mathbf{26}$$

where Φ_{μ}^{I} and Φ_{ν}^{II} , respectively, are the reactant and product electron-proton vibronic wavefunctions, and H_{el} is represented in the four-state VB basis by Eq. **19** .

In this regime, all of the quantities in the rate expression, including the Boltzmann factors, depend explicitly on the coordinate *R*. Since the PCET system is assumed to be in equilibrium along the coordinate *R*, the total rate constant (Eq. **27**) can be calculated by integrating Eq. **22** with a renormalized Boltzmann distribution function $P_{\mu}^{\mathrm{I}}\left(R\right)$ over all *R* distances:

$$k^{\mathrm{aver}}=\frac{1}{\hbar}\int_{0}^{\infty}dR\sum_{\mu}^{\{\mathrm{I}\}}P_{\mu}^{\mathrm{I}}\left(R\right)\sum_{\nu}^{\{\mathrm{II}\}}\left|V_{\mu\nu}^{\neq}\left(R\right)\right|^{2}\sqrt{\frac{\pi\beta}{\lambda_{\mu\nu}\left(R\right)}}\exp\left\{-\frac{\beta\left[\Delta G_{\mu\nu}^{0}\left(R\right)+\lambda_{\mu\nu}\left(R\right)\right]^{2}}{4\lambda_{\mu\nu}\left(R\right)}\right\}. \qquad \text{Eq. } \mathbf{27}$$

The above rate expression does not follow rigorously from the Golden Rule general expression. Nevertheless, it provides a physically reasonable method for estimating the rate constant in cases for which the dynamical coupling of the slow *R*-mode to the solvent fluctuations is negligible.

Quantization of a fast *R*-mode

Now we consider the case in which the *R*-mode is characterized by a high frequency Ω and a relatively low reduced mass M. In this case, the motion along the *R*-mode occurs on a much faster timescale than the characteristic timescale associated with the solvent fluctuations driving the PCET reaction, so the *R*-mode fluctuations are dynamically uncoupled from the solvent fluctuations. In contrast to the previous case of the slow dynamically uncoupled *R*-mode, however, the quantum character of this motion becomes important, especially at low temperatures where $\beta\hbar\Omega$ is much greater than 1. To include these quantum effects, the *R*-mode can be treated quantum mechanically on the same level as the electron and proton coordinates. The electrons, transferring proton, and *R*-mode are assumed to be adiabatic with respect to the solvent coordinates within the reactant and product states. Thus, the reaction can be described in terms of nonadiabatic transitions between two sets of intersecting free energy surfaces $\varepsilon_k^{\mathrm{I}}\left(z_p, z_e\right)$ and $\varepsilon_l^{\mathrm{II}}\left(z_p, z_e\right)$ corresponding to the reactant and product electron-proton-*R*-mode states. These electron-proton-*R*-mode vibronic states are eigenfunctions of $T_p + T_R + H_{\mathrm{el}}$, where H_{el} is represented by $\mathbf{H}^{\mathrm{I}}$ and $\mathbf{H}^{\mathrm{II}}$ for the reactant and product, respectively. The methodology for calculating these electron-proton-*R*-mode vibronic free energy surfaces in a manner that includes the electron-proton-*R*-mode nonadiabatic effects is analogous to that described in Ref. 17 for electron-proton vibronic states. The resulting nonadiabatic rate expression , shown in Eq. **28** , in the high-temperature limit of a Debye solvent is

$$k^{\text{quant}} = \frac{1}{\hbar}\sum_{k}^{\{\text{I}\}} P_k^{\text{I}} \sum_{l}^{\{\text{II}\}} \left|V_{kl}^{\neq}\right|^2 \sqrt{\frac{\pi\beta}{\lambda_{kl}}} \exp\left\{-\frac{\beta\left(\Delta G_{kl}^0 + \lambda_{kl}\right)^2}{4\lambda_{kl}}\right\}. \qquad \text{Eq. } \mathbf{28}$$

This expression formally resembles the expression in Eq. **22** except that the quantities do not depend explicitly on *R* but rather are calculated for pairs of mixed electron-proton-*R*-mode vibronic free energy surfaces, which are also assumed to be harmonic in z_p and z_e.

Dynamical effects of the *R*-mode

In this subsection, we present rate expressions that include the dynamical effects of both the *R*-mode and the solvent, as well as the quantum character of the *R*-mode. One of the most important effects of the *R*-coordinate motion in PCET systems is the modulation of the proton tunneling distance and thereby the nonadiabatic coupling between the reactant and product vibronic states. The fluctuations of the nonadiabatic coupling due to the *R*-motion can be dynamically coupled to the fluctuations of the solvent degrees of freedom, which are responsible for bringing the system into the degenerate state required for nonadiabatic transitions. Here we consider the case in which the electron and transferring proton are adiabatic with respect to the *R*-mode and solvent within the reactant and product states. Thus, the reactant and product electron-proton vibronic surfaces $\varepsilon_\mu^{\text{I}}(R,\xi)$ and $\varepsilon_\nu^{\text{II}}(R,\xi)$ are calculated. As mentioned above, the methodology for calculating these electron-proton vibronic free energy surfaces in a manner that includes the electron-proton nonadiabatic effects is described in Ref. 17.

To include the effects of the dynamical coupling between the *R*-mode and the solvent in our description, the *R*-mode is treated dynamically on the same level as the solvent modes. The effective channel Hamiltonians, displayed in Eq. **29** , for the reactant (J = I) and product (J = II) electron-proton vibronic states are:

$$H_\mu^J = T_R + T_\xi + \varepsilon_\mu^J(R,\xi). \qquad \text{Eq. } \mathbf{29}$$

The overall PCET rate is determined by nonadiabatic transitions between eigenstates of the effective channel Hamiltonians for all pairs of reactant and product electron-proton vibronic states. In this case, the Golden Rule nonadiabatic rate constant is expressed in Eq. **30**

$$k^{\mathrm{dyn}} = \sum_{\mu}^{\{\mathrm{I}\}} P_{\mu}^{\mathrm{I}} \sum_{\nu}^{\{\mathrm{II}\}} k_{\mu\nu}^{\mathrm{dyn}} , \qquad \text{Eq. } \mathbf{30}$$

where P_{μ}^{I} is the Boltzmann weighting for reactant electron-proton vibronic state Iμ, and the partial rate constant $k_{\mu\nu}^{\mathrm{dyn}}$ describes nonadiabatic transitions between the quantum states for the pair of electron-proton vibronic surfaces $\varepsilon_{\mu}^{\mathrm{I}}(R,\xi)$ and $\varepsilon_{\nu}^{\mathrm{II}}(R,\xi)$.

The partial rate constant (Eq. **31**) can be expressed as an integral of the time-dependent probability flux correlation function $j_{\mu\nu}(t)$ given in Eq. **32**.[29]

$$k_{\mu\nu}^{\mathrm{dyn}} = \frac{1}{\hbar^2} \int_{-\infty}^{\infty} j_{\mu\nu}(t)\, dt \qquad \text{Eq. } \mathbf{31}$$

$$j_{\mu\nu}(t) = \left\langle \hat{V}_{\mu\nu}(0) \exp_{(-)} \left[\frac{i}{\hbar} \int_{0}^{t} \Delta\hat{H}_{\mu\nu}(\tau)\, d\tau \right] \hat{V}_{\mu\nu}(t) \right\rangle_{\{\mathrm{I}\mu\}} . \qquad \text{Eq. } \mathbf{32}$$

Here $\left\langle (\cdots) \right\rangle_{\{\mathrm{I}\mu\}} = \mathrm{Tr}\left\{ \exp\left[-\beta H_{\mu}^{\mathrm{I}} \right] (\cdots) \right\} \Big/ \mathrm{Tr}\left\{ \exp\left[-\beta H_{\mu}^{\mathrm{I}} \right] \right\}$ designates a thermodynamic average over the reactant states (i.e., the eigenstates of the reactant Hamiltonian H_{μ}^{I}). In this expression, $\Delta\hat{H}_{\mu\nu}(\tau)$ and $\hat{V}_{\mu\nu}(t)$ are the Heisenberg operators describing the time evolution of the energy gap and the coupling between the reactant and product states governed by the reactant channel Hamiltonian H_{μ}^{I}, and $\exp_{(-)}[\cdots]$ is the negative time-ordered exponential.[47,48]

The nonadiabatic coupling $V_{\mu\nu}$ between reactant and product electron-proton vibronic states depends on the *R*-coordinate and the solvent coordinates. This coupling can be approximated as the product of a constant electronic coupling and a Franck-Condon overlap of the reactant and product electron-proton vibronic wavefunctions. In typical PCET systems with a well-separated electron donor and acceptor and a hydrogen-bonded PT interface, the overlap of the reactant and product proton vibrational wavefunctions depends only weakly on the solvent coordinates. As a result, the Condon approximation for the nonadiabatic coupling with respect to the solvent coordinates is typically valid.[18] In contrast, the overlap of the reactant and product proton vibrational wavefunctions depends very strongly on the proton donor-acceptor separation *R*. For a simple model based on two ground state harmonic oscillator wavefunctions with centers separated by *R*, the overlap increases exponentially with decreasing *R*. Expanding the coupling in a Taylor series to first order (Eq. **33**), we approximate the *R*-dependence of the overall coupling $V_{\mu\nu}$ by a single exponential:

$$V_{\mu\nu}(t) \approx V_{\mu\nu}^{(0)} \exp\left[-\alpha_{\mu\nu}\left(R(t)-\bar{R}^{\mathrm{I}\mu}\right)\right], \qquad \text{Eq. } \mathbf{33}$$

where $\bar{R}^{\mathrm{I}\mu}$ is the equilibrium value of the *R*-coordinate on the reactant surface $\varepsilon_{\mu}^{\mathrm{I}}\left(R, z_p, z_e\right)$, $V_{\mu\nu}^{(0)} = V_{\mu\nu}^{\neq}\left(\bar{R}^{\mathrm{I}\mu}\right)$ given in Eq. **26** , and the quantity $\alpha_{\mu\nu}$ can be calculated from the expression in Eq. **34**

$$\alpha_{\mu\nu} = -\frac{1}{2\left(V_{\mu\nu}^{(0)}\right)^2}\left.\frac{\partial\left(V_{\mu\nu}^2\right)}{\partial R}\right|_{R=\bar{R}^{\mathrm{I}\mu}}. \qquad \text{Eq. } \mathbf{34}$$

(Note that $\alpha_{\mu\nu}$ is calculated from the square of the coupling to avoid difficulties arising from the arbitrary sign of the coupling.) This approximation has been shown to be reasonable for model PCET systems and was also used previously for nonadiabatic proton transfer systems.[28,29,32]

Dynamical rate for molecular representation of the environment

When the solvent or protein environment is represented on a molecular level as a collection of modes with coordinates ξ, the dynamics of the Heisenberg operators for the energy gap (Eq. **35**) and the coupling (Eq. **36**) entering Eq. **32** can be described in terms of the time evolution of the *R*-coordinate $R(t)$ and the solvent coordinates $\xi(t)$ on the reactant electron-proton vibronic surface $\varepsilon_\mu^{\mathrm{I}}(R,\xi)$:

$$\Delta\hat{H}_{\mu\nu}(t) \to \Delta\varepsilon_{\mu\nu}\left(\hat{R}(t),\hat{\xi}(t)\right) \qquad \text{Eq. } \mathbf{35}$$

$$\hat{V}_{\mu\nu}(t) \to V_{\mu\nu}\left(\hat{R}(t),\hat{\xi}(t)\right) \qquad \text{Eq. } \mathbf{36}$$

where $\Delta\varepsilon_{\mu\nu}(R,\xi)$ and $V_{\mu\nu}(R,\xi)$, respectively, are given in Eq. **37** and Eq. **38**.

$$\Delta\varepsilon_{\mu\nu}(R,\xi) = \varepsilon_\nu^{\mathrm{II}}(R,\xi) - \varepsilon_\mu^{\mathrm{I}}(R,\xi) \qquad \text{Eq. } \mathbf{37}$$

$$V_{\mu\nu}(R,\xi) = \left\langle \Phi_\mu^{\mathrm{I}}\left(\mathbf{r}_e, r_p \mid R,\xi\right) \middle| T_p + H \middle| \Phi_\nu^{\mathrm{II}}\left(\mathbf{r}_e, r_p \mid R,\xi\right) \right\rangle \qquad \text{Eq. } \mathbf{38}$$

Here *H* is defined in the four-state VB basis by Eq. **21** . For the derivation of the rate expressions, the nonadiabatic coupling in Eq. **38** is approximated by the expression in Eq. **33** . The energy gap can be expanded in a Taylor series up to first order in *R* around the equilibrium value of the *R*-coordinate on the reactant surface (Eq. **39**):

$$\Delta\varepsilon_{\mu\nu}(R,\xi) = \Delta\varepsilon_{\mu\nu}(\bar{R}^{\mathrm{I}\mu},\xi) + D_{\mu\nu}(\xi)\delta R_\mu \qquad \text{Eq. } \mathbf{39}$$

where $D_{\mu\nu}(\xi)$, given in Eq. **40** ,

$$D_{\mu\nu}\left(\xi\right)=\left.\frac{\partial\Delta\varepsilon_{\mu\nu}}{\partial R}\right|_{R=\bar{R}^{1\mu}} \qquad \text{Eq. } \mathbf{40}$$

is the derivative of the energy gap with respect to the R-coordinate and $\delta R_{\mu}=R-\bar{R}^{1\mu}$.

Substituting Eq. **33** and Eq. **39** into Eq. **32** and using the cumulant expansion up to second order, we obtain the following expression (Eq. **41**) for the probability flux correlation function:

$$\begin{aligned} j_{\mu\nu}^{\mathrm{MD}}\left(t\right)=&\left|V_{\mu\nu}^{(0)}\right|^{2}\exp\left[-2\alpha_{\mu\nu}\left\langle\delta R_{\mu}\right\rangle\right]\exp\left[\frac{i}{\hbar}\left(\left\langle\mathcal{E}_{\mu\nu}\right\rangle+\left\langle\tilde{D}_{\mu\nu}\right\rangle\left\langle\delta R_{\mu}\right\rangle\right)t\right]\\ &\times\exp\left\{\alpha_{\mu\nu}^{2}\left[\left\langle\delta R^{2}\right\rangle+C_{R}\left(t\right)\right]-\frac{2i\alpha_{\mu\nu}}{\hbar}\left\langle\tilde{D}_{\mu\nu}\right\rangle\int_{0}^{t}C_{R}\left(\tau\right)d\tau\right.\\ &\left.-\frac{1}{\hbar^{2}}\int_{0}^{t}d\tau_{1}\int_{0}^{\tau_{1}}d\tau_{2}C_{\mathcal{E}}\left(\tau_{1}-\tau_{2}\right)-\frac{1}{\hbar^{2}}\int_{0}^{t}d\tau_{1}\int_{0}^{\tau_{1}}d\tau_{2}C_{D}\left(\tau_{1}-\tau_{2}\right)C_{R}\left(\tau_{1}-\tau_{2}\right)\right\} \end{aligned} \qquad \text{Eq. } \mathbf{41}$$

where the time evolution on the reactant vibronic surface is described in terms of the variables defined in Eq. **42** , Eq. **43** , Eq. **44** and Eq. **45**

$$\mathcal{E}_{\mu\nu}\left(t\right)=\Delta\varepsilon_{\mu\nu}\left(\bar{R}^{1\mu},\xi\left(t\right)\right) \qquad \text{Eq. } \mathbf{42}$$

$$\delta\mathcal{E}_{\mu\nu}\left(t\right)=\mathcal{E}_{\mu\nu}\left(t\right)-\left\langle\mathcal{E}_{\mu\nu}\right\rangle \qquad \text{Eq. } \mathbf{43}$$

$$\delta R_{\mu}\left(t\right)=R\left(t\right)-\bar{R}^{1\mu} \qquad \text{Eq. } \mathbf{44}$$

$$\delta R\left(t\right)=R\left(t\right)-\left\langle R\right\rangle=\delta R_{\mu}\left(t\right)-\left\langle\delta R_{\mu}\right\rangle, \qquad \text{Eq. } \mathbf{45}$$

and the time correlation functions are defined in Eq. **46** , Eq. **47** and Eq. **48**

$$C_{\mathcal{E}}(t) = \left\langle \delta\mathcal{E}_{\mu\nu}(0)\,\delta\mathcal{E}_{\mu\nu}(t) \right\rangle \qquad \text{Eq. } \mathbf{46}$$

$$C_{R}(t) = \left\langle \delta R(0)\,\delta R(t) \right\rangle \qquad \text{Eq. } \mathbf{47}$$

$$C_{D}(t) = \left\langle \tilde{D}_{\mu\nu}(0)\,\tilde{D}_{\mu\nu}(t) \right\rangle \qquad \text{Eq. } \mathbf{48}$$

with $\tilde{D}_{\mu\nu}(t) = D_{\mu\nu}\left(\xi(t)\right)$. Note that the probability flux expression in Eq. **41** is analogous to the probability flux expression given in Ref. 30 for vibrationally nonadiabatic PT reactions occurring on a single adiabatic electronic state. In PCET reactions, however, the energy gap and coupling are defined for pairs of electron-proton vibronic surfaces corresponding to different electronic states.

The above quantities can be evaluated with molecular dynamics simulations of the full solute-solvent system on the reactant vibronic surface $\varepsilon_{\mu}^{\mathrm{I}}(R,\xi)$. Specifically, the quantities $C_R(t)$, $\left\langle \delta R^2 \right\rangle$, and $\left\langle \delta R_{\mu} \right\rangle$ can be calculated from a molecular dynamics simulation with an unconstrained *R*-coordinate, and the quantities $\left\langle \mathcal{E}_{\mu\nu} \right\rangle$, $\left\langle \tilde{D}_{\mu\nu} \right\rangle$, $C_{\mathcal{E}}(t)$, and $C_D(t)$ can be calculated from a molecular dynamics simulations of the full solute-solvent system with the *R*-coordinate fixed to $R = \overline{R}^{\mathrm{I}\mu}$ (i.e., on the constrained reactant vibronic surface $\varepsilon_{\mu}^{I}(R = \overline{R}^{\mathrm{I}\mu},\xi)$). Subsequently, the time integral of the probability flux correlation function given in Eq. **32** can be calculated numerically.

Alternatively, the time correlation function $C_R(t)$ can be calculated with methodology based on the dephasing theory of molecular vibrations in liquids.[30] This methodology involves the calculation of a frequency shift correlation function, which can be obtained from a simulation of the system with the *R*-coordinate fixed to $R = \overline{R}^{\mathrm{I}\mu}$, and the correlation function for an undamped quantum mechanical harmonic oscillator. This

approach includes the quantum character of the *R*-mode. Typically the solvent dephasing effects on the *R*-mode occur on a much longer time scale than the decay of the probability flux correlation function, and the solvent dephasing effects on the *R*-mode can be neglected. In this case, the correlation functions involving the *R*-coordinate can be calculated directly from the analytical expressions for an undamped quantum mechanical harmonic oscillator.

The probability flux expression in Eq. **41** can be simplified under the following well-defined conditions: the coupling between the *R*-coordinate and the solvent coordinates is neglected, the surfaces are approximated to be harmonic along the *R*-coordinate, and the *R*-mode frequency is assumed to be the same for both the reactant and product surfaces. In this case, the surfaces can be expanded in a Taylor series up to second order in *R* and are expressed in Eq. **49**

$$\begin{aligned} \varepsilon_{\mu}^{I}(R,\xi) &= \varepsilon_{\mu}^{I}(\bar{R}^{\mathrm{I}\mu},\xi) + \frac{1}{2}M\Omega^{2}\delta R_{\mu}^{2} \\ \varepsilon_{\nu}^{II}(R,\xi) &= \varepsilon_{\nu}^{II}(\bar{R}^{\mathrm{I}\mu},\xi) - \frac{1}{2}M\Omega^{2}\Delta R_{\mu\nu}^{2} + \frac{1}{2}M\Omega^{2}\delta R_{\nu}^{2} \end{aligned}, \qquad \text{Eq. } \mathbf{49}$$

where $\delta R_{\nu} = R - \bar{R}^{\mathrm{II}\nu}$, $\Delta R_{\mu\nu} = \bar{R}^{\mathrm{II}\nu} - \bar{R}^{\mathrm{I}\mu}$, and the *R*-mode frequency Ω is defined in Eq. **50**

$$\Omega^{2} = \frac{1}{M}\left.\frac{\partial^{2}\varepsilon_{\mu}^{\mathrm{I}}(R,\xi)}{\partial R^{2}}\right|_{R=\bar{R}^{\mathrm{I}\mu}}. \qquad \text{Eq. } \mathbf{50}$$

In general, the *R*-mode frequency depends on the solvent coordinates, but this dependence is removed when the coupling between the *R*-coordinate and the solvent coordinates is neglected. Note that the neglect of this coupling is physically reasonable for PCET reactions, in which the dominant solute-solvent interactions arise from the changes in charge distribution due to the ET rather than the PT reaction. Given this expansion of the surfaces, the energy gap derivative defined in Eq. **40** becomes the constant $\tilde{D}_{\mu\nu} = \tilde{\Lambda}_{\mu\nu} \equiv -M\Omega^{2}\Delta R_{\mu\nu}$. In this limit, $\left\langle \tilde{D}_{\mu\nu} \right\rangle = \tilde{\Lambda}_{\mu\nu}$, $C_{D}(t) = \left\langle \tilde{\Lambda}_{\mu\nu}^{2} \right\rangle = \tilde{\Lambda}_{\mu\nu}^{2}$, and

$\left\langle \delta R_\mu \right\rangle = \left\langle \delta R \right\rangle = 0$ because $\bar{R}^{\mathrm{I}\mu} = \left\langle R \right\rangle$ for harmonic surfaces. As a result, Eq. **41** simplifies to Eq. **51**

$$j_{\mu\nu}^{\mathrm{MD,harm}}(t) = \left|V_{\mu\nu}^{(0)}\right|^2 \exp\left[\frac{i}{\hbar}\left\langle \mathcal{E}_{\mu\nu}\right\rangle t\right] \times \exp\left\{\alpha_{\mu\nu}^2\left[\left\langle \delta R^2\right\rangle + C_R(t)\right] - \frac{2i\alpha_{\mu\nu}\tilde{\Lambda}_{\mu\nu}}{\hbar}\int_0^t C_R(\tau)\,d\tau - \frac{1}{\hbar^2}\int_0^t d\tau_1\int_0^{\tau_1} d\tau_2 C_\varepsilon(\tau_1-\tau_2) - \frac{\tilde{\Lambda}_{\mu\nu}^2}{\hbar^2}\int_0^t d\tau_1\int_0^{\tau_1} d\tau_2 C_R(\tau_1-\tau_2)\right\} \quad \text{Eq. 51}$$

As mentioned above, the quantities $\left\langle \mathcal{E}_{\mu\nu}\right\rangle$ and $C_\varepsilon(t)$ can be evaluated with molecular dynamics simulations of the full solute-solvent system on the constrained reactant vibronic surface $\varepsilon_\mu^I(R=\bar{R}^{\mathrm{I}\mu},\xi)$. Since the dephasing effects of the solvent on the *R*-mode are neglected in this limit, the quantities pertaining to the *R*-coordinate can be calculated from analytical expressions for an undamped quantum mechanical harmonic oscillator with frequency Ω and reduced mass *M*. Thus, all of the quantities required for the calculation of the nonadiabatic flux in Eq. **51** can be calculated from a single molecular dynamics simulation on the constrained reactant vibronic surface.

Dynamical rate for continuum representation of the environment

When the solvent or protein environment is represented as a dielectric continuum, the dynamics of the Heisenberg operators for the energy gap and the coupling can be described in terms of the time evolution of the *R*-coordinate $R(t)$ and the two scalar solvent variables $z_p(t)$ and $z_e(t)$ on the adiabatic free energy surface $\varepsilon_\mu^{\mathrm{I}}\left(R,z_p,z_e\right)$. Expansion of the free energy surfaces $\varepsilon_\mu^{\mathrm{I}}\left(R,z_p,z_e\right)$ and $\varepsilon_\nu^{\mathrm{II}}\left(R,z_p,z_e\right)$ in Taylor series up to second order around the minima and use of the second order cumulant expansion[49] of Eq. **32** leads to the following expression (Eq. **52**) for the probability flux correlation function in terms of time correlation functions:

$$j^{\text{cont}}(t) = \left|V_{\mu\nu}^{(0)}\right|^2 \exp\left[\frac{i}{\hbar}\left(\Delta G^0 + \lambda_z + \lambda_R\right)t\right]$$
$$\times \exp\left\{\frac{2M\lambda_\alpha}{\hbar^2}\left[C_R(0) + C_R(t)\right] - \frac{4i}{\hbar^2}M\Omega\sqrt{\lambda_\alpha\lambda_R}\int_0^t C_R(\tau)\,d\tau\right.$$
$$\left. - \frac{1}{\hbar^2}\int_0^t d\tau_1 \int_0^{\tau_1} d\tau_2\, C_Z(\tau_1 - \tau_2) - \frac{2M\Omega^2\lambda_R}{\hbar^2}\int_0^t d\tau_1 \int_0^{\tau_1} d\tau_2\, C_R(\tau_1 - \tau_2)\right\} . \qquad \text{Eq. } \mathbf{52}$$

Although the indices μ and ν are omitted in Eq. **52** for simplicity, the quantities in this expression are defined in terms of a pair of reactant and product free energy surfaces $\varepsilon_\mu^{\mathrm{I}}\left(R, z_p, z_e\right)$ and $\varepsilon_\nu^{\mathrm{II}}\left(R, z_p, z_e\right)$. The time correlation function for the *R*-mode is defined in Eq. **47**. The time correlation function for the solvent variables is $C_Z(t) \equiv \left\langle \delta Z(0)\delta Z(t)\right\rangle$. In the continuum solvent representation, the solvent variables are defined in Eq. **53** , Eq. **54**, Eq. **55** and Eq. **56**

$$\delta Z(t) = \tilde{\Lambda}_p\left(z_p(t) - \bar{z}_p^{\mathrm{I}\mu}\right) + \tilde{\Lambda}_e\left(z_e(t) - \bar{z}_e^{\mathrm{I}\mu}\right) \qquad \text{Eq. } \mathbf{53}$$

$$\tilde{\Lambda}_p = \Lambda_{z_p z_p}\left(\bar{z}_p^{\mathrm{I}\mu} - \bar{z}_p^{\mathrm{II}\nu}\right) + \Lambda_{z_p z_e}\left(\bar{z}_e^{\mathrm{I}\mu} - \bar{z}_e^{\mathrm{II}\nu}\right) + \Lambda_{z_p R}\left(\bar{R}^{\mathrm{I}\mu} - \bar{R}^{\mathrm{II}\nu}\right) \qquad \text{Eq. } \mathbf{54}$$

$$\tilde{\Lambda}_e = \Lambda_{z_p z_e}\left(\bar{z}_p^{\mathrm{I}\mu} - \bar{z}_p^{\mathrm{II}\nu}\right) + \Lambda_{z_e z_e}\left(\bar{z}_e^{\mathrm{I}\mu} - \bar{z}_e^{\mathrm{II}\nu}\right) + \Lambda_{z_e R}\left(\bar{R}^{\mathrm{I}\mu} - \bar{R}^{\mathrm{II}\nu}\right) \qquad \text{Eq. } \mathbf{55}$$

$$\Lambda_{xy} = \left.\frac{\partial^2 \varepsilon_\mu^{\mathrm{I}}\left(R, z_p, z_e\right)}{\partial x \partial y}\right|_{\bar{z}_p^{\mathrm{I}\mu}, \bar{z}_e^{\mathrm{I}\mu}, \bar{R}^{\mathrm{I}\mu}} . \qquad \text{Eq. } \mathbf{56}$$

In Eq. **52** , ΔG^0 is the reaction free energy defined, in Eq. **57** , as the difference in the equilibrium free energies for the reactant and product surfaces:

$$\Delta G^0_{\mu\nu} = \varepsilon^{\mathrm{II}}_{\nu}\left(\bar{R}^{\mathrm{II}\nu}, \bar{z}_p^{\mathrm{II}\nu}, \bar{z}_e^{\mathrm{II}\nu}\right) - \varepsilon^{\mathrm{I}}_{\mu}\left(\bar{R}^{\mathrm{I}\mu}, \bar{z}_p^{\mathrm{I}\mu}, \bar{z}_e^{\mathrm{I}\mu}\right). \qquad \text{Eq. } \mathbf{57}$$

The *R*-mode reduced mass M and frequency Ω are related to the reactant surface $\varepsilon^{\mathrm{I}}_{\mu}\left(R, z_p, z_e\right)$ through the second derivative at the minimum as shown in Eq. **58** .

$$M\Omega^2 = \left.\frac{\partial^2 \varepsilon^{\mathrm{I}}_{\mu}\left(R, z_p, z_e\right)}{\partial R^2}\right|_{\bar{R}^{\mathrm{I}\mu}, \bar{z}_p^{\mathrm{I}\mu}, \bar{z}_e^{\mathrm{I}\mu}} \qquad \text{Eq. } \mathbf{58}$$

λ_z and λ_R are the solvent and *R*-mode reorganization energies, respectively, and are defined in Eq. **59** and Eq. **60**

$$\lambda_z = \varepsilon^{\mathrm{I}}_{\mu}\left(\bar{R}^{\mathrm{I}\mu}, \bar{z}_p^{\mathrm{II}\nu}, \bar{z}_e^{\mathrm{II}\nu}\right) - \varepsilon^{\mathrm{I}}_{\mu}\left(\bar{R}^{\mathrm{I}\mu}, \bar{z}_p^{\mathrm{I}\mu}, \bar{z}_e^{\mathrm{I}\mu}\right) \qquad \text{Eq. } \mathbf{59}$$

$$\lambda_R = \varepsilon^{\mathrm{I}}_{\mu}\left(\bar{R}^{\mathrm{II}\nu}, \bar{z}_p^{\mathrm{I}\mu}, \bar{z}_e^{\mathrm{I}\mu}\right) - \varepsilon^{\mathrm{I}}_{\mu}\left(\bar{R}^{\mathrm{I}\mu}, \bar{z}_p^{\mathrm{I}\mu}, \bar{z}_e^{\mathrm{I}\mu}\right) \approx \frac{1}{2} M\Omega^2 \Delta R^2 \qquad \text{Eq. } \mathbf{60}$$

where $\Delta R = \bar{R}^{\mathrm{II}\nu} - \bar{R}^{\mathrm{I}\mu}$ is the difference between the equilibrium *R*-coordinates on the reactant and product surfaces. Finally, the quantum coupling term λ_α, given in Eq. **61**, is defined for each pair of reactant and product states as

$$\lambda_\alpha = \frac{\hbar^2 \alpha^2_{\mu\nu}}{2M}. \qquad \text{Eq. } \mathbf{61}$$

The form of Eq. **52** is the same as the form of Eq. **51** , which was derived for a molecular representation of the environment in conjunction with the assumptions of negligible coupling between the *R*-mode and the solvent modes, a harmonic potential along the *R*-coordinate, and the same *R*-mode frequency for the reactant and product surfaces. Previously, expressions similar to Eq. **52** were derived and analyzed by Borgis, Lee, and Hynes in the context of vibrationally nonadiabatic proton transfer reactions in solution.[29-31] Note that the time correlation function for the solvent variables is fundamentally different for PCET reactions because PCET reactions involve two

correlated solvent coordinates z_p and z_e rather than a single solvent coordinate z_p. Moreover, the physical meaning of the quantum coupling term λ_α is fundamentally different for PCET reactions because the coupling for PCET reactions involves ET nonadiabatic coupling as well as PT coupling. The most interesting features of the expression in Eq. **52** are the terms in the exponential that are proportional to the quantum coupling term λ_α and to $\sqrt{\lambda_\alpha \lambda_R}$. These terms reflect the dynamical correlations between the *R*-mode and the nonadiabatic coupling fluctuations.

When the coherent quantum nonadiabatic transitions described by the first exponential term in Eq. **52** are sufficiently damped by the solvent and *R*-mode fluctuations, the magnitude of the oscillations of the probability flux correlation function decreases on a time scale shorter than the time scale of the solvent dephasing effects on the *R*-motion. For this short time scale, we can ignore the solvent dephasing effects on the harmonic *R*-motion and use the standard analytical expression for the time correlation function of an undamped quantum mechanical harmonic oscillator (Eq. **62**) for $C_R(t)$:[50]

$$C_R(t) = \frac{\hbar}{2M\Omega}\left[\coth\left(\tfrac{1}{2}\beta\hbar\Omega\right)\cos\Omega t + i\sin\Omega t\right]. \qquad \text{Eq. } \mathbf{62}$$

In a number of well-defined limits, the rate expression can be simplified to closed analytical expressions. In the short-time high-temperature approximation for a Debye solvent,[51] the third term in the second exponential of Eq. **52** becomes Eq. **63** .

$$\exp\left[-\frac{1}{\hbar^2}\int_0^t d\tau_1 \int_0^{\tau_1} d\tau_2\, C_Z(\tau_1 - \tau_2)\right] = \exp\left[-\frac{\lambda_z t^2}{\beta\hbar^2}\right]. \qquad \text{Eq. } \mathbf{63}$$

In this limit, the solvent dynamics is negligible on the time-scale of the probability flux correlation function. These approximations were tested previously by molecular dynamics simulations on model PT systems and were shown to be valid for typical proton transfer reactions in polar solvents.[29-31] Since the solvent reorganization energies associated with the ET component of the PCET process are typically much larger than those associated with PT reactions, the time scale for the damping of the probability flux correlation function is expected to be even shorter for PCET than for PT.

Substitution of Eq. **62** and Eq. **63** into Eq. **52** leads to the following closed analytical expression (Eq. **64**) for the nonadiabatic partial rate $k_{\mu\nu}^{\mathrm{dyn}}$:

$$k_{\mu\nu}^{\mathrm{dyn}} = \frac{\left|V_{\mu\nu}^{(0)}\right|^2}{\hbar^2\Omega}\exp\left[\frac{2\lambda_\alpha\zeta}{\hbar\Omega}\right]\int_{-\infty}^{\infty} d\tau \exp\left[-\frac{1}{2}\chi\tau^2 + p\left(\cos\tau - 1\right) + i\left(q\sin\tau + \theta\tau\right)\right] \qquad \text{Eq. } \mathbf{64}$$

where the dimensionless parameters are defined in Eq. **65**.

$$\zeta = \coth\left(\tfrac{1}{2}\beta\hbar\Omega\right);\quad \chi = \frac{2\lambda_z}{\beta\hbar^2\Omega^2};\quad \theta = \frac{\Delta G^0 + \lambda_z}{\hbar\Omega}$$
$$p = \zeta\frac{\lambda_R + \lambda_\alpha}{\hbar\Omega} - 2\frac{\sqrt{\lambda_R\lambda_\alpha}}{\hbar\Omega};\quad q = \frac{\lambda_R + \lambda_\alpha}{\hbar\Omega} - 2\zeta\frac{\sqrt{\lambda_R\lambda_\alpha}}{\hbar\Omega} \qquad \text{Eq. } \mathbf{65}$$

Again the indices μ and ν are omitted for simplicity. Note that the imaginary part of the rate in Eq. **64** is identically zero. The PT analog of this expression is given in Refs. 29-31.

The real part of the integrand in Eq. **64** is a damped oscillating function of the frequency-scaled time ($\tau = \Omega t$). The strength of the damping factor $\exp\left[-\chi\tau^2/2\right]$ depends on the temperature, the solvent reorganization energy λ_z, and the *R*-mode quantum energy $\hbar\Omega$. Note that in the regime considered here, the solvent fluctuations are the key element responsible for damping the quantum coherent electron-proton tunneling. In the absence of the solvent reorganization (i.e., $\lambda_z = 0$), the time integral in Eq. **64** is divergent and the reaction rate constant is not defined. Ref. 32 provides an alternative approach that avoids these divergences by performing a transformation of a model Hamiltonian corresponding to proton transfer. Since the thermal average of the transformed perturbation is zero, the integral of the time correlation function is convergent for the entire range of system parameters.

In certain limiting regimes, the time integral in Eq. **64** can be simplified to obtain closed analytical rate expressions.[29,31] In the high temperature (low frequency) limit for the *R*-mode ($\beta\hbar\Omega$ is much less than 1) we obtain the following asymptotic expression, given in Eq. **66** , for the partial rate:

$$k_{\mu\nu}^{\text{high-T}} = \frac{\left|V_{\mu\nu}^{(0)}\right|^2}{\hbar}\exp\left[\frac{4\lambda_\alpha}{\beta\hbar^2\Omega^2}\right]\sqrt{\frac{\pi\beta}{\lambda_{\text{tot}}\left(1-\frac{4\lambda_\alpha\lambda_R}{\lambda_{\text{tot}}^2}\right)}} \times\exp\left[-\frac{\beta\left(\Delta G_{\mu\nu}^0+\lambda_z-\frac{4}{\beta\hbar\Omega}\sqrt{\lambda_\alpha\lambda_R}\right)^2}{4\lambda_{\text{tot}}}\left(2-\frac{\lambda_z}{\lambda_{\text{tot}}}\right)\right], \quad \text{Eq. 66}$$

where $\lambda_{\text{tot}} = \lambda_z + \lambda_R + \lambda_\alpha$. This expression closely resembles the analogous expression in Eq. **22** for fixed *R* with a few important distinctions. First, it has an additional temperature-dependent exponential prefactor $\exp\left[4\lambda_\alpha/\left(\beta\hbar^2\Omega^2\right)\right]$, which results in non-Arrhenius behavior of the rate constant at high temperatures. Second, the conventional Marcus activation barrier $\left(\Delta G_{\mu\nu}^0+\lambda_z\right)^2/\left(4\lambda_z\right)$ is modified due to the presence of the cross term $4\sqrt{\lambda_\alpha\lambda_R}/\left(\beta\hbar\Omega\right)$, which is a quantum effect that is related to the dynamical correlation between the *R*-mode and the nonadiabatic coupling fluctuations. Note that if $\lambda_\alpha = \lambda_R = 0$ (i.e., the coupling is independent of *R* and the equilibrium value of *R* is the same for reactant and product free energy surfaces), this expression is identical to the previously derived rate expression for PCET reactions with fixed *R*, as evident by a comparison to Eq. **22** .

In the low temperature (high frequency) limit for the *R*-mode in the strong solvation regime (i.e., $\left|\Delta G_{\mu\nu}^0\right| < \lambda_z$), we obtain the following asymptotic expression, given in Eq. **67** , for the partial rate:

$$k_{\mu\nu}^{\text{low-T}} = \frac{\left|V_{\mu\nu}^{(0)}\right|^2}{\hbar}\exp\left[\frac{2\lambda_\alpha}{\hbar\Omega}\right]\exp\left[-\frac{\left(\sqrt{\lambda_\alpha}-\sqrt{\lambda_R}\right)^2}{\hbar\Omega}\right]\sqrt{\frac{\pi\beta}{\lambda_z}}\exp\left[-\frac{\beta\left(\Delta G^0+\lambda_z\right)^2}{4\lambda_z}\right], \quad \text{Eq. 67}$$

which is similar to the previously derived PCET rate expressions except for the additional exponential prefactors that modify the nonadiabatic coupling. In this quantum limit for

the *R*-mode, the rate expression corresponds qualitatively to the expression in Eq. **28** for the case of a fast quantized *R*-mode. The square of the coupling in conjunction with the two additional exponential prefactors in Eq. **67** can be interpreted in terms of the square of the coupling between the reactant and product *R*-mode vibrational ground states.[29] Transitions involving *R*-mode vibrationally excited states are not significant at low temperatures. Note that typical PCET reactions are expected to be in the strong solvation regime, in which the solvent reorganization energy exceeds the absolute reaction free energy. The rate expression can also be derived for the weak solvation regime, following the procedure in Ref. 31. Moreover, the rigorous derivation of the low-temperature rate expressions for proton transfer reactions given in Ref. 32 could also be applied to PCET reactions.

Model Calculations

Model system

To illustrate the various features of the nonadiabatic rate expressions presented in the previous section, we have performed calculations for a model PCET system. Our model PCET system is based on a linear, five-site model (Eq. **68**):

$$D_e - D_p - H - A_p - A_e \qquad \text{Eq. } \mathbf{68}$$

where D and A represent donor and acceptor, respectively, and the subscripts e and p represent electron and proton, respectively. The gas phase electronic Hamiltonian $\mathbf{h}_0\left(r_p, R\right)$ in the basis of the four VB states is described by a [4×4] matrix with the matrix elements represented by an analytical expression consisting of a modified LEPS potential for the PT interface[27] and a harmonic potential for the *R*-mode. The detailed expressions for the diagonal and off-diagonal matrix elements of the gas-phase electronic

Hamiltonian matrix $\mathbf{h}_0\left(r_p, R\right)$ are given in the Appendix B. For the calculation of the solvent reorganization energy matrix elements, we implemented a simple ellipsoidal electrostatic continuum model[52] used in our previous work.[21] In this ellipsoidal model, point charges on the five sites defined in Eq. **68** are placed on the major axis of the ellipsoidal cavity. These point charges are chosen to represent the solute charge distribution for each VB state. The cavity is immersed in a dielectric continuum solvent characterized by the inertial (ε_0) and optical (ε_∞) dielectric constants, respectively. The basic set of parameters for our model PCET system is given in Table **2**. In the calculations described below, we vary reduced mass *M*, and frequency Ω of the *R*-mode, as well as ΔR, while keeping all other parameters fixed.

Table **2**: Parameters for the model PCET system.

Hybrid LEPS potential		Ellipsoidal model					
D_{AH}, kcal/mol	80.0	ε_0					78.4
D_{BH}, kcal/mol	80.0	ε_∞					1.78
$R^0_{\mathrm{D_pH}}$, Å	1.0	Major axis, Å					8.0
$R^0_{\mathrm{A_pH}}$, Å	1.0	Minor axis, Å					5.0
R^0_1, Å	2.8		D_e	D_p	H	A_p	A_e
R^0_2, Å	2.9	1a state charges	-1.0	0.5	0.5	0.0	0.0
$k_{\mathrm{D_pH}}$	0.5	1b state charges	-1.0	0.0	0.5	0.5	0.0
$k_{\mathrm{A_pH}}$	0.5	2a state charges	0.0	0.5	0.5	0.0	-1.0
σ	0.5	2b state charges	0.0	0.0	0.5	0.5	-1.0
V^{ET}, kcal/mol	0.01						
V^{PT}, kcal/mol	50.0						
$\Omega_{\mathrm{D_pH}}$, cm^{-1}	2900						
$\Omega_{\mathrm{A_pH}}$, cm^{-1}	2900						
$\Delta E_{1\mathrm{b}}$, kcal/mol	20.0						
$\Delta E_{2\mathrm{a}}$, kcal/mol	20.0						
$\Delta E_{2\mathrm{b}}$, kcal/mol	0.0						

The nonadiabatic rate calculations were performed using Eq. **27** for k^{aver}, Eq. **28** for k^{quant}, and Eq. **64** for k^{dyn}. For simplicity, only the ground state electron-proton vibronic states for reactants and products were taken into account. In the calculation of k^{quant}, twenty vibrational states for the *R*-mode were used for both reactants and products. The dynamical rate constant was calculated by numerically evaluating the time integral in Eq. **64** . The values for Ω, ΔG^0, λ_z, λ_R, and α required for the calculation of the dynamical rate constant k^{dyn} were extracted from the reactant and product three-dimensional electron-proton vibronic free energy surfaces $\varepsilon_0^{\text{I}}\left(R, z_p, z_e\right)$ and $\varepsilon_0^{\text{II}}\left(R, z_p, z_e\right)$. Specifically, the *R*-mode harmonic frequency Ω was obtained from the second derivative along the *R*-coordinate evaluated numerically at the reactant minimum. The reaction free energy ΔG^0 was calculated as the difference of free energies at the minima of the reactant and product surfaces. The coupling parameter α was estimated from the derivative of the square of the coupling with respect to *R* calculated at the crossing point along a straight line connecting the reactant and product minima. The reorganization energies λ_z, λ_R, and λ_α were calculated using Eq. **59**, Eq. **60** and Eq. **61**, respectively. Table **3** provides the calculated values of these quantities for the model systems used in the calculations described below.

Table **3**: Intrinsic quantities calculated for a series of model PCET potentials with different *R*-mode reduced masses M and frequencies Ω.

Model code	P10-100	P10-300	P10-400	P10-600	P100-600
M, g/mol	10	10	10	10	100
$\Omega_{D_pA_p}$, cm^{-1}	100	300	400	600	600
Ω, cm^{-1}	169.5	287.7	376.4	564.6	558.9
$\hbar\Omega$, kcal/mol	0.48	0.82	1.08	1.61	1.60
ΔG^0, kcal/mol	0.19	0.36	0.38	0.36	0.47
λ_z, kcal/mol	12.27	12.09	12.15	12.07	12.07
ΔR, Å	0.10	0.10	0.10	0.10	0.10
λ_R, kcal/mol	0.01	0.41	0.47	1.41	10.72
α, $Å^{-1}$	8.62	10.31	10.38	10.70	13.04
λ_α, kcal/mol	0.36	0.51	0.52	0.55	0.08
$\sqrt{\lambda_R\lambda_\alpha}$, kcal/mol	0.06	0.46	0.49	0.88	0.94

Results and analysis

The temperature dependences of the nonadiabatic PCET rate constants calculated for the model systems specified in Table **3** are presented in Figure **15** and Figure **16**. Model systems P10-100, P10-300, P10-400, and P10-600 have a reduced mass of M = 10 g/mol and frequencies of approximately 100, 300, 400, and 600 cm^{-1}, respectively. Model system P100-600 has a reduced mass of M = 100 g/mol and a frequency of approximately 600 cm^{-1}. Figure **15** illustrates the effects of changing the *R*-mode frequency and reduced mass. Figure **16** illustrates the effects of changing the *R*-mode reorganization energy from $\lambda_R = 0$ to $\lambda_R = 0.47$ kcal/mol for model system P10-400.

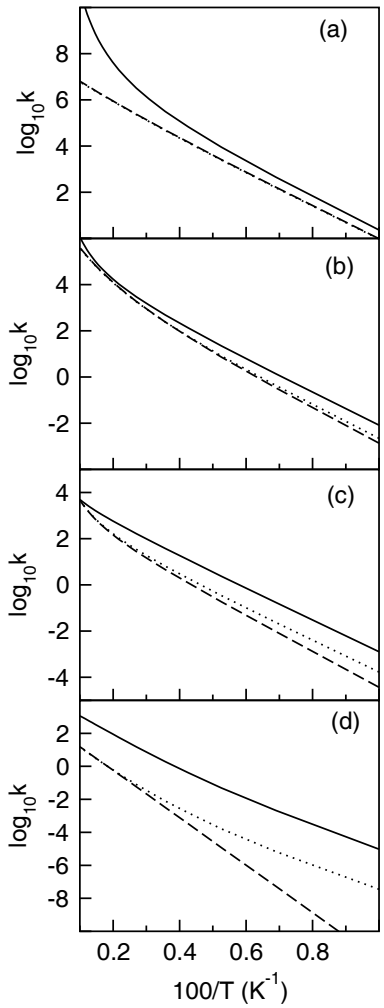

Figure **15**: Temperature dependence of the thermally averaged rate constant k^{aver} (dashed lines), the rate constant k^{quant} with a quantized *R*-mode (dotted lines), and the dynamical rate constant k^{dyn} (solid lines) for four PCET models with parameters given in Table **2** and Table **3** : (a) Model P10-100, (b) Model P10-300, (c) Model P10-600, and (d) Model P100-600.

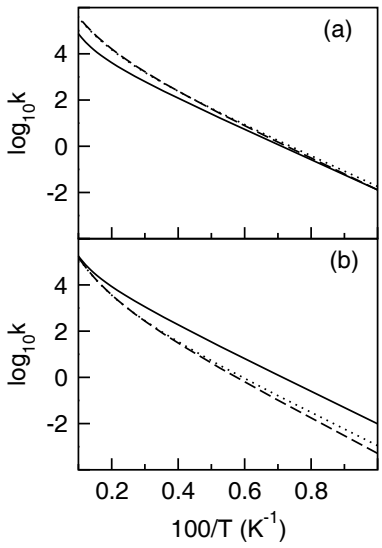

Figure **16**: Temperature dependence of the thermally averaged rate constant k^{aver} (dashed lines), the rate constant k^{quant} with a quantized *R*-mode (dotted lines), and the dynamical rate constant k^{dyn} (solid lines) for the P10-400 model with parameters given in Table **2** and Table **3** in the absence and presence of *R*-mode reorganization energy: (a) $\Delta R = 0$ and $\lambda_R = 0$ and (b) $\Delta R = 0.1$ Å and $\lambda_R = 0.47$ kcal/mol.

For all model systems studied, the rate k^{quant} with a quantized *R*-mode approaches the thermally averaged rate k^{aver} at high temperatures or low frequencies (i.e., for $\beta\hbar\Omega$ much less than 1). At low temperatures or high frequencies (i.e., for $\beta\hbar\Omega$ much greater than 1), k^{quant} exceeds k^{aver} due to the delocalized character of the ground state *R*-mode vibrational wavefunction. When the classical *R*-motion is frozen at low temperatures, the shorter *R*-distances are still accessible to the quantized *R*-mode, and the rate k^{quant} is enhanced relative to k^{aver} due to the larger effective nonadiabatic coupling at shorter *R*-distances. Note that at ambient temperatures of ~300 K for typical *R*-mode frequencies of 100-500 cm^{-1}, the quantum and thermally averaged approaches give similar results.

The relation of the thermally averaged and quantum rate constants to the dynamical rate constant is more complex. The dependence of the nonadiabatic coupling on the *R*-coordinate is effectively taken into account in the first two non-dynamical

approaches. Averaging of the rate constant over the *R*-coordinate in the thermally averaged approach and quantization of the *R*-mode in the quantum approach lead to effective sampling of the nonadiabatic couplings. However, the effects of *dynamical* coupling between fluctuations of the *R*-coordinate and the nonadiabatic coupling are neglected in these non-dynamical approaches. This dynamical coupling is a quantum effect that is expected to be more pronounced for systems with a high-frequency *R*-mode. Figure **15c** indicates that the dynamical rate constants k^{dyn} for systems with a high frequency *R*-mode deviate significantly from the thermally averaged rate constant k^{aver} and the quantum rate constant k^{quant} even at high temperatures. Note that the slope of the plot of $\log_{10} k^{\mathrm{quant}}$ vs. $1/T$ at lower temperatures is similar to the corresponding slope for the dynamical rate constant k^{dyn}, whereas the corresponding slope for the thermodynamically averaged rate constant k^{aver} is significantly different. This observation indicates that at lower temperatures, the quantization of the fast *R*-mode includes some of the important quantum effects influencing the effective activation energy of the nonadiabatic PCET process.

The key quantities reflecting the dynamical effects of the *R*-coordinate motion are the *R*-mode reorganization energy λ_R and the quantum coupling term λ_α defined in Eq. **60** and Eq. **61** , respectively. At high temperatures, the additional exponential factor $\exp\left[4\lambda_\alpha/\left(\beta\hbar^2\Omega^2\right)\right]$ in Eq. **66** strongly affects the temperature dependence and may result in significantly non-Arrhenius behavior of the rate. This non-Arrhenius behavior increases as the dependence of the coupling on the *R*-coordinate increases (i.e., as α increases). It also increases as the frequency and reduced mass of the *R*-mode decrease. This phenomenon is illustrated in Figure **15a** for a system with $\alpha = 8.62$ Å^{-1} in conjunction with an *R*-mode frequency of Ω = 170 cm^{-1} and a reduced mass of M = 10. Note that this non-Arrhenius behavior vanishes for constant coupling (i.e., $\alpha = 0$).

Another important aspect of the effects of the *R*-motion on the nonadiabatic PCET rates is the *R*-mode reorganization energy λ_R. For PCET reactions with symmetric or nearly symmetric interfaces, λ_R is zero or very small. In this case, the effects of the

dynamical correlation between the *R*-mode and the nonadiabatic coupling arise from only the quantum coupling term λ_α in Eq. **64** and hence are relatively small. This trend is illustrated in Figure **16**. For the symmetric model system with zero shift of the equilibrium *R*-distance from the reactants to products (i.e., $\Delta R = 0$), the *R*-mode reorganization energy λ_R is zero. In this case, we observe similar behavior of the rate constants for all three approaches, especially at lower temperatures, as shown in Figure **16a**. In contrast, Figure **16b** illustrates that the rate constants calculated with the three approaches differ considerably when $\Delta R = 0.1\,\text{Å}$, corresponding to $\lambda_R \approx 0.5$ kcal/mol, for the otherwise identical model system. In both cases, the temperature dependence of the rate constant k^{quant} for the quantized *R*-mode is similar to the temperature dependence of the dynamical rate constant k^{dyn}.

Conclusions

We have developed a theoretical formulation for PCET reactions to include the effects of the proton donor-acceptor vibrational motion. In this formulation, the solute is represented by a multistate valence bond model, and the active electrons and transferring proton(s) are treated quantum mechanically. We have presented nonadiabatic PCET rate expressions for the limits of a slow classical and a fast quantum donor-acceptor mode. We have also derived nonadiabatic PCET rate expressions that include the dynamical fluctuations of the nonadiabatic coupling, as well as the energy gap between the reactant and product states. This approach accounts for dynamical correlations between the fluctuations of the proton donor-acceptor distance and the nonadiabatic PCET coupling. The donor-acceptor mode can be treated classically or quantum mechanically within this dynamical description. For a continuum representation of the environment, the quantities in the dynamical rate expressions can be determined from the gas phase potential energy surface of the solute and an electrostatic dielectric continuum model. For a molecular representation of the environment, the quantitites in the dynamical rate expressions can

be calculated with classical molecular dynamics simulations of the full system in the reactant state. The main advantages of this theoretical formulation of PCET over previous formulations is the inclusion of the quantum mechanical and dynamical character of the proton donor-acceptor mode. We have illustrated the importance of these effects with applications to a series of model PCET systems.

Although our dynamical treatment of the proton donor-acceptor mode is analogous to the previous treatment of vibrationally nonadiabatic PT reactions, a number of important new issues arise for PCET reactions. In general, PCET reactions are described by at least a four-state model representing the four charge transfer states rather than the two-state model used for single PT reactions. As a result, general PCET reactions are described in terms of at least two scalar solvent coordinates corresponding to ET and PT rather than the single scalar solvent coordinate used for single PT reactions. The use of two scalar solvent coordinates leads to fundamentally different solvent terms in the rate expressions based on a dielectric continuum representation of the solvent. In addition, the previous work on vibrationally nonadiabatic PT reactions assumed that the reaction was *electronically* adiabatic (i.e., the reaction occurred on the electronic ground state). In contrast, typically PCET reactions are electronically nonadiabatic and occur on two different electronic surfaces corresponding to the two diabatic ET states. As a result, the nature of the nonadiabatic coupling is different for PCET reactions than for single PT reactions. The coupling for PCET may be viewed as a combination of the ET nonadiabatic coupling and the overlap of the reactant and product proton vibrational wavefunctions, whereas the coupling for single PT does not involve an ET coupling term.

The rate expressions presented in this paper provide the foundation for a variety of new directions. Future work will focus on the calculation of PCET rates with molecular dynamics simulations. These studies will elucidate the importance of the quantum and dynamical effects of the proton donor-acceptor mode, as well as the dynamical effects of the solvent, for PCET reactions.

References

(1) Blow, D. M. *Accounts of Chemical Research* **1976**, *9*, 145.

(2) Ramaswamy, S.; Eklund, H.; Plapp, B. V. *Biochemistry* **1994**, *33*, 5230.

(3) Ren, X. L.; Tu, C. K.; Laipis, P. J.; Silverman, D. N. *Biochemistry* **1995**, *34*, 8492.

(4) Knapp, M. J.; Rickert, K. W.; Klinman, J. P. *Journal of the American Chemical Society* **2002**, *124*, 3865.

(5) Kirmaier, C.; Holten, D. In *The Photosynthetic Bacterial reaction Center - Structure and Dynamics*; Breton, J., Vermeglio, A., Eds.; Plenum: New York, 1988.

(6) Binstead, R. A.; Meyer, T. J. *Journal of the American Chemical Society* **1987**, *109*, 3287.

(7) Kirby, J. P.; Roberts, J. A.; Nocera, D. G. *Journal of the American Chemical Society* **1997**, *119*, 9230.

(8) Farrer, B. T.; Thorp, H. H. *Inorganic Chemistry* **1999**, *38*, 2497.

(9) Huynh, M. H. V.; Meyer, T. J.; White, P. S. *Journal of the American Chemical Society* **1999**, *121*, 4530.

(10) Roth, J. P.; Lovell, S.; Mayer, J. M. *Journal of the American Chemical Society* **2000**, *122*, 5486.

(11) Nocera, D. G.; Chang, C. J.; Yeh, C. Y.; Deng, Y. Q. *Journal of Inorganic Biochemistry* **2001**, *86*, 81.

(12) Chang, C. J.; Chang, M. C. Y.; Damrauer, N. H.; Nocera, D. G. *Biochimica et Biophysica Acta* **2004**, *1655*, 13.

(13) Cukier, R. I. *Journal of Physical Chemistry* **1994**, *98*, 2377.

(14) Cukier, R. I. *Journal of Physical Chemistry* **1996**, *100*, 15428.

(15) Cukier, R. I.; Nocera, D. G. *Annual Review of Physical Chemistry* **1998**, *49*, 337.

(16) Cukier, R. I. *Biochimica et Biophysica Acta* **2004**, *1655*, 37.

(17) Soudackov, A.; Hammes-Schiffer, S. *Journal of Chemical Physics* **1999**, *111*, 4672.

(18) Soudackov, A.; Hammes-Schiffer, S. *Journal of Chemical Physics* **2000**, *113*, 2385.

(19) Hammes-Schiffer, S. *Accounts of Chemical Research* **2001**, *34*, 273.

(20) Hammes-Schiffer, S.; Iordanova, N. *Biochimica et Biophysical Acta* **2004**, *1655*, 29.

(21) Soudackov, A.; Hammes-Schiffer, S. *Journal of the American Chemical Society* **1999**, *121*, 10598.

(22) Iordanova, N.; Decornez, H.; Hammes-Schiffer, S. *Journal of the American Chemical Society* **2001**, *123*, 3723.

(23) Rostov, I.; Hammes-Schiffer, S. *Journal of Chemical Physics* **2001**, *115*, 285.

(24) Iordanova, N.; Hammes-Schiffer, S. *Journal of the American Chemical Society* **2002**, *124*, 4848.
(25) Carra, C.; Iordanova, N.; Hammes-Schiffer, S. *Journal of Physical Chemistry B* **2002**, *106*, 8415.
(26) Carra, C.; Iordanova, N.; Hammes-Schiffer, S. *Journal of the American Chemical Society* **2003**, *125*, 10429.
(27) Hatcher, E.; Soudackov, A. V.; Hammes-Schiffer, S. *Journal of the American Chemical Society* **2004**, *126*, 5763.
(28) Trakhtenberg, L. I.; Klochikhim, V. L.; Pshezhetsky, S. Y. *Chemical Physics* **1982**, *69*, 121.
(29) Borgis, D. C.; Lee, S. Y.; Hynes, J. T. *Chemical Physics Letters* **1989**, *162*, 19.
(30) Borgis, D.; Hynes, J. T. *Journal of Chemical Physics* **1991**, *94*, 3619.
(31) Borgis, D.; Hynes, J. T. *Chemical Physics* **1993**, *170*, 315.
(32) Suarez, A.; Silbey, R. *Journal of Chemical Physics* **1991**, *94*, 4809.
(33) Basilevsky, M. V.; Vener, M. V.; Davidovich, G. V.; Soudackov, A. V. *Chemical Physics* **1996**, *208*, 267.
(34) Kuznetsov, A. M.; Ulstrup, J. *Canadian Journal of Chemistry* **1999**, *77*, 1085.
(35) Kestner, N. R.; Logan, J.; Jortner, J. *Journal of Physical Chemistry* **1974**, *78*, 2148.
(36) Ulstrup, J.; Jortner, J. *Journal of Chemical Physics* **1975**, *63*, 4358.
(37) Bixon, M.; Jortner, J. *Advances in Chemical Physics* **1999**, *106*, 35.
(38) Kim, H. J.; Hynes, J. T. *Journal of Chemical Physics* **1992**, *96*, 5088.
(39) Kobrak, M. N.; Hammes-Schiffer, S. *Journal of Physical Chemistry B* **2001**, *105*, 10435.
(40) Marcus, R. *Journal of Chemical Physics* **1956**, *24*, 966.
(41) Marcus, R. *Journal of Chemical Physics* **1956**, *24*, 979.
(42) Levich, V. G.; Dogonadze, R. R. *Doklady Akademii Nauk SSSR* **1959**, *124*, 123.
(43) Levich, V. G. *Advances in Electrochemistry and Electrochemical Engineering* **1966**, *4*, 249.
(44) Ulstrup, J. *Charge Transfer Processes in Condensed Media*; Springer: Berlin, 1979.
(45) Newton, M. D.; Sutin, N. *Annual Reviews of Physical Chemistry* **1984**, *35*, 437.
(46) Barbara, P. F.; Meyer, T. J.; Ratner, M. A. *Journal of Physical Chemistry* **1996**, *100*, 13148.
(47) Goldberger, M. L.; Adams II, E. N. *Journal of Chemical Physics* **1952**, *20*, 240.
(48) Lax, M. *Journal of Chemical Physics* **1952**, *20*, 1752.
(49) Kubo, R. *Journal of Physical Society of Japan* **1962**, *17*, 1100.
(50) Chandler, D. Theory of quantum processes in liquids. In *Liquids Freezing and Glass Transition*; D. Levesque, J. P. H. a. J. Z.-J., Ed.; Elsevier Science Publishers, B.V. (North Holland), 1991; Vol. 51; pp 193.

(51) Zusman, L. D. *Chemical Physics* **1980**, *49*, 295.
(52) Westheimer, F. H.; Kirkwood, J. G. *Journal of Chemical Physics* **1938**, *6*, 513.

Chapter 4

Comparison of Dynamical Aspects of Nonadiabatic Electron, Proton, and Proton-Coupled Electron Transfer Reactions

Reproduced in part with permission from E. Hatcher, A. Soudackov, S. Hammes-Schiffer, *Chemical Physics*, **2005**, 319, 93-100.

Introduction

Proton-coupled electron transfer (PCET) reactions involve the simultaneous transfer of an electron and a proton. These types of reactions play an important role in a wide range of chemical and biological processes.[1-17] A variety of theoretical approaches have been developed and applied to PCET reactions in solution and proteins.[18-34] PCET reactions are typically nonadiabatic due to the relatively large separation between the electron donor and acceptor and small overlap between the localized proton vibrational wavefunctions of the reactant and product vibronic states. While the dynamical aspects of single electron transfer (ET) and single proton transfer (PT) reactions have been studied extensively,[35-44] the dynamical aspects of PCET reactions have been neglected in most previous theoretical treatments.

In general, nonadiabatic ET, PT, and PCET reactions can be described in terms of nonadiabatic transitions between reactant and product quantum states. Despite the similarities among nonadiabatic ET, PT, and PCET reactions, each type of reaction has unique features that deserve careful consideration. Solvent reorganization plays an important role in all three types of reactions, but the magnitude of the solvent reorganization energy and the relevant time scales of the solvent dynamics vary. An important feature of PT and PCET reactions is the role of the proton donor-acceptor vibrational motion, which strongly impacts the nonadiabatic couplings and thereby the

rates. Understanding the similarities and differences among these types of reactions will aid in the elucidation of the underlying physical principles of charge transfer reactions in condensed phases.

In this paper, we analyze the dynamical behavior of a model PCET system in solution and compare the results to previous analyses of the dynamical aspects of nonadiabatic ET and PT reactions.[37,39] Our analysis is based on a general dynamical rate expression for nonadiabatic PCET reactions.[27] The overall rate is expressed in terms of a time-dependent probability flux correlation function. The effects of the proton donor-acceptor and solvent dynamics on this probability flux correlation function are analyzed with molecular dynamics simulations. In addition, the approximations invoked for previously derived analytical rate expressions are tested.

The paper is organized as follows. Section II summarizes the theoretical formulation for PCET reactions and describes the model system. Section III presents the application of the dynamical theory to this model system and provides a detailed analysis of the dynamical aspects of PCET reactions, as well as a comparison to single ET and PT reactions. The conclusions and future directions are given in Section IV.

Methodology

Theoretical formulation

PCET systems may be defined in terms of the proton coordinate r_p, the proton donor-acceptor coordinate R, and the solvent coordinates ξ. In our theoretical formulation for nonadiabatic PCET reactions,[23,24] the active electrons and transferring proton are treated quantum mechanically. The PCET reaction is described in terms of nonadiabatic transitions between pairs of reactant and product electron-proton vibronic states. The reactant and product vibronic surfaces $\varepsilon_\mu^{\mathrm{I}}(R,\xi)$ and $\varepsilon_\nu^{\mathrm{II}}(R,\xi)$, respectively,

are obtained by calculating the proton vibrational states for the reactant and product ET electronic states.

In our previous work,[23,24] the electronic structure of the solute was described in the framework of a four-state valence bond (VB) model.[45] The most basic PCET reaction involving the transfer of one electron and one proton may be described in terms of the following four diabatic electronic basis states given in Eq. **69**.

$$\begin{aligned}
&(1a)\quad \mathrm{D_e^-}\cdots\cdots\mathrm{D_pH^+}\cdots\cdots\mathrm{A_p}\cdots\cdots\mathrm{A_e}\\
&(1b)\quad \mathrm{D_e^-}\cdots\cdots\mathrm{D_p}\cdots\cdots{}^{+}\mathrm{HA_p}\cdots\cdots\mathrm{A_e}\\
&(2a)\quad \mathrm{D_e}\cdots\cdots\mathrm{D_pH^+}\cdots\cdots\mathrm{A_p}\cdots\cdots\mathrm{A_e^-}\\
&(2b)\quad \mathrm{D_e}\cdots\cdots\mathrm{D_p}\cdots\cdots{}^{+}\mathrm{HA_p}\cdots\cdots\mathrm{A_e^-}
\end{aligned} \qquad \text{Eq. } \mathbf{69}$$

where 1 and 2 denote the ET state, and *a* and *b* denote the PT state. Typically for PCET reactions the intermediate states 1*b* and 2*a* are much higher in energy than states 1*a* and 2*b* due to differences in the electrostatic interactions. Thus, the reactant ET state is predominantly 1*a*, and the product ET state is predominantly 2*b*.

The coupling $V_{\mu\nu}$ between the reactant vibronic states Iμ and product vibronic state IIν is defined in Eq. **70**

$$V_{\mu\nu} = \left\langle \phi_\mu^{\mathrm{I}} \middle| V\left(r_{\mathrm{p}}, \xi^{\dagger}\right) \middle| \phi_\nu^{\mathrm{II}} \right\rangle_{\mathrm{p}} \qquad \text{Eq. } \mathbf{70}$$

where the subscript of the angular brackets indicates integration over r_{p}, $\xi^{\dagger}$ represents the solvent coordinates in the region of strong nonadiabatic coupling between the reactant and product surfaces, $V\left(r_p, \xi\right)$ is the electronic coupling between reactant and product states, and ϕ_μ^{I} and ϕ_ν^{II} are the proton vibrational wavefunctions for the reactant and product vibronic states, respectively. Here I and II, respectively, denote reactant and product ET states. For many PCET systems,[46,47] the coupling is approximately proportional to the overlap between the reactant and product proton vibrational wavefunctions as shown in Eq. **71** :

$$V_{\mu\nu} \approx V^{\mathrm{el}} \left\langle \phi_{\mu}^{\mathrm{I}} \,|\, \phi_{\nu}^{\mathrm{II}} \right\rangle_{\mathrm{p}}, \qquad \text{Eq. } \mathbf{71}$$

where V^{el} is a constant effective electronic coupling.

Recently, we derived nonadiabatic rate expressions for PCET that include the dynamical effects of both the proton donor-acceptor mode (i.e., the *R* coordinate) and the solvent.[27] One of the most important effects of the *R* coordinate motion in PCET systems is the modulation of the proton tunneling distance and thereby the nonadiabatic coupling between the reactant and product vibronic states. The fluctuations of the nonadiabatic coupling due to the *R* motion can be dynamically coupled to the fluctuations of the solvent degrees of freedom, which are responsible for bringing the system into the degenerate state required for nonadiabatic transitions. Here we consider the case in which the electron and transferring proton are adiabatic with respect to the *R* coordinate and the solvent within the reactant and product states. The *R* mode is treated dynamically on the same level as the solvent modes in order to include the effects of the dynamical coupling between the *R* mode and the solvent.

The nonadiabatic dynamical rate constant k^{dyn} is expressed in Eq. **72**.

$$k^{\mathrm{dyn}} = \sum_{\mu}^{\{\mathrm{I}\}} P_{\mu}^{\mathrm{I}} \sum_{\nu}^{\{\mathrm{II}\}} k_{\mu\nu}^{\mathrm{dyn}}, \qquad \text{Eq. } \mathbf{72}$$

where the partial rate constant $k_{\mu\nu}^{\mathrm{dyn}}$, given in Eq. **73** , describes nonadiabatic transitions between the quantum states for the pair of electron-proton vibronic surfaces Iμ and IIν and can be written as an integral of the time-dependent probability flux correlation function $j_{\mu\nu}(t)$.

$$k_{\mu\nu}^{\mathrm{dyn}} = \frac{1}{\hbar^2} \int_{-\infty}^{\infty} j_{\mu\nu}(t)\, dt \qquad \text{Eq. } \mathbf{73}$$

We have used this formulation to derive rate expressions for both a dielectric continuum and a molecular representation of the environment.[27] Here we focus on only the molecular representation of the environment.

To facilitate the derivation of an analytical expression for the probability flux correlation function, the *R* dependence of the overall coupling $V_{\mu\nu}$ is approximated by a single exponential in Eq. **74**

$$V_{\mu\nu} \approx V_{\mu\nu}^{(0)} \exp\left[-\alpha_{\mu\nu}\left(R-\bar{R}^{\mathrm{I}\mu}\right)\right], \qquad \text{Eq. } \mathbf{74}$$

where $\bar{R}^{\mathrm{I}\mu}$ is the equilibrium value of the *R* coordinate on the reactant surface Iμ, $V_{\mu\nu}^{(0)}$ is the value of the coupling at $R=\bar{R}^{\mathrm{I}\mu}$, and $\alpha_{\mu\nu}$ can be estimated from the *R* dependence of the coupling. The justification for Eq. **74** is that the nonadiabatic coupling can be approximated as the product of a constant electronic coupling and the overlap of the reactant and product proton vibrational wavefunctions, as given in Eq. **71** (See Appendix C). For PCET reactions, typically this overlap depends only weakly on the solvent coordinates but depends very strongly on the proton donor-acceptor separation *R*. For a simple model based on two ground state harmonic oscillator wavefunctions with centers separated by *R*, the overlap increases exponentially with decreasing *R*. The approximation in Eq. **74** has been shown to be reasonable for model PCET systems and was also used previously for nonadiabatic proton transfer systems.[36,48,49]

Using a second-order cumulant expansion, the probability flux correlation function, shown in Eq. **75** , can be expressed as

$$\begin{aligned} j_{\mu\nu}^{\mathrm{MD}}(t) = & \left|V_{\mu\nu}^{(0)}\right|^2 \exp\left[\frac{i}{\hbar}\left\langle \mathcal{E}_{\mu\nu}\right\rangle t\right] \\ & \times\exp\left\{\alpha_{\mu\nu}^2\left[C_R(0)+C_R(t)\right]-\frac{2i\alpha_{\mu\nu}}{\hbar}\left\langle \tilde{D}_{\mu\nu}\right\rangle\int_0^t C_R(\tau)\,d\tau\right. \\ & \left.-\frac{1}{\hbar^2}\int_0^t d\tau_1\int_0^{\tau_1} d\tau_2 C_{\mathcal{E}}(\tau_1-\tau_2)-\frac{1}{\hbar^2}\int_0^t d\tau_1\int_0^{\tau_1} d\tau_2 C_D(\tau_1-\tau_2)C_R(\tau_1-\tau_2)\right\} \end{aligned}, \qquad \text{Eq. } \mathbf{75}$$

where the time evolution on the reactant vibronic surface is described in terms of the energy gap (Eq. **76**)

$$\mathcal{E}_{\mu\nu}(t) = \Delta\varepsilon_{\mu\nu}\left(\bar{R}^{\mathrm{I}\mu},\xi(t)\right) = \varepsilon_{\nu}^{\mathrm{II}}\left(\bar{R}^{\mathrm{I}\mu},\xi\right)-\varepsilon_{\mu}^{\mathrm{I}}\left(\bar{R}^{\mathrm{I}\mu},\xi\right), \qquad \text{Eq. } \mathbf{76}$$

the derivative of the energy gap (Eq. **77**)

$$\tilde{D}_{\mu\nu}\left(\xi(t)\right)=\left.\frac{\partial\Delta\varepsilon_{\mu\nu}}{\partial R}\right|_{R=\bar{R}^{1\mu}}, \qquad \text{Eq. } \mathbf{77}$$

and the R mode. The time correlation function for the energy gap is defined as $C_{\varepsilon}(t)=\left\langle\delta\mathcal{E}_{\mu\nu}(0)\delta\mathcal{E}_{\mu\nu}(t)\right\rangle$, where $\delta\mathcal{E}_{\mu\nu}(t)=\mathcal{E}_{\mu\nu}(t)-\left\langle\mathcal{E}_{\mu\nu}\right\rangle$. The time correlation functions for the other variables are defined analogously. These expressions are analogous to those derived previously for vibrationally nonadiabatic PT reactions occurring on a single adiabatic electronic surface.[38,39]

The quantities in Eq. **75** can be evaluated with molecular dynamics simulations of the full solute-solvent system on the reactant vibronic surface $\varepsilon_{\mu}^{\mathrm{I}}(R,\xi)$. Specifically, the quantity $C_R(t)$ can be calculated from a molecular dynamics simulation with an unconstrained R coordinate, and the quantities $\left\langle\mathcal{E}_{\mu\nu}\right\rangle$, $\left\langle\tilde{D}_{\mu\nu}\right\rangle$, $C_{\varepsilon}(t)$, and $C_D(t)$ are calculated from a molecular dynamics simulation of the full solute-solvent system with the R coordinate constrained to $R=\bar{R}^{1\mu}$. In the derivation of this expression, we assume that $\bar{R}^{1\mu}=\left\langle R\right\rangle$. The quantum effects of the R coordinate may be included using the standard analytical expression for the time correlation function of an undamped quantum mechanical harmonic oscillator.[50]

The transferring hydrogen may be represented as a classical nucleus bound to the proton donor at a fixed distance during the molecular dynamics simulation on the reactant surface. For the calculation of the energy gap, the proton is moved to the proton acceptor to obtain the product state energy. This approximation neglects the effects of delocalization of the hydrogen nuclear wavefunction on the motion of the other nuclei. We emphasize that the quantum behavior of the transferring hydrogen is included in the rate calculation through the couplings between the vibronic states, which depend on the overlap between the reactant and product proton vibrational wavefunctions.

Model system

The model system used for the simulations discussed in this paper is depicted in Figure **17**. The D_e–A_e distance is constrainted to be 7.54 Å, and the D_p–H distance is constrained to be 1.1 Å. Harmonic bond restraints with force constants of 232 kcal/mol/Å^2 and equilibrium values of 2.37 Å are applied to D_e–D_p and A_e–A_p. To maintain approximate linearity, harmonic restraints with force constants of 100.0 kcal/mol/deg^2 and equilibrium values of 180˚ are applied to the $D_eD_pA_e$ angle, the $D_eA_pA_e$ angle, and the D_pHA_p angle. The masses of the electron donor and acceptor are 55.8470 g/mol (i.e., the atomic mass of iron), and the masses of the proton donor and acceptor are 14.0067 g/mol (i.e., the atomic mass of nitrogen).

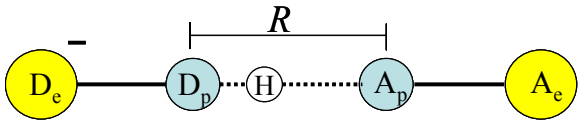

Figure **17**: Schematic picture of the solute for the model PCET system.

The solute is solvated with 253 explicit water molecules in a periodic cubic box with sides of length 19.98 Å. The water molecules are represented with the TIP3P flexible model.[51,52] The solvent-solute interactions include both electrostatic and van der Waals interactions. In the reactant, the electron donor has a charge of –0.5 *e* and the electron acceptor has a charge of +0.5 *e*, and in the product these charges are reversed. In the reactant, the proton donor has a charge of 0.0 and the proton acceptor has a charge of –0.41 *e*, and in the product these charges are reversed. The proton always has a charge of +0.41 *e*. Thus, the overall solute is neutral. The Ewald method is used to treat the electrostatic interactions.[53] The van der Waals pair parameters for the interactions of D_e and A_e with the oxygen atoms of the water molecules are ε=0.153 kcal/mol and σ=3.5 Å. The van der Waals pair parameters for the interactions of D_p and A_p with the oxygen atoms of the water molecules are ε=0.15595 kcal/mol and σ=3.14155 Å. The classical equations of motion are integrated with the Verlet algorithm[54] with a time step of 0.5 fs.

The solute constraints are applied with the SHAKE algorithm.[55] A canonical ensemble with a temperature of 300 K is maintained with a Nosè-Hoover thermostat.[56] The system is equilibrated for 70 ps, and the data is collected for 200 ps. All of the simulations were performed with a modified version of DL_POLY_2.14.[57] In the calculations of the probability flux, $\alpha = 10$ Å^{-1}.

Results

The time correlation functions $C_{\varepsilon}(t)$ and $C_R(t)$ for the energy gap and R coordinate, respectively, are depicted in Figure **18**. The corresponding spectral densities are depicted in Figure **19**. The spectral density $J(\omega)$ is defined in terms of the cosine transform of the time correlation function $C(t)$, as given in Eq. **78** ,

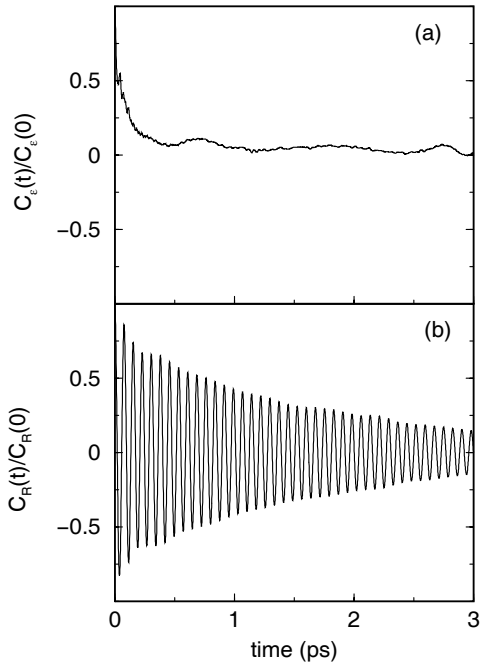

Figure **18**: Normalized time correlation function $C(t)/C(0)$ for (a) the energy gap fluctuations $\delta\mathcal{E}$ and (b) the R coordinate fluctuations δR .

$$C(t) = \frac{8}{\pi\beta}\int_0^\infty \frac{J(\omega)}{\omega}\cos(\omega t)d\omega \qquad \text{Eq. } \mathbf{78}$$

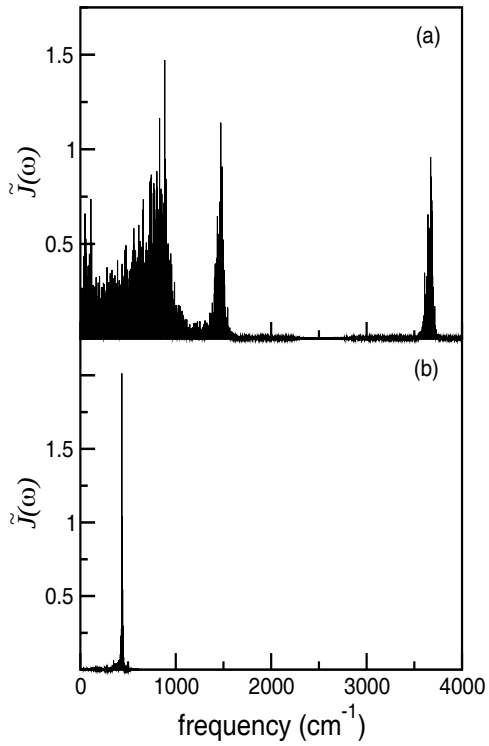

Figure **19**: Normalized spectral density $\tilde{J}(\omega)$ defined in Eq. **79** for (a) the energy gap fluctuations $\delta\mathcal{E}$ and (b) the *R* coordinate fluctuations δR .

and the normalized spectral density (Eq. **79**) is defined as[37]

$$\tilde{J}(\omega) = J(\omega)\Big/\int_0^\infty \frac{J(\omega)}{\omega}d\omega\,, \qquad \text{Eq. } \mathbf{79}$$

where $\beta = 1/k_B T$. The decay of the energy gap correlation function is characterized by two distinct relaxation times. The initial fast decay on the time scale of ~40 fs can be attributed to the relatively high frequency librational modes of water, and the slower exponential tail with a relaxation time of ~0.5 ps is attributable to the low frequency rotational and translational modes of the solvent. In the spectral density of the solvent, the stretching motions of water are evident at ~3600 cm^{-1}, the bending motions of water are evident at ~1500 cm^{-1}, and the librational, rotational, and translational solvent motions correspond to the broad band at lower frequencies. The *R* coordinate correlation function decays on a slower time scale of ~3 ps. The sharp peak in the spectral density of the *R* coordinate indicates that the frequency of this mode is ~400 cm^{-1}. For this model, $\langle R \rangle = 2.85$ Å and $\langle \delta R^2 \rangle = 0.005$ $Å^2$. If the *R* mode were harmonic and uncoupled to the solvent, $C_R(t)$ would oscillate indefinitely with fixed amplitude, and the spectral density would be a delta function centered at the corresponding frequency. The observed decay of $C_R(t)$ and the broadening of the peak in the spectral density of the *R* mode are due to damping effects from the solvent-solute interactions.

If the potential energy of the system is assumed to be harmonic along the *R* coordinate, the energy gap derivative defined in Eq. **77** becomes the constant given in Eq. **80**.

$$\tilde{D}_{\mu\nu} = \tilde{\Lambda}_{\mu\nu} \equiv -M\Omega^2 \Delta R_{\mu\nu}, \qquad \text{Eq. } \mathbf{80}$$

where $\Delta R = \bar{R}^{\mathrm{II}\nu} - \bar{R}^{\mathrm{I}\mu}$ is the difference between the equilibrium *R* coordinates on the product and reactant surfaces and the *R* mode frequency Ω is given by Eq. **81** .

$$M\Omega^2 = \left. \frac{\partial^2 \varepsilon_\mu^{\mathrm{I}}(R,\xi)}{\partial R^2} \right|_{R=\bar{R}^{\mathrm{I}\mu}} \qquad \text{Eq. } \mathbf{81}$$

In this limit, the energy gap derivative is independent of time, so $\langle \tilde{D}_{\mu\nu} \rangle = \tilde{\Lambda}_{\mu\nu}$ and $C_D(t) = \tilde{\Lambda}_{\mu\nu}^2$. For a symmetric system, $\tilde{\Lambda}_{\mu\nu} = 0$. For this model system, $\langle \tilde{D}_{\mu\nu} \rangle$ = 3.67

kcal/mol/Å. The two terms in Eq. **75** that include this factor are negligible relative to the other terms due to the relatively small magnitude of $\left\langle \tilde{D}_{\mu\nu} \right\rangle$.

Figure **20** depicts the time dependence of the flux and the dominant contributing factors. The highly oscillatory term $\exp\left[\frac{i}{\hbar}\left\langle \mathcal{E}_{\mu\nu} \right\rangle t\right]$ shown in Figure **20b** has a period of ~0.005 ps and describes the coherent oscillations of the quantum amplitudes between the reactant and product vibronic states. For a symmetric system, the average energy gap $\left\langle \mathcal{E}_{\mu\nu} \right\rangle$ = 72.25 kcal/mol corresponds to the solvent reorganization energy. The period of the coherent term increases as the solvent reorganization energy decreases. The quantum coherent term is damped by other terms in Eq. **75** , thereby enabling the calculation of a reaction rate.

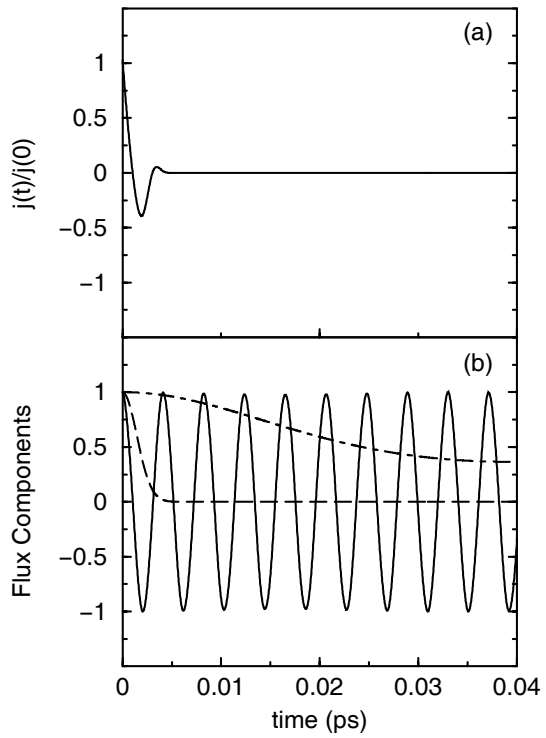

Figure **20**: (a) Normalized probability flux time correlation function $j(t)/j(0)$ defined in Eq. **75**. (b) Time dependence of normalized terms in Eq. **75**: coherent term $\exp\left[\frac{i}{\hbar}\langle\mathcal{E}_{\mu\nu}\rangle t\right]$ with solid line, R coordinate term $\exp\left\{\alpha_{\mu\nu}^2\left[C_R(0)+C_R(t)\right]\right\}$ with dot-dashed line, and solvent damping term $\exp\left\{-\frac{1}{\hbar^2}\int_0^t d\tau_1\int_0^{\tau_1} d\tau_2 C_\varepsilon(\tau_1-\tau_2)\right\}$ with dashed line. Each term is normalized by the value at $t = 0$.

The R coordinate term $\exp\left\{\alpha_{\mu\nu}^2\left[C_R(0)+C_R(t)\right]\right\}$ shown in Fig. **18b** oscillates with a period of ~0.08 ps and approaches the constant value $\exp\left\{\alpha_{\mu\nu}^2 C_R(0)\right\}$ at long times. A comparison of Figure **18b** and Figure **20a** indicates that the damping of the R mode by the solvent occurs on a longer time scale than the decay of the probability flux. If the R coordinate motion is assumed to be harmonic, and the solvent damping effects on this harmonic motion are neglected, then the standard analytical expression for the time

correlation function of an undamped quantum mechanical harmonic oscillator as given in Eq. **82** can be used for $C_R(t)$:[50]

$$C_R(t) = \frac{\hbar}{2M\Omega}\left[\coth\left(\tfrac{1}{2}\beta\hbar\Omega\right)\cos\Omega t + i\sin\Omega t\right]. \qquad \text{Eq. } \mathbf{82}$$

The classical (high temperature) limit of this expression is Eq. **83**

$$C_R(t) = \frac{1}{\beta M\Omega^2}\cos\Omega t\,. \qquad \text{Eq. } \mathbf{83}$$

Figure **21a** compares the *R* coordinate term with $C_R(t)$ calculated from the simulations to this term with $C_R(t)$ calculated from the expressions in Eqs. **82** and **83**. The agreement between the calculated *R* coordinate term and the classical harmonic oscillator results indicates that solvent damping effects are not important on the time scale of the probability flux. The classical and quantum harmonic oscillator results are both fairly constant for the relevant time scale, suggesting that the quantum effects of the *R* coordinate do not impact the dynamical behavior of the probability flux. On the other hand, inclusion of the quantum effects of the *R* coordinate increases the magnitude of the rates slightly.

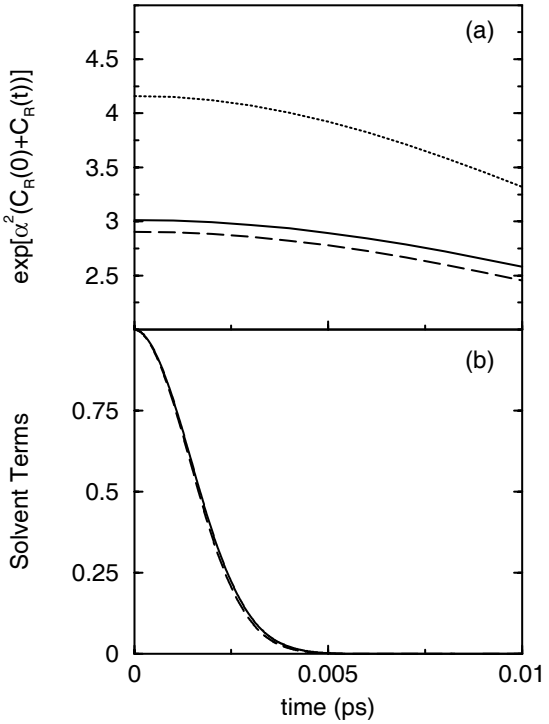

Figure **21**: (a) Comparison of R coordinate term $\exp\left\{\alpha_{\mu\nu}^2\left[C_R(0)+C_R(t)\right]\right\}$ calculated with $C_R(t)$ from classical molecular dynamics simulations (solid line) to this term with $C_R(t)$ for an undamped quantum harmonic oscillator given in Eq. **82** (dotted line) and with $C_R(t)$ for an undamped classical harmonic oscillator given in Eq. **83** (dashed line). (b) Comparison of solvent damping term $\exp\left\{-\frac{1}{\hbar^2}\int_0^t d\tau_1\int_0^{\tau_1} d\tau_2 C_\varepsilon(\tau_1-\tau_2)\right\}$ calculated with molecular dynamics simulations (solid line) and calculated with the frozen solvent approximation given in Eq. **84** (dashed line).

The solvent damping term $\exp\left\{-\frac{1}{\hbar^2}\int_0^t d\tau_1\int_0^{\tau_1} d\tau_2 C_\varepsilon(\tau_1-\tau_2)\right\}$ decays to zero on a time scale of ~0.005 ps, as shown in Figure **20b**. Since the solvent term decays much faster than the *R* coordinate term, the time scale of the decay of the flux is determined mainly by the solvent motions. Moreover, the decay time of the probability flux *j(t)* shown in Figure **20a** is short with respect to the initial decay time of the energy gap correlation function $C_\varepsilon(t)$ shown in Figure **18a**. As a result, only the initial value of the

energy gap correlation function (i.e., $C_\varepsilon(0) = \left\langle \delta\mathcal{E}^2 \right\rangle$) impacts the rate. In this case, the frozen solvent approximation, which considers only equilibrium fluctuations of the solvent, is valid. According to the short-time solvent approximation, $C_\varepsilon(t) = C_\varepsilon(0)$ and the solvent damping term (Eq. **84**) becomes a Gaussian:

$$\exp\left\{-\frac{1}{\hbar^2}\int_0^t d\tau_1 \int_0^{\tau_1} d\tau_2 C_\varepsilon\left(\tau_1-\tau_2\right)\right\} = \exp\left\{-\frac{C_\varepsilon(0)t^2}{2\hbar^2}\right\}. \qquad \text{Eq. } \mathbf{84}$$

Figure **21b** compares the exact solvent damping term with $C_\varepsilon(t)$ calculated from the simulations to the approximate expression in Eq. **84** . These results are virtually indistinguishable, indicating that the short-time solvent approximation is valid for these types of systems. Typically the solvent damping term decays faster as the solvent reorganization energy increases.

The probability flux correlation function for nonadiabatic single ET is analogous to Eq. **75** with the removal of all terms involving the *R* coordinate. For single ET, the dominant terms are the coherent term, which oscillates with a frequency dependent on the solvent reorganization energy, and the solvent damping term, which decays on a time scale dependent on the solvent reorganization energy. The solvent reorganization energies for PCET and single ET are typically similar for the same D_e–A_e separation because the proton moves only a relatively small distance (~0.5 Å) and therefore does not significantly influence the difference in solute charge density of the reactant and product states. Previously, Ando calculated the energy gap correlation functions and the corresponding spectral densities for a series of single ET reactions in water.[37] The results are qualitatively similar to those shown here, with similar time scales for the decay of the energy gap correlation functions.

As mentioned above, the decay of the solvent damping term in Eq. **75** dominates the flux because it decays faster than all other terms, so the *R*-dependent terms in Eq. **75** do not significantly impact the dynamical aspects of the probability flux correlation function. Thus, the dynamical behavior of the probability flux for PCET and ET reactions is similar. On the other hand, the magnitude of the rates for PCET and ET often

vary substantially because of differences in the nonadiabatic coupling $V_{\mu\nu}^{(0)}$. As given by Eq. **71** , the coupling for PCET can be approximated as the product of an electronic coupling and the overlap between the reactant and product proton vibrational wavefunction. The overlap factor tends to decrease the rate of PCET relative to the corresponding ET reaction.[46]

The probability flux expression in Eq. **75** is analogous to the probability flux expression given in Ref. 39 for vibrationally nonadiabatic PT reactions occurring on a single adiabatic electronic surface. In PCET reactions, however, the energy gap and coupling are defined for pairs of electron-proton vibronic surfaces corresponding to different electronic states. Thus, the coupling for PCET reactions involves ET nonadiabatic coupling as well as PT coupling. Moreover, the value of α (i.e., the R dependence of the coupling) could differ for PCET and PT reactions due to qualitatively different electrostatic interactions between the transferring proton and the solute electrons. In addition, the solvent reorganization is typically much smaller for PT than for PCET because the proton is transferred a shorter distance than the electron, so PCET reactions involve substantially greater differences in solute charge density for the reactant and product states. As a result of this difference in solvent reorganization energies, the period of the coherent term is smaller for PCET than for PT, and the solvent damping term decays faster for PCET than for PT.

Previously Borgis and Hynes calculated the time correlation functions for the energy gap, R coordinate frequency shift, and probability flux for a nonadiabatic PT reaction in a model polar aprotic solvent.[39] The results are qualitatively similar to those shown here in that the solvent decay dominates the probability flux. For PT, however, the decay of the probability flux correlation function is on a longer time scale (~0.02 ps) than the time scale of ~0.005 ps observed for PCET. Borgis and Hynes also found that the damping of the R mode is negligible and that the short-time solvent approximation is valid for nonadiabatic PT reactions.[39]

Conclusions

In this chapter we analyzed the dynamical aspects of a model PCET reaction in solution and tested the approximations previously invoked for the analytical calculation of rates. The rate of nonadiabatic PCET reactions is expressed as a time integral of a time-dependent probability flux correlation function. The dynamical behavior of the probability flux correlation function is dominated by a solvent damping term that depends on the energy gap correlation function. Only the initial value of the energy gap correlation function impacts the rate, so the short-time solvent approximation, in which only the equilibrium solvent fluctuations are considered, is valid for these types of systems. As the solvent reorganization energy increases, the probability flux correlation function decays faster. The time dependence of the correlation function for the proton donor-acceptor mode does not impact the dynamical behavior of the probability flux correlation function, but the initial value of this correlation function influences the magnitude of the rate. Solvent damping effects on the proton donor-acceptor mode are negligible, and the harmonic approximation for this mode is physically reasonable. The quantum effects of the proton donor-acceptor mode do not impact the dynamical behavior of the probability flux but slightly increase the magnitude of the rate. These results provide validation for the use of the analytical dynamical rate expressions discussed in Ref. 27.

We also compared the dynamical aspects of PCET to those of single ET and single PT. For PCET and ET reactions with similar solvent reorganization energies, the dynamical behavior of the probability flux correlation function, including the time scale of the decay, is similar. Typically the magnitude of the rate of a PCET reaction is significantly lower than that of the corresponding ET reaction because the coupling for PCET is the product of an electronic coupling and the overlap between the reactant and product proton vibrational wavefunctions. The dynamical behavior of nonadiabatic PT reactions is also qualitatively similar to that of PCET reactions, but typically PT reactions have much smaller solvent reorganization energies than PCET reactions. As a result, the probability flux correlation function decays on a significantly longer time scale for PT

than for PCET reactions. In addition, the magnitude of the rate will be influenced by differences in the couplings for PCET and PT. Specifically, PCET couplings are defined for pairs of vibronic surfaces corresponding to different electronic states, wheres PT reactions typically occur on a single adiabatic electronic surface.

References

(1) Babcock, G. T.; Barry, B. A.; Debus, R. J.; Hoganson, C. W.; Atamian, M.; McIntosh, L.; Sithole, I.; Yocum, C. F. *Biochemistry* **1989**, *28*, 9557.

(2) Okamura, M. Y.; Feher, G. *Annual Reviews of Biochemistry* **1992**, *61*, 861.

(3) Tommos, C.; Tang, X.-S.; Warncke, K.; Hoganson, C. W.; Styring, S.; McCracken, J.; Diner, B. A.; Babcock, G. T. *Journal of the American Chemical Society* **1995**, *117*, 10325.

(4) Hoganson, C. W.; Babcock, G. T. *Science* **1997**, *277*, 1953.

(5) Hoganson, C. W.; Lydakis-Simantiris, N.; Tang, X.-S.; Tommos, C.; Warncke, K.; Babcock, G. T.; Diner, B. A.; McCracken, J.; Styring, S. *Photosynthesis Research* **1995**, *47*, 177.

(6) Blomberg, M. R. A.; Siegbahn, P. E. M.; Styring, S.; Babcock, G. T.; Akermark, B.; Korall, P. *Journal of the American Chemical Society* **1997**, *119*, 8285.

(7) Diner, B. A.; Babcock, G. T. Structure, dynamics and energy conversion efficiency in photosystem II. In *Oxygenic Photosynthesis: The Light Reactions*; Ort, D. R., Yocum, C. F., Eds.; Kluwer: Dordrecht, The Netherlands, 1996; pp 213.

(8) Babcock, G. T.; Wikstrom, M. *Nature* **1992**, *356*, 301.

(9) Malmstrom, B. G. *Accounts of Chemical Research* **1993**, *26*, 332.

(10) Siegbahn, P. E. M.; Eriksson, L.; Himo, F.; Pavlov, M. *Journal of Physical Chemistry B* **1998**, *102*, 10622.

(11) Roth, J. P.; Lovel, S.; Mayer, J. M. *J. Am. Chem. Soc.* **2000**, *122*, 5486.

(12) Binstead, R. A.; Meyer, T. J. *Journal of the American Chemical Society* **1987**, *109*, 3287.

(13) Farrer, B. T.; Thorp, H. H. *Inorganic Chemistry* **1999**, *38*, 2497.

(14) Kirby, J. P.; Roberts, J. A.; Nocera, D. G. *Journal of the American Chemical Society* **1997**, *119*, 9230.

(15) Huynh, M. H. V.; Meyer, T. J. *Angew. Chem. Int. Ed.* **2002**, *41*, 1395.

(16) Sjodin, M.; Styring, S.; Akermark, B.; Sun, L.; Hammarstrom, L. *Journal of the American Chemical Society* **2000**, *122*, 3932.

(17) Knapp, M. J.; Rickert, K. W.; Klinman, J. P. *Journal of the American Chemical Society* **2002**, *124*, 3865.

(18) Cukier, R. I. *Journal of Physical Chemistry* **1994**, *98*, 2377.

(19) Cukier, R. I. *Journal of Physical Chemistry* **1996**, *100*, 15428.

(20) Cukier, R. I.; Nocera, D. G. *Annual Reviews of Physical Chemistry* **1998**, *49*, 337.

(21) Cukier, R. I. *Journal of Physical Chemistry A* **1999**, *103*, 5989.

(22) Cukier, R. I. *Journal of Physical Chemistry B* **2002**, *106*, 1746.
(23) Soudackov, A.; Hammes-Schiffer, S. *Journal of Chemical Physics* **1999**, *111*, 4672.
(24) Soudackov, A.; Hammes-Schiffer, S. *Journal of Chemical Physics* **2000**, *113*, 2385.
(25) Hammes-Schiffer, S. *Accounts of Chemical Research* **2001**, *34*, 273.
(26) Hammes-Schiffer, S. Proton-coupled electron transfer. In *Electron Transfer in Chemistry Vol I. Principles, Theories, Methods, and Techniques*; Balzani, V., Ed.; Wiley-VCH: Weinheim, 2001; pp 189.
(27) Soudackov, A. V.; Hatcher, E.; Hammes-Schiffer, S. *Journal of Chemical Physics* **2005**, *122*, 014505.
(28) Mayer, J. M.; Hrovat, D. A.; Thomas, J. L.; Borden, W. T. *Journal of the American Chemical Society* **2002**, *124*, 11142.
(29) Mincer, J. S.; Schwartz, S. D. *Journal of Chemical Physics* **2004**, *120*, 7755.
(30) Georgievskii, Y.; Stuchebrukhov, A. A. *Journal of Chemical Physics* **2000**, *113*, 10438.
(31) Moore, D. B.; Martinez, T. J. *Journal of Physical Chemistry A* **2000**, *104*, 2367.
(32) Siegbahn, P. E. M.; Blomberg, M. R. A.; Crabtree, R. H. *Theoretical Chemistry Accounts* **1997**, *97*, 289.
(33) Siebrand, W.; Smedarchina, Z. *Journal of Physical Chemistry B* **2004**, *108*, 4185.
(34) Kuznetsov, A. M.; Ulstrup, J. *Canadian Journal of Chemistry* **1999**, *77*, 1085.
(35) Barzykin, A. V.; Frantsuzov, P. A.; Seki, K.; Tachiya, M. Solvent Effects in Nonadiabatic Electron Transfer Reactions: Theoretical Aspects. In *Advances in Chemical Physics*; Prigogine, I., Rice, S. A., Eds., 2002; Vol. 123; pp p. 511.
(36) Suarez, A.; Silbey, R. *Journal of Chemical Physics* **1991**, *94*, 4809.
(37) Ando, K. *Journal of Chemical Physics* **1997**, *106*, 116.
(38) Borgis, D.; Lee, S.; Hynes, J. T. *Chemical Physics Letters* **1989**, *162*, 19.
(39) Borgis, D.; Hynes, J. T. *Journal of Chemical Physics* **1991**, *94*, 3619.
(40) Borgis, D.; Hynes, J. T. *Chemical Physics* **1993**, *170*, 315.
(41) Kuznetsov, A. M. *Charge Transfer in Physics, Chemistry, and Biology*; Gordon & Breach: Reading, 1995.
(42) Kuznetsov, A. M.; Ulstrup, J. *Electron Transfer in Chemistry and Biology: An Introduction to the Theory*; Wiley: Chichester, 1999.
(43) Newton, M. D.; Friedman, H. L. *Journal of Chemical Physics* **1988**, *88*, 4460.
(44) Ungar, L. W.; Newton, M. D.; Voth, G. A. *Journal of Physical Chemistry B* **1999**, *103*, 7367.
(45) Warshel, A. *Computer Modeling of Chemical Reactions in Enzymes and Solutions*; John Wiley & Sons, Inc.: New York, 1991.
(46) Iordanova, N.; Decornez, H.; Hammes-Schiffer, S. *Journal of the American Chemical Society* **2001**, *123*, 3723.

(47) Iordanova, N.; Hammes-Schiffer, S. *Journal of the American Chemical Society* **2002**, *124*, 4848.

(48) Trakhtenberg, L. I.; Klochikhim, V. L.; Pshezhetsky, S. Y. *Chemical Physics* **1982**, *69*, 121.

(49) Borgis, D. C.; Lee, S. Y.; Hynes, J. T. *Chemical Physics Letters* **1989**, *162*, 19.

(50) Chandler, D. *Liquids Freezing and Glass Transition*; Elsevier: Amsterdam, 1991; Vol. 51.

(51) Jorgensen, W. L. *Journal of the American Chemical Society* **1981**, *103*, 335.

(52) Jorgensen, W. L.; Chandreskhar, J.; Madura, J. D.; Impey, R. W.; Klein, M. L. *Journal of Chemical Physics* **1982**, *79*, 926.

(53) Ewald, P. P. *Ann. Phys.* **1921**, *64*, 253.

(54) Verlet, L. *Physical Review* **1967**, *159*, 98.

(55) Ryckaert, J. P.; Ciccotti, G.; Berendsen, H. J. C. *Journal of Computational Physics* **1977**, *23*, 327.

(56) Hoover, W. G. *Physical Review A* **1985**, *31*, 1695.

(57) Smith, W.; Forester, T. R. DL_POLY_2.14; CCLRC: Daresbury Laboratory, Warrington, England, 2003.

Chapter 5

Nonadiabatic Proton-Coupled Electron Transfer Reactions: Impact of Donor-Acceptor Vibrations, Reorganization Energies, and Couplings on Dynamics and Rates

Reproduced in part with permission from E. Hatcher, A. Soudackov, S. Hammes-Schiffer, *Journal of Physical Chemistry B.*, **2005**, 109, 18565-18574.

Introduction

Proton-coupled electron transfer (PCET) reactions, which involve the simultaneous transfer of an electron and a proton, play a significant role in many chemical and biological processes.[1-18] A variety of theoretical formulations have been applied to PCET reactions.[19-36] Typically PCET reactions are nonadiabatic because of the large distance between the electron donor and acceptor and the small overlap between the localized proton vibrational wavefunctions for the reactant and product vibronic states. In this regime, the reaction rate is determined by solvent fluctuations, which lead to degeneracy of the reactant and product vibronic states, and by the nonadiabatic coupling, which depends strongly on the proton donor-acceptor separation. Most of the previous studies of PCET reactions neglected the dynamical aspects of the proton donor-acceptor mode and the solvent or protein.

Recently we derived a dynamical nonadiabatic rate expression for PCET reactions in condensed phases.[29,37] The nonadiabatic rate constant is expressed in terms of the time integral of a time-dependent probability flux correlation function. This rate constant expression includes the dynamical fluctuations of the nonadiabatic coupling and the energy gap between the reactant and product states. The donor-acceptor mode can be

treated classically or quantum mechanically. This approach accounts for dynamical correlations between the fluctuations of the proton donor-acceptor distance and the nonadiabatic PCET coupling. Rate expressions were derived for PCET reactions in a number of well-defined limits for both dielectric continuum and molecular representations of the environment. The effects of the proton donor-acceptor and solvent dynamics on this probability flux correlation function were analyzed with classical molecular dynamics simulations.[37]

In this paper, we perform molecular dynamics simulations on model PCET systems to analyze the dependence of the PCET rate on key physical properties of the system and to test the validity of the approximations underlying previously derived rate expressions. The effects of the solvent reorganization energy, the proton donor-acceptor frequency, and the distance dependence of the nonadiabatic coupling on the probability flux correlation function are analyzed by varying the parameters in model systems. The impact of these properties on the magnitude of the PCET rate constant is also examined. The linear response approximation and the other main approximations underlying previously derived analytical rate expressions are tested for these model systems. The rates calculated from the molecular dynamics simulations are compared to those calculated with an analytical rate expression.

An outline of the paper is as follows. Section II summarizes the theoretical formulation for PCET reactions and describes the model systems. Section III presents the analyses of the dependence of the probability flux correlation function on key physical properties of the system and the main approximations underlying previously derived rate expressions. The conclusions and future directions are given in Section IV.

Methods

Theoretical formulation

PCET systems may be described in terms of the proton coordinate r_p, the proton donor-acceptor coordinate R, and the solvent coordinates ξ. In our theoretical formulation for nonadiabatic PCET reactions,[26,27] the active electrons and transferring proton are treated quantum mechanically. The PCET reaction is described in terms of nonadiabatic transitions between pairs of reactant (Iμ) and product (IIν) electron-proton vibronic states. Here I and II, respectively, denote the sets of reactant and product diabatic states, and μ and ν denote vibronic states within each set. The reactant vibronic surfaces $\varepsilon_\mu^{\mathrm{I}}(R,\xi)$ and product vibronic surfaces $\varepsilon_\nu^{\mathrm{II}}(R,\xi)$ are obtained by calculating the proton vibrational states for the reactant and product ET electronic states.

In our previous work,[26,27] the solute was represented by a four-state valence bond (VB) model.[38] For PCET reactions involving the transfer of one electron and one proton, the four diabatic electronic basis states are given in Eq. **85** :

$$\begin{aligned}
&(1a)\quad \mathrm{D_e^-}\cdots\cdots\mathrm{D_pH^+}\cdots\cdots\mathrm{A_p}\cdots\cdots\mathrm{A_e}\\
&(1b)\quad \mathrm{D_e^-}\cdots\cdots\mathrm{D_p}\cdots\cdots{}^{+}\mathrm{HA_p}\cdots\cdots\mathrm{A_e}\\
&(2a)\quad \mathrm{D_e}\cdots\cdots\mathrm{D_pH^+}\cdots\cdots\mathrm{A_p}\cdots\cdots\mathrm{A_e^-}\\
&(2b)\quad \mathrm{D_e}\cdots\cdots\mathrm{D_p}\cdots\cdots{}^{+}\mathrm{HA_p}\cdots\cdots\mathrm{A_e^-}
\end{aligned} \qquad \text{Eq. } \mathbf{85}$$

where 1 and 2 denote the ET state, and *a* and *b* denote the PT state. Typically for PCET reactions the solvated 1*a* and 2*b* states are lower in energy than the intermediate states 1*b* and 2*a* because the electrostatic interactions within the complex dominate over the solvation energies for bulky complexes.[39] Therefore, the reactant ET state is predominantly 1*a*, and the product ET state is predominantly 2*b*.

The coupling $V_{\mu\nu}$ between two vibronic states Iμ and IIν is defined in Eq. **86** as

$$V_{\mu\nu} = \left\langle \phi_\mu^{\mathrm{I}} \middle| V\left(r_{\mathrm{p}}, \xi^{\dagger}\right) \middle| \phi_\nu^{\mathrm{II}} \right\rangle_{\mathrm{p}} . \qquad \text{Eq. } \mathbf{86}$$

In Eq. **86** , the subscript of the angular brackets indicates integration over r_{p}, $\xi^{\dagger}$ represents the solvent coordinates at the intersection point of the reactant and product surfaces along the line connecting the minima of the surfaces, $V\left(r_p, \xi\right)$ is the electronic coupling between reactant and product states, and ϕ_μ^{I} and ϕ_ν^{II} are the proton vibrational wavefunctions of the reactant and product vibronic states, respectively. For many PCET systems,[40,41] the coupling, shown in Eq. **87** , is approximately of the form

$$V_{\mu\nu} \approx V^{\mathrm{el}} \left\langle \phi_\mu^{\mathrm{I}} \middle| \phi_\nu^{\mathrm{II}} \right\rangle_{\mathrm{p}} , \qquad \text{Eq. } \mathbf{87}$$

where V^{el} is a constant effective electronic coupling and $\left\langle \phi_\mu^{\mathrm{I}} \middle| \phi_\nu^{\mathrm{II}} \right\rangle_{\mathrm{p}}$ is the overlap between the reactant and product vibrational wavefunctions. The nonadiabatic coupling depends strongly on the proton donor-acceptor coordinate *R* because this coordinate modulates the proton tunneling distance and therefore the overlap $\left\langle \phi_\mu^{\mathrm{I}} \middle| \phi_\nu^{\mathrm{II}} \right\rangle_{\mathrm{p}}$. Although the coupling does not depend explicitly on the solvent coordinates in the relevant regime, the fluctuations of the solvent degrees of freedom can be dynamically coupled to the *R* motion, which in turn impacts the fluctuations of the nonadiabatic coupling.

Recently we developed nonadiabatic PCET rate expressions that include the dynamical effects of both the proton donor-acceptor motion and the solvent.[29] In this formulation, the electron and transferring proton are adiabatic with respect to the *R* coordinate and the solvent within the reactant and product states, and the *R*-mode is treated dynamically on the same level as the solvent modes. The nonadiabatic dynamical rate constant (Eq. **88**) can be expressed as

$$k^{\mathrm{dyn}} = \sum_{\mu}^{\{\mathrm{I}\}} P_\mu^{\mathrm{I}} \sum_{\nu}^{\{\mathrm{II}\}} k_{\mu\nu}^{\mathrm{dyn}} , \qquad \text{Eq. } \mathbf{88}$$

where P_{μ}^{I} is the Boltzmann weighting for the reactant state Iμ and $k_{\mu\nu}^{\mathrm{dyn}}$ is the partial rate constant describing nonadiabatic transitions between the reactant (Iμ) and product (IIν) vibronic states. The partial rate constant $k_{\mu\nu}^{\mathrm{dyn}}$, given in Eq. **89** , is the integral of the time-dependent probability flux correlation function $j_{\mu\nu}(t)$:

$$k_{\mu\nu}^{\mathrm{dyn}} = \frac{1}{\hbar^2}\int_{-\infty}^{\infty} j_{\mu\nu}(t)\,dt\,. \qquad \text{Eq. } \mathbf{89}$$

The probability flux correlation function $j_{\mu\nu}(t)$ can be represented in terms of the Heisenberg operators describing the time evolution of the energy gap and the coupling.[29] To facilitate the derivation of an analytical expression for the probability flux correlation function, the R dependence of the overall coupling $V_{\mu\nu}$ (Eq. **90**) is approximated by a single exponential:

$$V_{\mu\nu} \approx V_{\mu\nu}^{(0)} \exp\left[-\alpha_{\mu\nu}\left(R-\bar{R}^{\mathrm{I}\mu}\right)\right], \qquad \text{Eq. } \mathbf{90}$$

where $\bar{R}^{\mathrm{I}\mu}$ is the equilibrium value of the R coordinate on the reactant surface Iμ, $V_{\mu\nu}^{(0)}$ is the value of the coupling at $R=\bar{R}^{\mathrm{I}\mu}$, and $\alpha_{\mu\nu}$ can be estimated from the R dependence of the coupling. The justification for Eq. **90** is that the nonadiabatic coupling can be approximated as the product of a constant electronic coupling and the overlap of the reactant and product proton vibrational wavefunctions, as given in Eq. **87**. For a simple model based on two ground state harmonic oscillator wavefunctions with centers separated by R, the overlap increases exponentially with decreasing R. A more detailed justification for Eq. **90** is provided in Appendix C. The approximation in Eq. **90** has been shown to be reasonable for model PCET systems and was also used previously for nonadiabatic proton transfer systems.[42-44]

Performing a second order cumulant expansion, the probability flux correlation function is expressed in Eq. **91**

$$j_{\mu\nu}(t) = \left|V_{\mu\nu}^{(0)}\right|^2 \exp\left[\frac{i}{\hbar}\left\langle \mathcal{E}_{\mu\nu}\right\rangle t\right] \times \exp\left\{\alpha_{\mu\nu}^2\left[C_R(0)+C_R(t)\right] - \frac{2i\alpha_{\mu\nu}}{\hbar}\left\langle \tilde{D}_{\mu\nu}\right\rangle \int_0^t C_R(\tau)\,d\tau - \frac{1}{\hbar^2}\int_0^t d\tau_1 \int_0^{\tau_1} d\tau_2 C_{\mathcal{E}}(\tau_1-\tau_2) - \frac{1}{\hbar^2}\int_0^t d\tau_1 \int_0^{\tau_1} d\tau_2 C_D(\tau_1-\tau_2) C_R(\tau_1-\tau_2)\right\}, \quad \text{Eq. 91}$$

where the time evolution on the reactant vibronic surface is described in terms of the energy gap coordinate (Eq. **92**)

$$\mathcal{E}_{\mu\nu}(t) = \Delta\varepsilon_{\mu\nu}\left(\bar{R}^{\mathrm{I}\mu}, \xi(t)\right) = \varepsilon_\nu^{\mathrm{II}}\left(\bar{R}^{\mathrm{I}\mu}, \xi\right) - \varepsilon_\mu^{\mathrm{I}}\left(\bar{R}^{\mathrm{I}\mu}, \xi\right), \quad \text{Eq. 92}$$

the derivative of the energy gap (Eq. **93**)

$$\tilde{D}_{\mu\nu}(t) = \left.\frac{\partial \Delta\varepsilon_{\mu\nu}}{\partial R}\right|_{R=\bar{R}^{\mathrm{I}\mu}}, \quad \text{Eq. 93}$$

and the *R* mode. Note that these quantities are evaluated at $R = \bar{R}^{\mathrm{I}\mu}$ because the energy gap is expanded about $R = \bar{R}^{\mathrm{I}\mu}$ in the derivation of the rate expression.[29] The time correlation functions $C_{\mathcal{E}}(t)$, $C_R(t)$ and $C_D(t)$ are defined in Eq. **94**

$$C_{\mathcal{E}}(t) = \left\langle \delta\mathcal{E}_{\mu\nu}(0)\,\delta\mathcal{E}_{\mu\nu}(t)\right\rangle$$
$$C_R(t) = \left\langle \delta R(0)\,\delta R(t)\right\rangle \quad , \quad \text{Eq. 94}$$
$$C_D(t) = \left\langle \tilde{D}_{\mu\nu}(0)\,\tilde{D}_{\mu\nu}(t)\right\rangle$$

where $\delta\mathcal{E}_{\mu\nu}(t) = \mathcal{E}_{\mu\nu}(t) - \left\langle \mathcal{E}_{\mu\nu}\right\rangle$ and $\delta R(t) = R(t) - \langle R\rangle$. This formulation of the rate expression is similar to that previously derived for vibrationally nonadiabatic PT reactions occurring on a single adiabatic electronic surface.[42-45]

If the potential energy of the system is assumed to be harmonic along the *R* coordinate, the energy gap derivative defined in Eq. **93** becomes a constant term given in Eq. **95**

$$\tilde{D}_{\mu\nu} = \tilde{\Lambda}_{\mu\nu} \equiv -M\Omega^2 \Delta R_{\mu\nu}, \qquad \text{Eq. } \mathbf{95}$$

where $\Delta R = \bar{R}^{\mathrm{II}\nu} - \bar{R}^{\mathrm{I}\mu}$ is the difference between the equilibrium R coordinates on the product and reactant surfaces, and the R mode frequency Ω is given by in Eq. **96** .

$$M\Omega^2 = \left. \frac{\partial^2 \varepsilon_\mu^{\mathrm{I}}(R,\xi)}{\partial R^2} \right|_{R=\bar{R}^{\mathrm{I}\mu}} \qquad \text{Eq. } \mathbf{96}$$

In this limit, the energy gap derivative is independent of time, so $\left\langle \tilde{D}_{\mu\nu} \right\rangle = \tilde{\Lambda}_{\mu\nu}$ and $C_D(t) = \tilde{\Lambda}_{\mu\nu}^2$. For a symmetric system, $\tilde{\Lambda}_{\mu\nu} = 0$. As shown in Ref. 29 and 37, often the two terms in Eq. **91** that include this factor are negligible relative to the other terms due to the relatively small magnitude of $\left\langle \tilde{D}_{\mu\nu} \right\rangle$. In this paper, however, we do not assume harmonicity of the potential energy along the R coordinate, and we include all terms in our calculations of the nonadiabatic rates.

Classical molecular dynamics simulations of the full solute-solvent system on the reactant vibronic surface $\varepsilon_\mu^{\mathrm{I}}(R,\xi)$ can be used to calculate the input quantities for Eq. **91**. The $C_R(t)$ term is calculated from a molecular dynamics simulation with an unconstrained R, and the $\left\langle \mathcal{E}_{\mu\nu} \right\rangle$, $\left\langle \tilde{D}_{\mu\nu} \right\rangle$, $C_\mathcal{E}(t)$, and $C_D(t)$ terms are calculated from molecular dynamics simulations with the R coordinate constrained to $R = \langle R \rangle$, where $\langle R \rangle$ is obtained from the unconstrained simulation. (Note that we assumed $\bar{R}^{\mathrm{I}\mu} = \langle R \rangle$ in the derivation of the rate expression.) In the molecular dynamics simulations, the transferring proton is bound to the proton donor at a fixed distance corresponding to the reactant. For the calculation of the energy gap, the product state energy is obtained by moving the proton so that it is bound to the proton acceptor at the same fixed distance. This approximation neglects the effects of delocalization of the hydrogen nuclear wavefunction on the motion of the other nuclei.

Although the proton nucleus is described classically in the molecular dynamics simulations, the quantum mechanical nature of the proton is implicitly included in the

nonadiabatic rate expression through the nonadiabatic couplings between the reactant and product vibronic states. As shown in Eq. **87** , these couplings depend on the overlap between the reactant and product proton vibrational wavefunctions and thus are inherently quantum mechanical. The magnitude and distance dependence of the couplings in Eq. **90** could be fit to couplings obtained from purely quantum mechanical calculations using the nuclear-electronic orbital approach.[46,47]

The quantum mechanical behavior of the *R* motion can also be included in the nonadiabatic rate expression using the standard analytical expression for the time correlation function of an undamped quantum mechanical harmonic oscillator (Eq. **97**) for $C_R(t)$:[48]

$$C_R(t) = \frac{\hbar}{2M\Omega}\left[\coth\left(\tfrac{1}{2}\beta\hbar\Omega\right)\cos\Omega t + i\sin\Omega t\right]. \qquad \text{Eq. } \mathbf{97}$$

In Eq. **97** , the *R* coordinate motion is assumed to be harmonic, and the solvent damping effects on this harmonic motion are neglected. The classical (high temperature) analog of this expression is shown in Eq. **98** .

$$C_R(t) = \frac{1}{\beta M\Omega^2}\cos\Omega t \qquad \text{Eq. } \mathbf{98}$$

Model system

The probability flux correlation function is affected by changes in the proton donor-acceptor vibrational frequency (Ω), the solvent reorganization energy ($\lambda = \langle \mathcal{E}_{\mu\nu} \rangle$ for a symmetric system), and the distance dependence of the coupling ($\alpha_{\mu\nu}$). In this paper, we focus on nonadiabatic transitions between the lowest energy reactant and product states (i.e., include only $\mu = \nu = 0$ in the rate expression given in Eq. **88**). For notational simplicity, we drop the μ and ν subscripts for the remainder of the paper. We study three symmetric model systems with different values of Ω and λ to examine the

impact of these properties on the probability flux correlation function. The parameters of the three model systems are given in Table **4**. For each of these model systems we calculate the rate with α = 5, 10, 15, 20, 25 and 30 Å^{-1}.

The basic PCET model system consists of an electron donor and acceptor, a proton donor and acceptor, and a transferring proton. This model system is depicted in Figure **22**. The masses of the electron donor and acceptor are 100.0 g/mol, and the masses of the proton donor and acceptor are 14.0 g/mol. To maintain approximate linearity, harmonic angle restraints with force constants of 100.0 kcal/mol/deg^2 and equilibrium values of 180˚ are applied to the $D_eD_pA_e$ angle, the $D_eA_pA_e$ angle, and the D_pHA_p angle. The D_e–A_e distance is constrained to 8 Å, and the D_p–H distance is constrained to 1.1 Å. The potentials between the D_e–D_p , A_e–A_p , and D_p–A_p coordinates are represented as three coupled harmonic oscillators with identical force constants. The equilibrium distances for these harmonic potentials are 2.6 Å for D_e–D_p and A_e–A_p and 2.8 Å for D_p–A_p. The proton donor-acceptor vibrational frequency Ω is varied by changing the force constants for these harmonic potentials. The force constants for the harmonic potentials are 63.3 kcal/mol/Å^2 for Models 1 and 3 and 15.8 kcal/mol/Å^2 for Model 2. For the simulations with a constrained R distance, the D_p–A_p distance is constrained to $\langle R \rangle$, the average R distance obtained from the unconstrained simulations. The values of $\langle R \rangle$ are given in Table **4** .

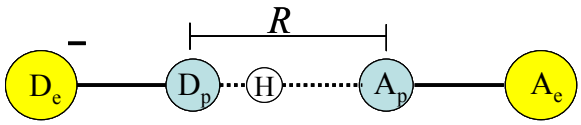

Figure **22**: Simple schematic picture of the solute for the coupled oscillator, model PCET system.

Table **4**: Calculated quantities from the molecular dynamics simulations for the three models.

	Model 1	Model 2	Model 3
$\langle R \rangle$, Å	2.83	2.92	2.85
Ω, cm^{-1}	387	198	388
$\langle \mathcal{E} \rangle$, kcal/mol	53.1	56.1	29.9
$\langle \delta\mathcal{E}^2 \rangle / 2k_B T$, kcal/mol	65.3	66.7	35.0
$\tilde{D}$, kcal/mol Å	3.9	3.8	2.4

The solute is solvated with 253 flexible TIP3P[49-51] water molecules in a cubic box with sides of 19.34 $Å^3$. The solvent-solute interactions include both electrostatic and van der Waals interactions. For the reactant state, the electron donor and acceptor have charges of –0.5e and +0.5e, respectively, and the proton donor and acceptor have charges of 0.0e and –0.5e, respectively. For the product state, the charges on the donors and acceptors are reversed. The proton always has a charge of +0.5e. These charges were chosen to ensure an overall neutral charge for the solute. The long range electrostatic interactions in the periodic system are treated with the Ewald method.[52] The van der Waals pair parameters for the interactions of the proton donor and acceptor with the oxygen atoms of the water molecules are ε = 0.15595 kcal/mol and σ = 4.1416 Å. The reorganization energy λ is varied by changing the van der Waals parameter σ of the electron donor and acceptor, where increasing the radii of the electron donor and acceptor decreases the solvent-solute electrostatic interactions and thereby decreases the solvent reorganization energy. The van der Waals pair parameters for the interactions of the electron donor and acceptor with the oxygen atoms of the water molecules are ε = 0.055 kcal/mol for all three models and σ = 4.075 Å for Models 1 and 2 and σ = 5.075 Å for Model 3.

All of the molecular dynamics simulations were performed with a modified version of DL_POLY 2.14.[53] The classical equations of motion were integrated with the

Verlet algorithm[54] with a time step of 0.5 fs. The solute constraints were applied with the SHAKE algorithm.[55] A canonical ensemble with a temperature of 300 K was maintained with a Nosè-Hoover thermostat with a relaxation time of 0.4 ps.[56] The system was equilibrated for 100 ps, and the data was collected for 200 ps. We verified that the results were converged by extending the simulation for Model 1 to 1 ns.

Results and Discussion

Impact of physical properties on dynamics and rates

In this subsection, we analyze the contributions to the probability flux correlation function given in Eq. **91**. For this purpose, we performed molecular dynamics simulations for the three different model systems described above. These model systems enable us to examine the impact of the solvent reorganization energy, proton donor-acceptor frequency, and distance dependence of the coupling on the probability flux correlation function and the magnitude of the rate.

The energy gap and R coordinate correlation functions provide insight into the relative timescales of the solvent and proton donor-acceptor motions. The energy gap correlation functions $C_{\varepsilon}(t)$ for Models 1 and 3 are depicted in Figure **23** . $C_{\varepsilon}(t)$ exhibits two different relaxation times: an initial fast decay on the time scale of ~50 fs and a slower exponential decay on a time scale of ~0.5 ps. The fast and slow components of the decay of the energy gap correlation function correspond to the relatively high-frequency librational modes of water and the lower frequency rotational and translational modes of water, respectively. Since Model 1 has a larger solvent reorganization energy than Model 3, $C_{\varepsilon}(0) = \left\langle \delta\mathcal{E}^2 \right\rangle$ is larger for Model 1. The R coordinate correlation functions $C_R(t)$ for Models 1 and 2 are depicted in Figure **24**. The R coordinate correlation function is highly oscillatory and decays on a slower timescale of ~3 ps due to the weak coupling of the R motion to the solvent degrees of freedom. The amplitude and

the period of the oscillations of the $C_R(t)$ term are larger for Model 2 than for Model 1 because Model 2 has a smaller proton donor-acceptor frequency.

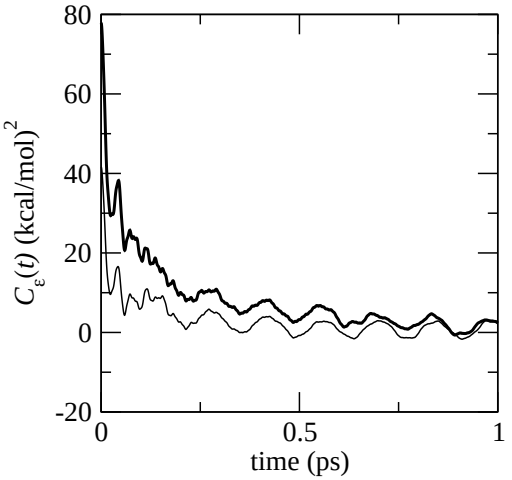

Figure **23**: Energy gap correlation function $C_\varepsilon(t)$ for Model 1 (thick line) and Model 3 (thin line). $C_\varepsilon(0)$ is larger for Model 1 because Model 1 has a large solvent reorganization energy.

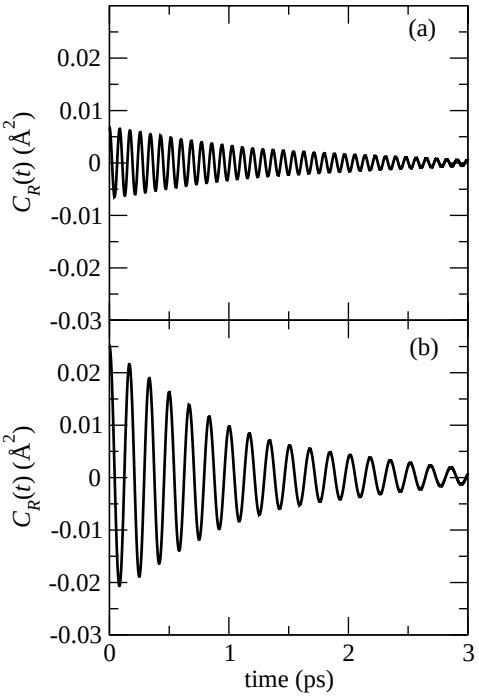

Figure **24**: Proton donor-acceptor distance correlation function $C_R(t)$ for (a) Model 1 and (b) Model 2. The amplitude and period of the oscillations of $C_R(t)$ are smaller for Model 1 because Model 1 has a larger proton donor-acceptor vibrational frequency.

The normalized spectral densities of the *R* coordinate time correlation functions for Models 1 and 2 are depicted in Figure **25** . The spectral density $J(\omega)$, which is given in Eq. **99** , is defined in terms of the cosine transform of the time correlation function $C(t)$ as

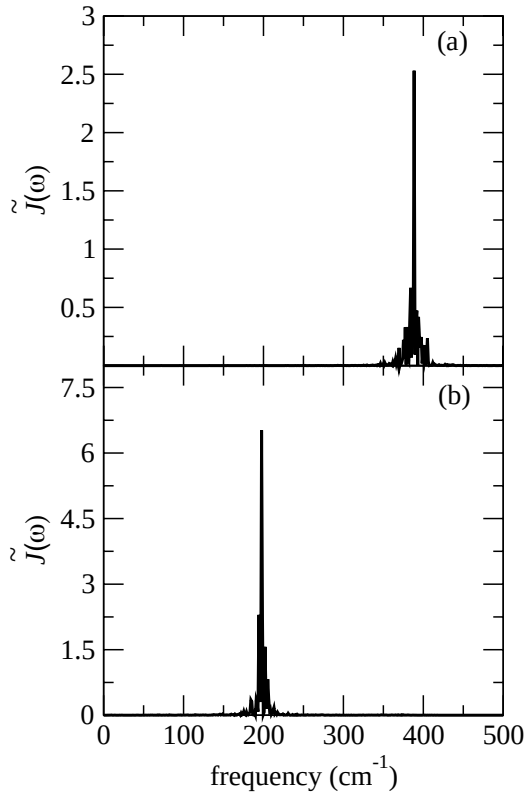

Figure **25**: Normalized spectral density $\tilde{J}(\omega)$ of the *R*-coordinate time correlation function $C_R(t)$ defined in Eq. **100** for (a) Model 1 and (b) Model 2. The peak in the spectral density corresponds to the average frequency of the proton donor-acceptor vibrational mode.

$$C(t) = \frac{8}{\pi\beta}\int_0^\infty \frac{J(\omega)}{\omega}\cos(\omega t)d\omega\,, \qquad \text{Eq. } \mathbf{99}$$

and the normalized spectral density is defined in Eq. **100** as[57]

$$\tilde{J}(\omega) = J(\omega)\Big/\int_0^\infty \frac{J(\omega)}{\omega}d\omega\,, \qquad \text{Eq. } \mathbf{100}$$

where $\beta = 1/k_B T$. The sharp peaks at ~400 cm^{-1} and ~200 cm^{-1} for Models 1 and 2, respectively, in the *R* coordinate spectral density correspond to the proton donor-acceptor

vibrational frequency. For an undamped harmonic oscillator, $C_R(t)$ would oscillate indefinitely with fixed amplitude, and the spectral density would be a delta function at the corresponding frequency. The calculated spectral densities of the *R* coordinate are broadened because the time correlation function $C_R(t)$ is damped due to solute-solvent coupling.

The dominant terms in the probability flux correlation function given in Eq. **91** are the quantum coherent term $F_Q(t) = \exp\left[\frac{i}{\hbar}\langle\mathcal{E}\rangle t\right]$, the solvent damping term $F_\varepsilon(t) = \exp\left[-\frac{1}{\hbar^2}\int_0^t d\tau_1 \int_0^{\tau_1} d\tau_2 C_\varepsilon(\tau_1 - \tau_2)\right]$, and the *R* coordinate term $F_R(t) = \exp\left\{\alpha^2\left[C_R(0) + C_R(t)\right]\right\}$. The quantum coherent and solvent damping terms are strongly influenced by changes in the solvent reorganization energy λ. The *R*-coordinate term is strongly influenced by the proton donor-acceptor vibrational frequency Ω and the parameter α, which describes the distance dependence of the nonadiabatic coupling. The three model systems described in Table **4** will enable us to investigate the impact of solvent reorganization energy, proton donor-acceptor vibrational frequency, and α on the probability flux correlation function. The normalized probability flux correlation functions and the dominant terms for all of the model systems with $\alpha = 10\,\text{Å}^{-1}$ are depicted in Figure **26**.

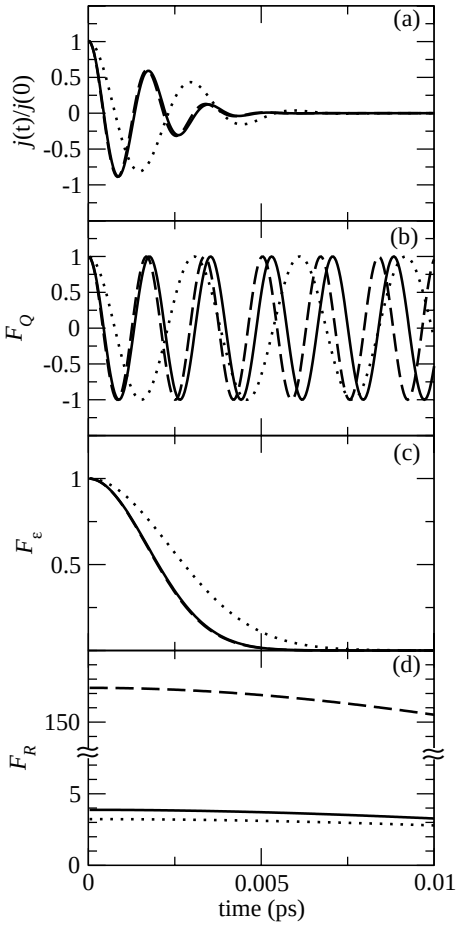

Figure **26**: Normalized probability flux correlation function $j(t)/j(0)$ and its dominant components for Model 1 (solid), Model 2 (dashed) and Model 3 (dotted) with $\alpha = 10$ Å^{-1}. (a) normalized probability flux correlation function, (b) quantum coherent term $F_Q(t) = \exp\left[\frac{i}{\hbar}\langle\mathcal{E}\rangle t\right]$, (c) solvent damping term $F_\varepsilon(t) = \exp\left\{-\frac{1}{\hbar^2}\int_0^t d\tau_1 \int_0^{\tau_1} d\tau_2 C_\mathcal{E}(\tau_1 - \tau_2)\right\}$, and (d) R-coordinate term $F_R(t) = \exp\left\{\alpha^2\left[C_R(0) + C_R(t)\right]\right\}$. The normalized probability flux and solvent damping term for Models 1 and 2 are nearly indistinguishable because they have similar solvent reorganization energies. Without normalization, the probability flux for Models 1 and 2 would not have similar magnitudes due to the different R coordinate terms. The real parts of the complex terms are plotted.

The highly oscillatory function $F_Q(t)$ depicted in Figure **26b** is the quantum coherent term, which describes the coherent oscillations of the quantum amplitude between the reactant and product vibronic states. The period of the oscillation for this

term is determined by the solvent reorganization energy of the system. The quantum coherent terms for Models 1 and 2 have similar periods of ~2 fs because the reorganization energies for these systems are similar. In contrast, the quantum coherent term for Model 3 has a larger period of ~3 fs because this system has a smaller solvent reorganization energy. The quantum coherent term is damped by other terms in Eq. **91** , thereby enabling the calculation of a reaction rate.

The solvent damping term $F_{\varepsilon}(t)$ dominates the decay of the probability flux because it decays to zero much faster than any other component in the probability flux. Similar to the coherent term, the solvent damping term depends on the solvent reorganization energy of the system. As illustrated in Figure **26c** , the solvent decay terms for Models 1 and 2 decay on similar timescales of ~5 fs, whereas the solvent decay term for Model 3 decays on a time scale of ~8 fs. The solvent term decays slower for Model 3 than for Models 1 and 2 because Model 3 has a smaller solvent reorganization energy. As a result, the probability flux decays on a slower time scale for Model 3 than for Model 1 and 2, as depicted in Figure **26a** . The magnitude of the rate, which is obtained by time integration of the probability flux correlation function, is smaller for Model 1 than for Model 3 because Model 1 has a larger solvent reorganization energy.

The R coordinate term $F_R(t)$ depicted in Figure **26d** depends on the proton donor-acceptor frequency Ω. As shown in Figure **24**, the magnitude of $C_R(0) = \langle \delta R^2 \rangle$ (i.e., the variance) increases as the proton donor-acceptor frequency decreases. As a result, the magnitude of the R coordinate term increases as the proton donor-acceptor frequency decreases. All of the R coordinate terms have a similar slope on the timescale of the probability flux decay, but the magnitude of the R coordinate term is much larger for Model 2 than for Models 1 and 3 due to the smaller proton donor-acceptor frequency for Model 2. Thus, the magnitudes of the rates calculated for Model 2 are larger by two orders of magnitude. The normalized probability flux is similar for Models 1 and 2, however, indicating that the dynamics of the reaction is not affected by the proton donor-acceptor frequency.

The value of the parameter α also strongly impacts the magnitude of the *R* coordinate term. Figure **27** depicts the rate as a function of α for all three model systems with $V^{(0)} = 0.1\text{kcal/mol}$. The rate increases with increasing α for all model systems, but the rate increases much faster with α for Model 2 because Model 2 has a lower proton donor-acceptor frequency. As shown in Figure **24b**, the smaller *R* distances are more accessible with a lower proton donor-acceptor frequency. The nonadiabatic coupling increases exponentially as the *R* distance decreases, thereby dramatically increasing the reaction rate. For small values of α (i.e., α < 5), the rate for Model 1 is lower than the rate for Model 3 because Model 1 has a larger solvent reorganization energy, which influences the solvent damping term as described above. For larger values of α, the rate for Model 3 is slightly lower than the rate for Model 1 because the F_R term is a little bit lower for Model 3, as illustrated in Figure **26d** , and this term becomes dominant for large values of α. The physical origin of this phenomenon is that the differences in the van der Waals pair parameters for the solute-solvent interactions in Models 1 and 3 slightly impact the *R* coordinate correlation function as well as the solvent reorganization energy.

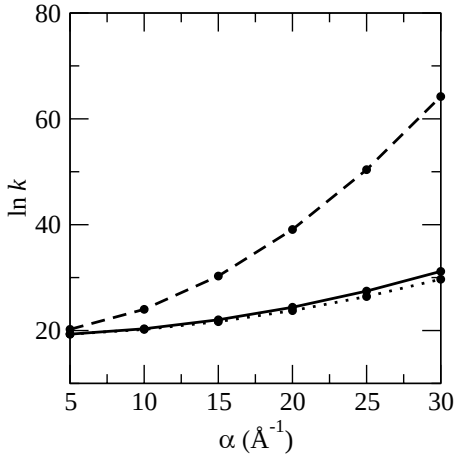

Figure **27**: The $\ln k$ as a function of α for Model 1 (solid), Model 2 (dashed), and Model 3 (dotted). The rate constant *k* is given in s^{-1}.

Analysis of approximations underlying rate expressions

In the first part of this subsection, we analyze the results of our molecular dynamics simulations to test the validity of the linear response approximation for model PCET systems. In the linear response approximation, the energy gap distribution function $P(\mathcal{E})$ is a Gaussian characterized by the average $\langle\mathcal{E}\rangle$ and the variance $\langle\delta\mathcal{E}^2\rangle$ of the energy gap reaction coordinate. Here we define the energy gap reaction coordinate $\mathcal{E}$ as in Eq. **92** , so the average value $\langle\mathcal{E}\rangle$ will be positive for the reactant state and negative for the product state. The free energy (Eq. **101**) is calculated from the distribution function using the standard prescription

$$G(\mathcal{E}) = -k_{\mathrm{B}}T \ln\left[P(\mathcal{E})\right], \qquad \text{Eq. } \mathbf{101}$$

where k_B is the Boltzmann constant and T is the temperature of the system.[45] In the linear response regime, the free energy curve is a parabola with minimum $\langle\mathcal{E}\rangle$ and force constant given in Eq. **102** .

$$f_{\mathrm{harm}} = \frac{k_B T}{\langle\delta\mathcal{E}^2\rangle} \qquad \text{Eq. } \mathbf{102}$$

Marcus theory for electron transfer reactions is based on the linear response approximation.[58] In this theory, the free energy surfaces G_{I} and G_{II} for the reactant and product states are assumed to be harmonic functions of the energy gap coordinate $\mathcal{E}$ with identical force constants given in Eq. **102** . The reactant and product free energy surfaces are related to each other as in Eq. **103** .[59,60]

$$G_{\mathrm{II}}(\mathcal{E}) = G_{\mathrm{I}}(\mathcal{E}) + \mathcal{E} \qquad \text{Eq. } \mathbf{103}$$

The corresponding reorganization energy (Eq. **104**) is expressed in terms of the variance as

$$\lambda_{\text{harm}} = \frac{\left\langle \delta\mathcal{E}^2 \right\rangle}{2k_{\text{B}}T}. \qquad \text{Eq. } \mathbf{104}$$

Within the Marcus theory framework, the activation free energy shown in Eq. **105** is a simple quadratic function of the reaction free energy ΔG^0 (driving force):

$$\Delta G^{\dagger} = \frac{\left(\Delta G^0 + \lambda_{\text{harm}}\right)^2}{4\lambda_{\text{harm}}}, \qquad \text{Eq. } \mathbf{105}$$

and the reaction rate constant (Eq. **106**) is exponentially dependent on the activation free energy:

$$k \propto \exp\left(-\Delta G^{\dagger}/k_B T\right). \qquad \text{Eq. } \mathbf{106}$$

This expression leads to the Marcus energy gap law, which is manifested by the inverted parabolic dependence of the logarithm of the rate constant on the reaction free energy. An analogous theoretical formulation has been developed for PCET reactions.[26,27]

The energy gap distribution function $P(\mathcal{E})$ is obtained from our molecular dynamics simulations by binning the energy gap values calculated along the molecular dynamics trajectory over 100 bins spanning the range of energies from 20 to 90 kcal/mol. The calculated distribution for Model 1, shown in Figure **28a,** resembles a Gaussian distribution centered at $\mathcal{E} = \langle\mathcal{E}\rangle$. The reactant free energy curve for Model 1, depicted in Figure **28b**, is calculated from Eq. **101** . For thermoneutral and symmetrical systems, the product free energy curve $G_{\text{II}}(\mathcal{E})$ can be obtained by reflecting the reactant free energy curve about the y-axis. In this case, the reorganization energy λ is defined as the average value of the energy gap in the reactant state (i.e., $\lambda = \langle\mathcal{E}\rangle$). The calculated values of the reorganization energy for all three model systems are given in Table **4** .

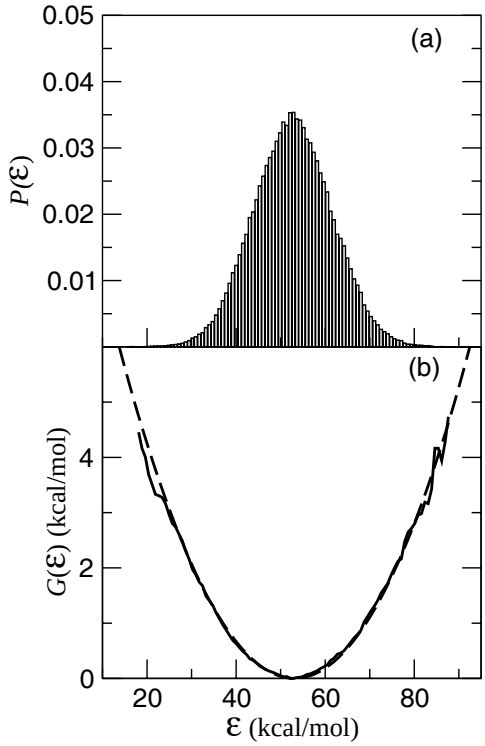

Figure **28**: (a) Histogram of the reactant energy gap distribution and (b) the reactant free energy curve calculated from the energy gap distribution with Eq. **101** (solid) and a parabola calculated from the function $G(\mathcal{E}) = \frac{1}{2}\frac{k_B T}{\langle \delta\mathcal{E}^2 \rangle}\left(\mathcal{E} - \langle \mathcal{E} \rangle\right)^2$ (dashed).

These numerical results obtained from molecular dynamics simulations can be compared to results calculated from linear response theory. The harmonic free energy curve obtained from linear response theory (i.e., with the force constant given in Eq. **102**) for Model 1 is shown in Figure **28b** for comparison to the free energy curve obained from Eq. **102** with the calculated energy gap distribution function. The nearly harmonic free energy curve, corresponding to an nearly Gaussian form of the energy gap distribution function, indicates that the linear response approximation is reasonable for this system. This observation provides validation for the use of the second-order cumulant expansion in the derivation of the rate expression.

For a quantitative analysis, Table **4** provides a comparison of the reorganization energies calculated from the variance with Eq. **104** and the reorganization energies

calculated from $\lambda = \langle \mathcal{E} \rangle$. The reorganization energies $\lambda = \langle \mathcal{E} \rangle$ are smaller than the corresponding reorganization energies calculated from Eq. **104** by 23%, 19%, and 17% for Models 1, 2, and 3, respectively. These discrepancies arise from slight anharmonicities of the free energy surfaces. We found that these discrepancies decrease as the van der Waals radii of the donors and acceptors are increased. This observation suggests that the deviations from linear response theory arise from short-range solvent-solute interactions that are neglected in the linear response approximation.

We also examine the dependence of the rate constant on the reaction free energy for comparison to the Marcus theory energy gap law. For this purpose, we add the driving force ΔG^0 to $\langle \mathcal{E} \rangle$ in the first exponential of the probability flux expression given by Eq. **91**. This process corresponds to shifting the product free energy surface vertically along the free energy axis by ΔG^0. The resulting $\ln k$ as a function of ΔG^0 for Model 1 is depicted in Figure **29**. This curve is a nearly symmetric inverted parabola with a maximum at $\Delta G^0 \approx \lambda = \langle \mathcal{E} \rangle = 53.13$ kcal/mol. For comparison, Figure **29** also depicts the symmetric Marcus inverted parabola obtained from the rate constant expression given in Eq. **106** in conjunction with the activation free energy given in Eq. **105** for $\lambda = \langle \mathcal{E} \rangle = 53.13$ kcal/mol. The shape of the Marcus inverted parabola is very similar to the curve obtained by integrating the probability flux correlation function in Eq. **91** . Thus, despite the slight anharmonicity of the free energy surfaces, the calculated energy gap law for this model PCET reaction provides further validation of the linear response approximation for this range of parameters at room temperature.

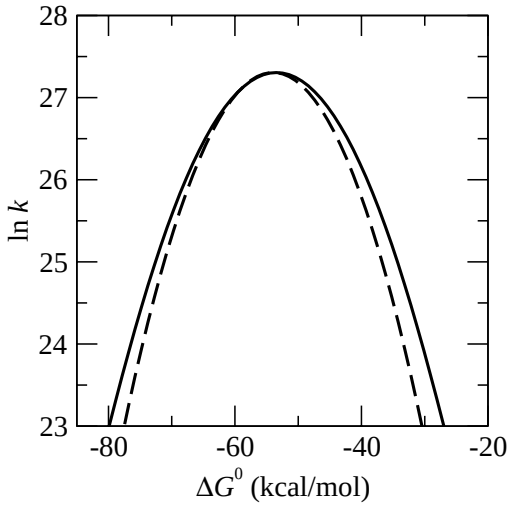

Figure **29**: The $\ln k$ as a function of the reaction free energy ΔG^0 for Model 1 with $\alpha = 10$ Å^{-1} (solid) and an inverted parabola calculated with $\ln k \propto -(\Delta G^0 + \lambda)^2 / (4\lambda k_B T)$ using $\lambda = \langle \mathcal{E} \rangle = 53.13$ kcal/mol (dashed). The parabolas were vertically adjusted so that the two maxima correspond to the same rates. The rate constant k is given in s^{-1}.

Deviations of the experimentally measured energy gap laws from the inverted parabolic behavior for electron transfer reactions have been explained by quantum vibronic effects,[61,62] different solute polarizabilities for reactant and product states,[63,64] and solvent nuclear quantum effects.[57,65] The present calculations do not include these additional factors. In particular, we do not account for the quantum effects arising from the excited electron-proton vibronic states, which are included in the general rate expression given in Eq. **88** . These excited states could lead to deviations of the energy gap law from the symmetric inverted parabolic behavior. For typical PCET systems with highly asymmetric proton potentials and relatively large vibronic energy level splittings in the reactant and product electronic states, however, these quantum effects are not expected to be significant.

In the remainder of this subsection, we test the additional approximations underlying the derivation of the following analytical rate expression (Eq. **107**) for nonadiabatic PCET reactions:[29]

$$k^{\text{anal}} = \frac{\left|V_{\mu\nu}^{(0)}\right|^2}{\hbar^2\Omega}\exp\left[\frac{2\lambda_\alpha\zeta}{\hbar\Omega}\right]\int_{-\infty}^{\infty} d\tau \exp\left[-\frac{1}{2}\chi\tau^2 + p\left(\cos\tau - 1\right) + i\left(q\sin\tau + \theta\tau\right)\right], \qquad \text{Eq. } \mathbf{107}$$

where the dimensionless parameters are defined in Eq. **108** [29]

$$\zeta = \coth\left(\tfrac{1}{2}\beta\hbar\Omega\right); \quad \chi = \frac{2\lambda}{\beta\hbar^2\Omega^2}; \quad \theta = \frac{\Delta G^0 + \lambda}{\hbar\Omega}; \quad p = \zeta\frac{\lambda_\alpha}{\hbar\Omega}; \quad q = \frac{\lambda_\alpha}{\hbar\Omega} \qquad \text{Eq. } \mathbf{108}$$

for symmetric systems with zero reorganization energy along the *R* coordinate. In Eq. **108** , λ is the solvent reorganization energy and $\lambda_\alpha = \hbar^2\alpha^2/2M$. This formulation of the rate expression is similar to that previously derived for vibrationally nonadiabatic PT reactions occurring on a single adiabatic electronic surface.[42-45] At the end of this subsection, we compare the rates calculated with Eq. **89** and Eq. **91** to those calculated with Eq. **107** .

In addition to the linear response approximation discussed in the previous section, the derivation of the analytical PCET rate expression given in Eq. **107** depends on two other approximations that can be tested with these molecular dynamics simulations. In the first approximation, the *R* coordinate motion is assumed to be harmonic, and the solvent damping effects on this harmonic motion are assumed to be negligible. In this case, the *R* coordinate time correlation function $C_R(t)$ can be replaced with the standard analytical expression for the time correlation function of an undamped quantum mechanical harmonic oscillator. Figure **30a** compares the *R* coordinate term, $F_R(t)$, for $C_R(t)$ calculated with classical molecular dynamics simulations ($F_R^{\text{MD}}(t)$), the classical harmonic oscillator approximation given in Eq. **98** ($F_R^{\text{cl}}(t)$), and the quantum harmonic oscillator approximation given in Eq. **97** ($F_R^{\text{q}}(t)$). The similarity between $F_R^{\text{MD}}(t)$ and $F_R^{\text{cl}}(t)$ indicates that anharmonic and solvent damping effects for the *R* motion are not significant on the time scale of the probability flux. Both $F_R^{\text{cl}}(t)$ and $F_R^{\text{q}}(t)$ are relatively constant on the relevant time scale, implying that the quantum effects of the *R* coordinate do not impact the dynamical behavior of the probability flux. Inclusion of the

quantum effects of the R coordinate, however, slightly increases the magnitude of the rates.

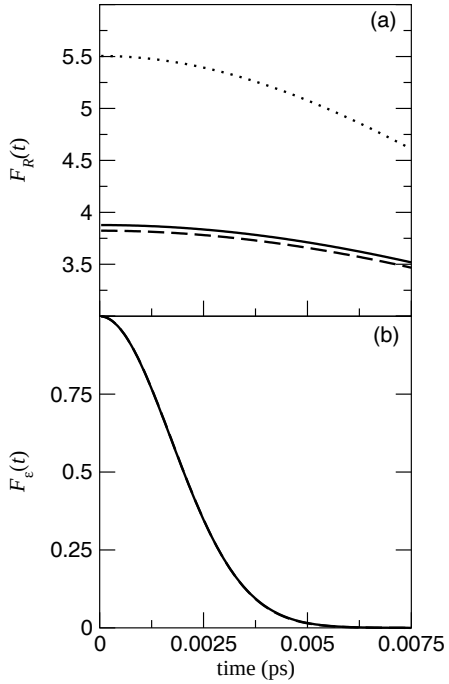

Figure **30**: (a) Comparison of the R coordinate term $F_R(t) = \exp\left\{\alpha_{\mu\nu}^2\left[C_R(0) + C_R(t)\right]\right\}$ for Model 1 with $\alpha = 10$ Å^{-1} calculated with $C_R(t)$ from the classical molecular dynamics simulations (solid) to this term with $C_R(t)$ for an undamped quantum harmonic oscillator given in Eq. **97** (dotted) and with $C_R(t)$ for an undamped classical harmonic oscillator given in Eq. **98** (dashed). (b) Comparison of the solvent damping term $F_\varepsilon(t) = \exp\left\{-\frac{1}{\hbar^2}\int_0^t d\tau_1 \int_0^{\tau_1} d\tau_2 C_\varepsilon(\tau_1 - \tau_2)\right\}$ for Model 1 calculated with classical molecular dynamics simulations (solid) and with the short-time approximation given in Eq. **109** (dashed). Note that the solid and dashed curves are virtually indistinguishable. The real parts of the complex terms are plotted.

The second approximation used in the derivation of the analytical PCET rate expression is the short-time approximation. In this limit, only the initial value of the energy gap correlation function impacts the rate, so $C_\varepsilon(t) \approx C_\varepsilon(0) \equiv \left\langle \delta\mathcal{E}^2 \right\rangle$. This approximation is valid when the decay time of the probability flux $j(t)$ is short with

respect to the initial decay time of the energy gap correlation function $C_{\varepsilon}(t)$. According to the short-time approximation, the solvent damping term becomes a Gaussian as shown in Eq. **109** :

$$\exp\left\{-\frac{1}{\hbar^2}\int_0^t d\tau_1 \int_0^{\tau_1} d\tau_2 C_{\varepsilon}\left(\tau_1-\tau_2\right)\right\} = \exp\left\{-\frac{\left\langle \delta\mathcal{E}^2\right\rangle t^2}{2\hbar^2}\right\}. \qquad \text{Eq. } \mathbf{109}$$

Figure **30b** compares the exact solvent damping term with $C_{\varepsilon}(t)$ calculated from the molecular dynamics simulations to the approximate expression in Eq. **109**. These two curves are indistinguishable, indicating that the short-time approximation is valid for these types of systems.

Figure **31** presents a comparison of the probability flux correlation functions calculated from the analytical expression given by Eq. **107** and from Eq. **91** in conjunction with the three different forms of the *R* coordinate term $F_R^{\mathrm{MD}}(t)$, $F_R^{\mathrm{cl}}(t)$, and $F_R^{\mathrm{q}}(t)$. All of the probability flux correlation functions were calculated for Model 1 with $\alpha = 10\,\text{Å}^{-1}$, and $\lambda = \left\langle \mathcal{E}\right\rangle$ in the analytical rate expression. The probability flux correlation function calculated from the analytical expression is similar to that calculated from Eq. **91** using $F_R^{\mathrm{q}}\left(t\right)$ because $C_R(t)$ is approximated as the time correlation function of an undamped quantum harmonic oscillator in the derivation of the analytical expression. The minor differences between these two curves are due to subtle deviations from linear response theory, as manifested by the quantitative difference between $\left\langle \mathcal{E}\right\rangle$ and $\left\langle \delta\mathcal{E}^2\right\rangle / 2k_{\mathrm{B}}T$. The two curves become virtually indistinguishable if λ is replaced by $\left\langle \delta\mathcal{E}^2\right\rangle / 2k_{\mathrm{B}}T$ in the $\chi = \dfrac{2\lambda}{\beta\hbar^2\Omega^2}$ term of the analytical expression. The minor differences between the probability flux correlation functions calculated from Eq. **91** using $F_R^{\mathrm{MD}}\left(t\right)$ and $F_R^{\mathrm{cl}}\left(t\right)$ arise from relatively small anharmonic and solvent damping effects on the *R* motion (i.e., on $C_R\left(t\right)$) in the molecular dynamics simulations.

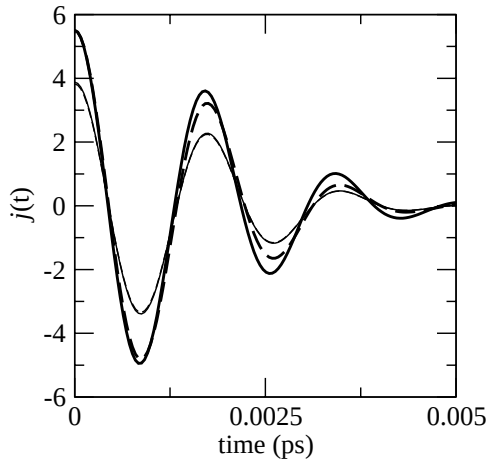

Figure **31**: Comparison of the probability flux correlation function *j(t)*, scaled by $\left|V^{(0)}\right|^2$, for Model 1 with $\alpha = 10$ Å^{-1} using Eq. **91** with $F_R^{\mathrm{MD}}(t)$ (thin solid), $F_R^{\mathrm{cl}}(t)$ (thin dashed) , and $F_R^{\mathrm{q}}(t)$ (thick dashed), and using the analytical expression given in Eq. **107** (thick solid). The real parts of the complex terms are plotted. Note that the solid and dashed thin lines are virtually indistinguishable.

The α dependence of the rates calculated from the time integration of these probability flux correlation functions is depicted in Figure **32** . The rates calculated from the analytical expression are virtually identical to the rates calculated with Eq. **91** using $F_R^{\mathrm{q}}(t)$ for all values of α. Similarly, the rates calculated with Eq. **91** using $F_R^{\mathrm{MD}}(t)$ and $F_R^{\mathrm{cl}}(t)$ are nearly indistinguishable.

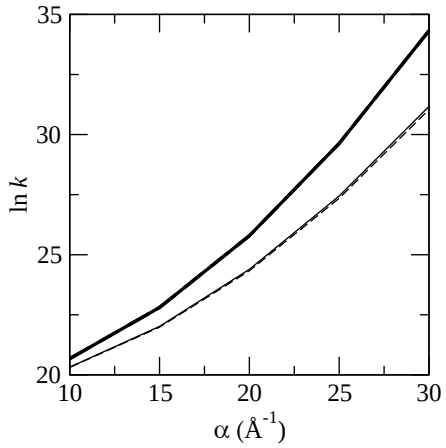

Figure **32**: The $\ln k$ for Model 1 using the probability flux correlation function in Eq. **91** with $F_R^{\mathrm{MD}}(t)$ (thin solid), $F_R^{\mathrm{cl}}(t)$ (thin dashed) , and $F_R^{\mathrm{q}}(t)$ (thick dashed), and using the analytical expression given in Eq. **107** (thick solid). The rate constant k is given in s^{-1}. Note that the solid and dashed lines are virtually indistinguishable in both cases.

Conclusions

In this paper, we performed molecular dynamics simulations on a model system to analyze fundamental aspects of PCET reactions in solution. We investigated the impact of the solvent reorganization energy, the proton donor-acceptor frequency, and the distance dependence of the nonadiabatic coupling on the dynamical aspects of the reaction and the magnitude of the rate. We also tested the validity of the linear response approximation for these types of systems and the additional approximations underlying previously derived analytical rate expressions. Furthermore, we compared the rates calculated from the molecular dynamics simulations to those calculated with the analytical rate expression.

Our analysis of the contributions to the nonadiabatic rate constant indicates that the solvent reorganization energy impacts the time dependence of the probability flux correlation function as well as the magnitude of the PCET rate. Increasing the solvent

reorganization energy leads to a faster decay of the solvent damping term in the probability flux correlation function. The solvent damping term dominates the decay of the probability flux because it decays to zero much faster than any other component in the probability flux. Thus, the solvent reorganization energy determines the time scale of the probability flux decay. The magnitude of the PCET rate constant, which is calculated by the time integration of the probability flux correlation function, decreases as the solvent reorganization energy increases when all other physical properties remain the same.

In contrast, we found that the proton donor-acceptor frequency strongly impacts the magnitude of the PCET rate but does not significantly influence the time dependence of the probability flux. Decreasing the proton donor-acceptor frequency increases the magnitude of the R coordinate term in the probability flux correlation function and therefore increases the magnitude of the overall PCET rate. The physical basis for this phenomenon is that a lower proton donor-acceptor frequency enables the sampling of smaller proton donor-acceptor distances, which are associated with significantly larger nonadiabatic couplings. The dynamics of the reaction is not affected by the proton donor-acceptor frequency because the R coordinate term is relatively constant on the time scale of the probability flux decay.

We also found that the distance dependence of the nonadiabatic coupling significantly impacts the magnitude of the PCET rate. The parameter α in the exponential of the nonadiabatic coupling dictates the increase of the nonadiabatic coupling as the proton donor-acceptor distance decreases. Increasing the parameter α increases the magnitude of the R coordinate term in the probability flux correlation function and therefore increases the magnitude of the overall PCET rate. The physical basis for this phenomenon is that a larger value of α leads to larger nonadiabatic couplings for the relevant proton donor-acceptor distances, which are smaller than the equilibrium distance. Moreover, the rate increases faster with α as the proton donor-acceptor frequency decreases because smaller proton donor-acceptor distances are more accessible with a lower proton donor-acceptor frequency.

In addition, we tested the validity of the linear response approximation for these types of PCET systems. The free energy profiles corresponding to the reactant and product vibronic states are nearly parabolic as functions of the energy gap coordinate, and the dependence of the rate on driving force is close to an inverted parabola. The minor deviations from linear response behavior were determined to arise from short-range solvent-solute interactions that are neglected in the linear response approximation. As in electron transfer theory, however, deviations from linear response theory are expected to arise from quantum vibronic effects, different solute polarizabilities for reactant and product states, and solvent nuclear quantum effects.

We also tested additional approximations underlying a previously derived analytical rate expression. The short-time approximation for the solvent was determined to be valid for these types of systems. Moreover, we found that anharmonic and solvent damping effects on the proton donor-acceptor motion are not significant on the time scale of the probability flux. Inclusion of the quantum effects of the proton donor-acceptor motion slightly increases the magnitude of the overall rate but does not impact the dynamical behavior of the probability flux. The rates calculated from the molecular dynamics simulations agree well with those calculated from the analytical rate expression. Thus, these studies provide validation for the use of the previously derived analytical rate expressions.

The analyses presented in this paper enhance our understanding of the fundamental physical principles of PCET reactions in solution. This theoretical formulation for PCET reactions is also applicable to larger, more complex biological systems. Furthermore, the analytical rate expressions enable the prediction of the temperature dependence of the rates and the deuterium kinetic isotope effects for comparison to experiment.

References

(1) Babcock, G. T.; Barry, B. A.; Debus, R. J.; Hoganson, C. W.; Atamian, M.; McIntosh, L.; Sithole, I.; Yocum, C. F. *Biochemistry* **1989**, *28*, 9557.

(2) Okamura, M. Y.; Feher, G. *Annual Reviews of Biochemistry* **1992**, *61*, 861.

(3) Knapp, M. J.; Rickert, K. W.; Klinman, J. P. *Journal of the American Chemical Society* **2002**, *124*, 3865.

(4) Sjodin, M.; Styring, S.; Akermark, B.; Sun, L.; Hammarstrom, L. *Journal of the American Chemical Society* **2000**, *122*, 3932.

(5) Huynh, M. H. V.; Meyer, T. J. *Angew. Chem. Int. Ed.* **2002**, *41*, 1395.

(6) Kirby, J. P.; Roberts, J. A.; Nocera, D. G. *Journal of the American Chemical Society* **1997**, *119*, 9230.

(7) Farrer, B. T.; Thorp, H. H. *Inorganic Chemistry* **1999**, *38*, 2497.

(8) Binstead, R. A.; Meyer, T. J. *Journal of the American Chemical Society* **1987**, *109*, 3287.

(9) Roth, J. P.; Lovel, S.; Mayer, J. M. *J. Am. Chem. Soc.* **2000**, *122*, 5486.

(10) Siegbahn, P. E. M.; Eriksson, L.; Himo, F.; Pavlov, M. *Journal of Physical Chemistry B* **1998**, *102*, 10622.

(11) Blomberg, M. R. A.; Siegbahn, P. E. M.; Styring, S.; Babcock, G. T.; Akermark, B.; Korall, P. *Journal of the American Chemical Society* **1997**, *119*, 8285.

(12) Hoganson, C. W.; Babcock, G. T. *Science* **1997**, *277*, 1953.

(13) Hoganson, C. W.; Lydakis-Simantiris, N.; Tang, X.-S.; Tommos, C.; Warncke, K.; Babcock, G. T.; Diner, B. A.; McCracken, J.; Styring, S. *Photosynthesis Research* **1995**, *47*, 177.

(14) Tommos, C.; Tang, X.-S.; Warncke, K.; Hoganson, C. W.; Styring, S.; McCracken, J.; Diner, B. A.; Babcock, G. T. *Journal of the American Chemical Society* **1995**, *117*, 10325.

(15) G.T. Babcock, B. A. D., J. McCracken, S. Styring. *Photosynthesis Research* **1995**, *47*, 177.

(16) Diner, B. A.; Babcock, G. T. Structure, dynamics and energy conversion efficiency in photosystem II. In *Oxygenic Photosynthesis: The Light Reactions*; Ort, D. R., Yocum, C. F., Eds.; Kluwer: Dordrecht, The Netherlands, 1996; pp 213.

(17) Babcock, G. T.; Wikstrom, M. *Nature* **1992**, *356*, 301.

(18) Malmstrom, B. G. *Accounts of Chemical Research* **1993**, *26*, 332.

(19) Cukier, R. I. *Journal of Physical Chemistry* **1994**, *98*, 2377.

(20) Cukier, R. I. *Journal of Physical Chemistry* **1996**, *100*, 15428.
(21) Cukier, R. I. *Journal of Physical Chemistry A* **1999**, *103*, 5989.
(22) Cukier, R. I. *Journal of Physical Chemistry B* **2002**, *106*, 1746.
(23) Cukier, R. I. *Biochimica et Biophysica Acta-Bioenergetics* **2004**, *1655*, 37.
(24) Cukier, R. I.; Nocera, D. G. *Annual Reviews of Physical Chemistry* **1998**, *49*, 337.
(25) Hammes-Schiffer, S. *Accounts of Chemical Research* **2001**, *34*, 273.
(26) Soudackov, A.; Hammes-Schiffer, S. *Journal of Chemical Physics* **1999**, *111*, 4672.
(27) Soudackov, A.; Hammes-Schiffer, S. *Journal of Chemical Physics* **2000**, *113*, 2385.
(28) Hammes-Schiffer, S. Proton-coupled electron transfer. In *Electron Transfer in Chemistry Vol I. Principles, Theories, Methods, and Techniques*; Balzani, V., Ed.; Wiley-VCH: Weinheim, 2001; pp 189.
(29) Soudackov, A. V.; Hatcher, E.; Hammes-Schiffer, S. *Journal of Chemical Physics* **2005**, *122*, 014505.
(30) Mayer, J. M.; Hrovat, D. A.; Thomas, J. L.; Borden, W. T. *Journal of the American Chemical Society* **2002**, *124*, 11142.
(31) Mincer, J. S.; Schwartz, S. D. *Journal of Chemical Physics* **2004**, *120*, 7755.
(32) Moore, D. B.; Martinez, T. J. *Journal of Physical Chemistry A* **2000**, *104*, 2367.
(33) Georgievskii, Y.; Stuchebrukhov, A. A. *Journal of Chemical Physics* **2000**, *113*, 10438.
(34) Siegbahn, P. E. M.; Blomberg, M. R. A.; Crabtree, R. H. *Theoretical Chemistry Accounts* **1997**, *97*, 289.
(35) Siebrand, W.; Smedarchina, Z. *Journal of Physical Chemistry B* **2004**, *108*, 4185.
(36) Kuznetsov, A. M. *Charge Transfer in Physics, Chemistry, and Biology*; Gordon & Breach: Reading, 1995.
(37) Hatcher, E.; Soudackov, A.; Hammes-Schiffer, S. *Chemical Physics* **2005**, *319*, 93.
(38) Warshel, A. *Computer Modeling of Chemical Reactions in Enzymes and Solutions*; John Wiley & Sons, Inc.: New York, 1991.
(39) Hammes-Schiffer, S.; Iordanova, N. *Biochimica et Biophysica Acta-Bioenergetics* **2004**, *1655*, 29.
(40) Iordanova, N.; Decornez, H.; Hammes-Schiffer, S. *Journal of the American Chemical Society* **2001**, *123*, 3723.
(41) Iordanova, N.; Hammes-Schiffer, S. *Journal of the American Chemical Society* **2002**, *124*, 4848.
(42) Suarez, A.; Silbey, R. *Journal of Chemical Physics* **1991**, *94*, 4809.
(43) Trakhtenberg, L. I.; Kochikhim, V. L.; Pshezhetsky, S. Y. *Chemical Physics* **1982**, *69*, 121.
(44) Borgis, D.; Lee, S.; Hynes, J. T. *Chemical Physics Letters* **1989**, *162*, 19.
(45) Borgis, D.; Hynes, J. T. *Journal of Chemical Physics* **1991**, *94*, 3619.

(46) Webb, S. P.; Iordanov, T.; Hammes-Schiffer, S. *Journal of Chemical Physics* **2002**, *117*, 4106.

(47) Pak, M. V.; Swalina, C.; Webb, S. P.; Hammes-Schiffer, S. *Chemical Physics* **2004**, *304*, 227.

(48) Chandler, D. *Liquids Freezing and Glass Transition*; Elsevier: Amsterdam, 1991; Vol. 51.

(49) Jorgensen, W. L. *Journal of the American Chemical Society* **1981**, *103*, 335.

(50) Jorgensen, W. L.; Chandreskhar, J.; Madura, J. D.; Impey, R. W.; Klein, M. L. *Journal of Chemical Physics* **1982**, *79*, 926.

(51) Cornell, W. D.; Cieplak, P.; Bayly, C. I.; Gould, I. R.; Merz, K. M.; Ferguson, D. M.; Spellmeyer, D. C.; Fox, T.; Caldwell, J. W.; Kollman, P. A. *Journal of the American Chemical Society* **1995**, *117*, 5179.

(52) Ewald, P. P. *Ann. Phys.* **1921**, *64*, 253.

(53) Smith, W.; Forester, T. R. DL_POLY_2.14; CCLRC: Daresbury Laboratory, Warrington, England, 2003.

(54) Verlet, L. *Physical Review* **1967**, *159*, 98.

(55) Ryckaert, J. P.; Ciccotti, G.; Berendsen, H. J. C. *Journal of Computational Physics* **1977**, *23*, 327.

(56) Hoover, W. G. *Physical Review A* **1985**, *31*, 1695.

(57) Ando, K. *Journal of Chemical Physics* **1997**, *106*, 116.

(58) Marcus, R. A. *Annual Reviews of Physical Chemistry* **1964**, *15*, 155.

(59) Warshel, A. *Journal of Physical Chemistry* **1982**, *86*, 2218.

(60) Hwang, J.-K.; Warshel, A. *Journal of the American Chemical Society* **1987**, *109*, 715.

(61) M. Bixon, J. J. *J. Phys. Chem.* **1991**, *95*, 1941.

(62) S. Efrima, M. B. *Chemical Physics* **1976**, *13*, 447.

(63) Matyushov, D. V.; Voth, G. A. *Journal of Chemical Physics* **2000**, *113*, 5413.

(64) Small, D. W.; Matyushov, D. V.; Voth, G. A. *Journal of the American Chemical Society* **2003**, *125*, 7470.

(65) Ando, K. *Journal of Chemical Physics* **2001**, *114*, 9470.

Chapter 6

Proton-Coupled Electron Transfer in Soybean Lipoxygenase: Dynamical Behavior and Temperature Dependence of Kinetic Isotope Effects

Introduction

Lipoxygenase is a non-heme iron metalloenzyme that catalyzes the oxidation of unsaturated fatty acids. The human form is medically significant because it assists in the production of leukotrienes and lipoxins, which play a role in immune response.[1] Moreover, the inhibition of lipoxygenase has been found to aid in the prevention of cancer.[2-5] Kinetic studies have been conducted for human lipoxygenase[6, 7] and soybean lipoxygenase-1 (SLO)[8, 9] with linoleic acid, the natural substrate for SLO. High-resolution crystal structures have been solved for SLO.[10, 11] In addition, a number of mutants of SLO have been studied experimentally.[9, 11, 12]

The reaction catalyzed by SLO is depicted in Figure **33**. In the first step of the catalytic reaction, the pro-*S* hydrogen from the C11 carbon of the linoleic acid substrate is abstracted by the Fe(III)-OH cofactor to form a radical intermediate substrate and Fe(II)-OH_2. Subsequently, the radical form of the linoleic acid reacts with dioxygen to ultimately form hydroperoxyoctadecadienoic acid and the ferric form of the iron cofactor. Quantum mechanical calculations[13] suggest that the first step occurs by a proton-coupled electron transfer (PCET) mechanism, in which the electron transfers from the π-system of the substrate to the iron of the cofactor, while the proton transfers from the C11 carbon of the substrate to the hydroxyl ligand of the cofactor. Moreover, analysis of the

thermodynamic properties of the single proton transfer and electron transfer reactions, as well as the concerted PCET mechanism, indicates that the single proton and electron transfer reactions are highly endothermic, whereas the PCET reaction is exothermic.[9, 14] Thus, the electron and proton transfer simultaneously to avoid the high-energy intermediates.

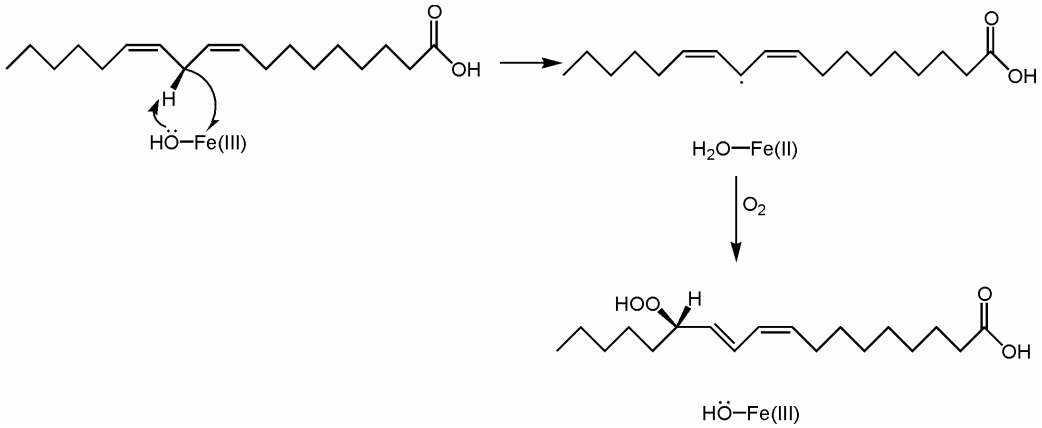

Figure **33**: The reaction of soybean lipoxygenase with its natural substrate linoleic acid. In the first step of this reaction, hydrogen is abstracted from the linoleic acid to the iron cofactor. In the second step, dioxygen binds to the radical fatty acid to form a hydroperoxide.

Klinman and coworkers determined that the hydrogen abstraction step in the SLO reaction is rate limiting above 32° C.[9] The deuterium kinetic isotope effect (KIE) of this reaction was observed to be unusually high with a value of 81 at room temperature,[8, 9, 15-17] and the temperature dependences of the rates and KIEs were found to be relatively weak.[9] Moreover, human lipoxygenase was observed to behave similarly.[6, 7] This behavior was interpreted to indicate that hydrogen tunneling, as well as a vibrational promoting mode, play important roles in these enzymatic reactions.[9, 14] These results have stimulated extensive theoretical activity.

The SLO reaction has been studied with density functional theory[13, 18-20] and various quantum/classical approaches.[8, 9, 14, 17, 21-27] Most of these theoretical studies were based on simple models and did not include the explicit enzyme environment. An exception is the work of Warshel and coworkers.[25, 26] They represented the explicit enzyme environment with an electronically adiabatic empirical valence bond potential

and included nuclear quantum effects with path integral methods, but they were unable to reproduce the experimental temperature dependence of the KIE. Our vibronically nonadiabatic treatment of this reaction with an empirical valence bond (EVB) potential and a dielectric continuum representation of the enzyme environment resulted in the experimentally observed temperature dependence of the rates and KIE.[14] The vibronically nonadiabatic treatment is applicable to systems for which the vibronic coupling, which can be approximated as the product of an electronic coupling and the overlap between the reactant and product hydrogen vibrational wavefunctions, is less than the thermal energy. Our previous calculations illustrated that the proton donor-acceptor motion plays a vital role in facilitating the hydrogen tunneling process. On the other hand, this previous study neglected the explicit enzyme environment and all dynamical effects.

In this paper, we examine the dynamical aspects of the PCET reaction catalyzed by SLO using a vibronically nonadiabatic molecular dynamics method with an explicit enzyme environment. In this approach, the vibronically nonadiabatic rate constant is represented by the time integral of the probability flux correlation function, which is expressed in terms of the vibronic coupling, the average energy gap and proton donor-acceptor distance, and the time correlation functions of the energy gap and the proton donor-acceptor distance.[28-30] This method accounts for the dynamical correlation between the proton donor-acceptor motion and the nonadiabatic coupling. Previously this approach was applied to model PCET reactions in solution, but it has not yet been applied to PCET in an enzyme. Here we test the underlying assumptions of this formulation for an enzymatic system and study the dynamical behavior of the protein, substrate, and cofactor. We also investigate the physical basis for the experimentally observed magnitude and temperature dependence of the KIEs for this enzyme reaction.

An outline of the paper is as follows. In section II, we describe the theoretical formulation for vibronically nonadiabatic PCET reactions and the methodology used for the molecular dynamics simulations. Section III presents the results, including the validation of linear response theory for this system, the analysis of the time correlation functions for the protein and proton donor-acceptor motions, and the analysis of the

magnitude and temperature dependence of the KIEs. In Section IV, we summarize the main findings of this study and discuss potential future directions.

Theory and Methods

Theoretical formulation

In this paper, we apply a vibronically nonadiabatic dynamical formulation for PCET reactions to the SLO reaction. In this formulation, the active electrons and transferring proton are treated quantum mechanically, and the PCET reaction is described in terms of nonadiabatic transitions between pairs of reactant and product mixed electron-proton vibronic states. The nonadiabatic rate constant is expressed as the time integral of the probability flux correlation function shown in Eq. **110**

$$k = \sum_{\mu} P_{\mu} \sum_{\nu} \frac{1}{\hbar^2} \int_{-\infty}^{\infty} j_{\mu\nu}(t)\, dt \,, \qquad \text{Eq. } \mathbf{110}$$

where the summations are over the reactant and product vibronic states, P_{μ} is the Boltzmann probability for the reactant state μ, and $j_{\mu\nu}(t)$ is the probability flux correlation function for the reactant/product pair of vibronic states $\mu\nu$.

The nonadiabatic coupling $V_{\mu\nu}$ between the reactant and product vibronic states is strongly influenced by the proton donor-acceptor coordinate *R*. This coupling can often be approximated as shown in Eq. **111**

$$V_{\mu\nu}(R) \approx V^{\mathrm{el}} S_{\mu\nu}(R) \,, \qquad \text{Eq. } \mathbf{111}$$

where V^{el} is a constant effective electronic coupling and $S_{\mu\nu}(R)$ is the overlap between the reactant and product proton vibrational wavefunctions at distance *R*. In the region about the equilibrium value of the *R* coordinate, this coupling can be approximated to be of the form given in Eq. **112**

$$V_{\mu\nu}(R) \approx V^{\mathrm{el}} S_{\mu\nu}^{(0)} \exp\left[-\alpha_{\mu\nu}\left(R-\bar{R}_{\mu}\right)\right], \qquad \text{Eq. } \mathbf{112}$$

where $\bar{R}_{\mu}$ is the equilibrium value of the *R* coordinate on the reactant surface and $S_{\mu\nu}^{(0)} = S_{\mu\nu}\left(\bar{R}_{\mu}\right)$. Note that the nonadiabatic coupling includes the quantum mechanical behavior of the transferring proton.

We derived an expression for the probability flux correlation function using linear response theory in conjunction with the form of the coupling given in Eq. **112** .[28] In this case, the probability flux correlation function is expressed as Eq. **113**

$$\begin{aligned} j_{\mu\nu}(t) = & \left|V^{\mathrm{el}} S_{\mu\nu}^{(0)}\right|^2 \exp\left[\frac{i}{\hbar}\left\langle \mathcal{E}_{\mu\nu}\right\rangle t\right] \\ & \times \exp\left\{\alpha_{\mu\nu}^2\left[C_R(0)+C_R(t)\right]\right\} \times \exp\left\{-\frac{1}{\hbar^2}\int_0^t d\tau_1 \int_0^{\tau_1} d\tau_2 C_{\mathcal{E}}(\tau_1-\tau_2)\right\}, \end{aligned} \qquad \text{Eq. } \mathbf{113}$$

where $\mathcal{E}_{\mu\nu}$ is the energy gap (i.e., the difference between the energies of the reactant state μ and the product state ν) for $R=\bar{R}_{\mu}$, the time correlation functions are defined as Eq. **114**

$$\begin{aligned} C_{\mathcal{E}}(t) &= \left\langle \delta\mathcal{E}_{\mu\nu}(0)\,\delta\mathcal{E}_{\mu\nu}(t)\right\rangle \\ C_R(t) &= \left\langle \delta R(0)\,\delta R(t)\right\rangle \end{aligned}, \qquad \text{Eq. } \mathbf{114}$$

where $\delta\mathcal{E}_{\mu\nu}(t) = \mathcal{E}_{\mu\nu}(t) - \left\langle \mathcal{E}_{\mu\nu}\right\rangle$ and $\delta R(t) = R(t) - \langle R\rangle$, and the angular brackets indicate averaging on the reactant vibronic surface. Here we have omitted terms involving the derivative of the energy gap with respect to *R* because these terms have been shown previously to be negligible. This formulation of the rate expression is similar

to that previously derived for vibrationally nonadiabatic PT reactions occurring on a single adiabatic electronic surface.[31-35]

The input quantities for the probability flux correlation function given in Eq. **113** can be calculated with classical molecular dynamics simulations of the system on the reactant vibronic surface. The time correlation function $C_R(t)$ and the average value $\overline{R}$ are calculated from classical molecular dynamics simulations on the reactant vibronic surface with an unconstrained *R* coordinate. The average energy gap $\langle \mathcal{E}_{\mu\nu} \rangle$ and the time correlation function $C_\varepsilon(t)$ are calculated from classical molecular dynamics simulations on the reactant vibronic surface with the *R* coordinate constrained to $R = \overline{R}$. The energy gap is calculated for each time step using a two-state EVB model representing the reactant and product vibronic surfaces.

To investigate the temperature dependence of the kinetic isotope effects, we invoke two additional approximations that have been shown to be valid for the SLO reaction. The first approximation relies on the observation that only the initial value of the energy gap correlation function impacts the rate, so the solvent damping term becomes a Gaussian shown in Eq. **115**

$$F_\varepsilon(t) \equiv \exp\left\{-\frac{1}{\hbar^2}\int_0^t d\tau_1 \int_0^{\tau_1} d\tau_2 C_\varepsilon(\tau_1 - \tau_2)\right\} \approx \exp\left\{-\frac{\langle \delta\mathcal{E}^2 \rangle t^2}{2\hbar^2}\right\}. \qquad \text{Eq. } \mathbf{115}$$

In linear response theory, the reorganization energy λ can be expressed in terms of the variance $\langle \delta\mathcal{E}^2 \rangle$ as Eq. **116**

$$\lambda = \frac{\langle \delta\mathcal{E}^2 \rangle}{2k_B T}, \qquad \text{Eq. } \mathbf{116}$$

where k_B is the Boltzmann constant. The second approximation relies on the representation of $C_R(t)$ by the standard analytical expression for an undamped classical mechanical harmonic oscillator given in Eq. **117**

$$C_R(t) = \frac{k_B T}{M\Omega^2}\cos\Omega t\,, \qquad \text{Eq. } \mathbf{117}$$

where Ω is the harmonic oscillator frequency and M is the mass.

We make one additional approximation to obtain a remarkably simple, approximate expression for the deuterium kinetic isotope effect (KIE), which is the ratio of the rate constants for hydrogen transfer and deuterium transfer. As will be shown below, the R coordinate term in Eq. **117** is approximately constant on the timescale of the probability flux correlation function decay for the SLO reaction, so we can invoke the approximation that $C_R(t) \approx C_R(0)$. In this case, the R coordinate term in Eq. **117** can be simplified to Eq. **118**

$$F_R(t) \equiv \exp\left\{\alpha_{\mu\nu}^2\left[C_R(0) + C_R(t)\right]\right\} \approx \exp\left\{2\alpha_{\mu\nu}^2 C_R(0)\right\}. \qquad \text{Eq. } \mathbf{118}$$

Using the approximations in Eq. **115-118** , the time integral of the probability flux can be integrated analytically to give the rate expression in Eq. **119**

$$k = \sum_\mu P_\mu \sum_\nu \left|V^{\mathrm{el}} S_{\mu\nu}^{(0)}\right|^2 \exp\left[\frac{2k_B T\alpha_{\mu\nu}^2}{M\Omega^2}\right]\sqrt{\frac{\pi}{\lambda k_B T}}\exp\left[-\frac{\left(\Delta G^0 + \lambda + \Delta\varepsilon_{\mu\nu}\right)^2}{4\lambda k_B T}\right], \qquad \text{Eq. } \mathbf{119}$$

where ΔG^0 is the driving force and $\Delta\varepsilon_{\mu\nu}$ is the difference between the product and reactant vibronic energy levels relative to the ground states. Here we have used the linear response relation $\langle\mathcal{E}\rangle = \Delta G^0 + \lambda$ and the expression for the reorganization energy in Eq. **116** . The derivation of Eq. **119** also assumes that the time correlation functions for the R coordinate and the energy gap (i.e., the reorganization energy) are the same for all vibronic states. This rate expression is similar to the Marcus theory expression for electron transfer except for the R-coordinate factor of $\exp\left[2k_B T\alpha_{\mu\nu}^2 / M\Omega^2\right]$ and the inclusion of the overlap factor in the vibronic coupling.

The rate expression in Eq. **119** leads to a relatively simple expresison for the KIE because only the first two factors depend on the isotope. If we consider only the

nonadiabatic transition between the two ground states, the KIE can be approximated as Eq. **120**

$$\mathrm{KIE} \approx \frac{\left|S_H\right|^2}{\left|S_D\right|^2} \exp\left\{\frac{2k_\mathrm{B}T}{M\Omega^2}\left(\alpha_H^2 - \alpha_D^2\right)\right\}, \qquad \text{Eq. } \mathbf{120}$$

where S_H and S_D are the overlaps of the hydrogen and deuterium wavefunctions, respectively, and α_H and α_D represents the exponential dependence of this overlap on R for hydrogen and deuterium, respectively. Note that the quantity $k_\mathrm{B}T/M\Omega^2 = \left\langle \delta R^2 \right\rangle$ and can be calculated directly from the molecular dynamics simulations. Similarly, the reorganization energy λ given by Eq. **116** and the quantity $\Delta G^0 + \lambda = \left\langle \mathcal{E} \right\rangle$ can also be calculated directly from the molecular dynamics simulations. The simplified expression for the KIE given in Eq. **120** provides insight into the magnitude and temperature dependence of the KIE for the lipoxygenase system. The effects of excited vibronic states can be included by summing over these states in Eq. **119**.

A more quantitatively accurate calculation of the KIE is obtained by including the time-dependence of $C_R(t)$ in the calculation of the rates. In this case, we do not make the approximation given in Eq. **118**. The rate can be calculated by numerically integrating the time integral of the probability flux correlation function using the approximations in Eqs. **115** and **117**. Alternatively, to avoid the numerical integration, we can expand the expression in Eq. **117** in a Taylor series to second order in time and analytically integrate the time integral of the resulting probability flux correlation function. This procedure leads to the rate expression shown in Eq. **121**

$$k = \sum_{\mu} P_{\mu} \sum_{\nu} \left| V^{\mathrm{el}} S_{\mu\nu}^{(0)} \right|^2 \exp\left[\frac{2 k_{\mathrm{B}} T \alpha_{\mu\nu}^2}{M\Omega^2} \right] \sqrt{\frac{\pi}{\left(\lambda + \frac{\hbar^2 \alpha_{\mu\nu}^2}{2M} \right) k_{\mathrm{B}} T}}$$

$$\times \exp\left[- \frac{\left(\Delta G^0 + \lambda + \Delta\varepsilon_{\mu\nu} \right)^2}{4\left(\lambda + \frac{\hbar^2 \alpha_{\mu\nu}^2}{2M} \right) k_{\mathrm{B}} T} \right] \quad . \qquad \text{Eq. } \mathbf{121}$$

This expression is identical to Eq. **119** except that λ is replaced by $\left(\lambda + \hbar^2 \alpha_{\mu\nu}^2 / 2M\right)$ in the two denominators. As a result, all of the factors depend on the isotope, and the expression for the KIE is substantially more complicated than the expression in Eq. **120**. A similar rate expression was derived previously for PCET reactions in this regime.[28]

In order to calculate the rates and KIEs, the overlap of hydrogen and deuterium wavefunctions, S_H and S_D, and the vibronic coupling parameters, α_H and α_D, must be calculated. These quantities can be estimated from one-dimensional nuclear wavefunctions for Morse potentials corresponding to C–H and O–H vibrational modes. The standard Morse expression is given by Eq. **122**

$$E_{\mathrm{XY}} = D_{\mathrm{XY}} \left(\mathrm{e}^{-2\beta_{\mathrm{XY}}\left(R_{\mathrm{XY}} - R_{\mathrm{XY}}^{\mathrm{o}}\right)} - 2\,\mathrm{e}^{-\beta_{\mathrm{XY}}\left(R_{\mathrm{XY}} - R_{\mathrm{XY}}^{\mathrm{o}}\right)} \right) \qquad \text{Eq. } \mathbf{122}$$

The values for D_{CH} and D_{OH} were determined to be 77 and 82 kcal/mol based on the bond dissociation energies.[9, 36, 37] The values for β_{CH} and β_{OH} were determined to be 2.068 and 2.442 Å^{-1} to reproduce the typical experimentally measured C–H and O–H frequencies of 2900 and 3500 cm^{-1}.[38] The values for $R_{\mathrm{CH}}^{\mathrm{o}}$ and $R_{\mathrm{OH}}^{\mathrm{o}}$ were determined to be 1.09 and 0.96 Å from the experimentally measured bond lengths.[38] All of these values are similar to the values used in our previous study.[14] The hydrogen and deuterium vibrational wavefunctions for the Morse potentials are calculated analytically.[39] The overlaps

between the reactant and product wavefunctions are calculated numerically, and the α_H and α_D parameters are calculated with the finite difference method using the relation $\alpha = d \ln S / dR$ for the equilibrium value $\overline{R}$. The overlaps S_H and S_D depend strongly on the R coordinate, but the α_H and α_D parameters depend only weakly on the R coordinate in the vicinity of the equilibrium value. The values of the overlaps and the α_H and α_D parameters can be calculated in this manner for both ground and excited vibrational states. For $\overline{R}$ = 2.87 Å, we found that α_{H} = 22.74 Å^{-1}, α_{D} = 32.84 Å^{-1}, S_{H} = 3.87×10^{-5}, and $S_{\mathrm{D}} = 3.37\times10^{-7}$ for the ground states.

A PCET reaction is vibronically nonadiabatic when the vibronic coupling is significantly less than the thermal energy $k_{\mathrm{B}}T$. Based on the mechanism that the electron is transferring a large distance and based on the small overlaps of the proton vibrational wavefunctions, we expect the vibronic coupling given in Eq. **111** to be well below thermal energy. Thus, this PCET reaction is vibronically nonadiabatic.

Molecular dynamics simulations

We used the 1YGE crystal structure of soybean lipoxygenase-1[10] for the initial coordinates in our simulations. The linoleic acid substrate was inserted into the substrate cavity of the crystal structure using the AutoDock 3.0.5 docking program.[40] The initial conformation of the linoleic acid was chosen based on the lowest energy conformation of 250 different conformations. The starting conformations of the iron cofactor and linoleic acid substrate are depicted in Figure **34**. The protonation states of the residues within the protein were calculated according to the Poisson Boltzmann electrostatics method using the H++ database.[41, 42] Subsequently, we replaced a peripheral water with a sodium cation to neutralize the overall charge of the system. The protein and substrate were centered in a truncated octahedral periodic box with dimensions 139Å x 139Å x 139Å and were solvated with 12772 explicit TIP3P[43-45] water molecules.

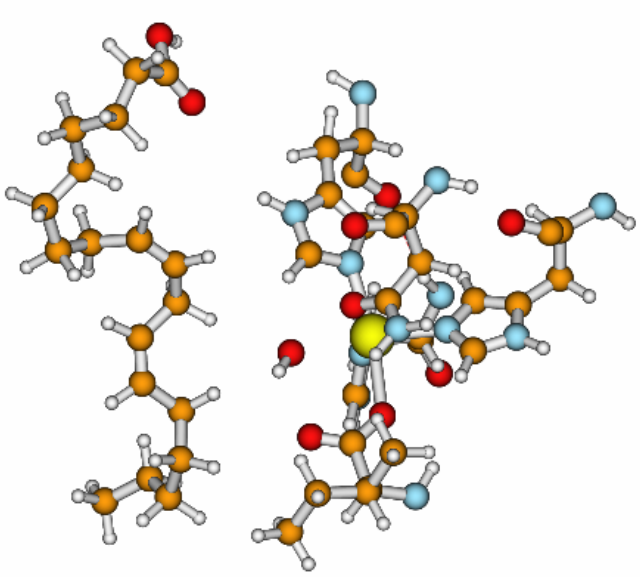

Figure **34**: The iron cofactor of lipoxygenase and the substrate linoleic acid.

The potential energy surface used for the molecular dynamics simulations is based on the AMBER99 forcefield.[45] We used the RESP method[46] to determine the partial charges of the neutral (reactant) and the radical (product) forms of linoleic acid. For this purpose, the structures of the linoleic acid were optimized using density functional theory at the B3LYP/6-31G** level, and the partial atomic charges were calculated at the MP2/6-31G* level. All of these electronic structure calculations were performed with Gaussian03.[47] The Fe–ligand bonds and ligand–Fe–ligand angles in the iron cofactor were represented by harmonic potentials. For the Fe–ligand bonds, the equilibrium distances were set to the distances optimized previously with DFT calculations,[14] and the force constants were obtained from the experimental studies for model iron systems.[48] For the ligand–Fe–ligand angles, the equilibrium angles were set to the octahedral positions of 90 and 180 degrees, and the force constants were set to 125 kcal/mol · rad^2. The Fe–O(842)–H angle was represented by a harmonic potential with the equilibrium angle of 126 degrees and a force constant of 100 kcal/mol · rad^2, similar to the parameters used previously for a Zn–O–H angle.[49] The Fe–O(839)–C angle was represented by a harmonic potential with an equilibrium angle of 128 degrees and a force

constant of 70 kcal/mol · rad^2, similar to the values used previously for an iron transferrin system.[50]

The simulations were performed with a modified version of DLPROTEIN[51, 52] that includes the EVB method. A two-state EVB model for the system was used to calculate the energy gap between the reactant and product states. The transferring electron and proton are localized on the linoleic acid substrate in the reactant and on the iron cofactor in the product. A two-state EVB model is applicable for this system because the intermediate diabatic PCET states, in which only the electron or only the proton has transferred, are much higher in energy than the reactant and product states. The modified AMBER forcefield is used to describe both EVB states. To account for the difference in the zero of energy for the two potential energy surfaces, a constant energy shift Δ is added to the product state potential. As described below, the value of Δ is determined by linear response theory relations.

We emphasize that this solvated enzyme system includes ~52,000 atoms and that all of these atoms are moving in our molecular dynamics simulations. In other words, we are not freezing any part of the system. The classical equations of motion were integrated with the velocity Verlet algorithm[53] on the reactant vibronic surface with a time step of 1 fs. All bond lengths involving hydrogen atoms were constrained with the SHAKE algorithm.[54] The Ewald method[55] was used to treat long-range electrostatic interactions. The NPT simulations were performed with a Hoover thermostat,[56] and the NVT simulations were performed with a Nosé-Hoover thermostat.[57]

The system was carefully equilibrated prior to data collection. To avoid dissociation of the linoleic acid substrate, the distance between the C11 carbon of the linoleic acid and the oxygen atom of the hydroxyl ligand of the iron cofactor was constrained to 3.2Å, which is approximately the sum of the van der Waals radii of carbon and oxygen, during the equilibration procedure. In the first step of equilibration, a minimization of the entire system was performed. In the second step, molecular dynamics simulations were propagated for 50 ps at 100K, 200K and 300K with an NPT ensemble. The NPT ensemble was used to relax the volume of the box and to avoid vacuum bubbles in the solvent. In the third step of the equilibration procedure, the

molecular dynamics simulations were propagated for 100 ps with an NVT ensemble at 300K. The root-mean-square deviation of the backbone of the protein after equilibration was calculated to be 1.48 Å.[58]

A final preparation step was performed after this equilibration procedure. For this step and the data collection, the constraint between the C11 carbon of the linoleic acid and the oxygen from the hydroxyl ligand was released, and a weak harmonic angle restraint was applied to the corresponding C–H–O angle to ensure sampling of the region of phase space relevant to hydrogen abstraction. This angle restraint was represented by an equilibrium angle of 180 degrees and a force constant of 10 kcal/mol · rad^2. The final preparation step was required because we found that the substrate dissociated during the data collection procedure, which requires at least 100 ps of sampling. Therefore, an initial molecular dynamics simulation was propagated for 50 ps at 303 K to provide an estimate of the average distance between the C11 carbon of the linoleic acid and the iron of the cofactor. This distance was subsequently constrained to its average value of 4.4 Å to avoid dissociation of the substrate but still enable the sampling of the proton donor-acceptor distance. This procedure could be viewed as providing an associated reactive complex that would be formed on a much slower time scale than can be sampled with computer simulations.

The first stage of data collection involved molecular dynamics simulations on the reactant vibronic surface with an unconstrained R coordinate (i.e., without a constraint between the C11 carbon of the linoleic acid and the oxygen of the hydroxyl group of the iron cofactor). We sampled the entire system for 100 ps at 303 K. The average proton donor-acceptor distance was determined to be $\overline{R}$ = 2.87 Å. We also calculated the time correlation function of the proton donor-acceptor mode to be $C_R(0) = \langle \delta R^2 \rangle$ = 0.00406 Å^{-2}. Using Eq. **117**, the quantity $M\Omega^2$ was determined directly from this variance, and the mass M was determined from the time dependence of the R coordinate term $F_R(t)$ on the timescale of the probability flux correlation function decay. Note that the mass and frequency of the proton donor-acceptor mode are determined directly and uniquely from the molecular dynamics simulations, thereby avoiding the arbitrary choice of mass and

frequency. We tested for convergence by calculating these quantities for two halves of the molecular dynamics data and found that the average proton donor-acceptor distance differed by less than 0.01 Å and the variance differed by 0.0003 $Å^2$ for the two portions of the data.

The second stage of data collection involved molecular dynamics simulations on the reactant vibronic surface with the proton donor-acceptor distance constrained to the averaged distance determined in the first stage. We sampled the system for 50 ps during this stage. During this stage, we calculated the average energy gap $\langle \mathcal{E}_{\mu\nu} \rangle$ and the time correlation function of the energy gap $C_{\varepsilon}(t)$ to use as input into the rate expression given above. The energy gap between the reactant and product vibronic states was calculated with a two-state EVB model. At each time step, the product energy was calculated by moving the transferring hydrogen H* to the acceptor oxygen in the Fe–O–H plane with an O–H* distance of 0.9572 Å and an H*–O–H angle of 104.5 degrees. The energy gap $\mathcal{E}_{\mu\nu}$ was calculated as the difference between the energies of the reactant and product states, excluding the bonding interactions directly involving the transferring hydrogen because this hydrogen nucleus behaves quantum mechanically. Thus, the energy gap includes both the inner-sphere (i.e., substrate and cofactor) and outer-sphere (i.e., protein) contributions. We tested for convergence by comparing the results for two independent 25 ps molecular dynamics simulations and found that the average energy gap differed by only 2.3 kcal/mol for these two independent simulations.

The overall rate constant is obtained by summing over the contributions from all pairs of reactant and product vibronic states. The probability flux correlation function can be determined for any pair of reactant and product vibronic states by calculating the overlaps and α_{H} and α_{D} parameters for the corresponding vibrational states of the Morse potentials, as well as the relevant vibrational energy level splittings $\Delta\varepsilon_{\mu\nu}$. This procedure is based on the approximation that the time correlation functions for the *R* coordinate and the energy gap (i.e., the reorganization energy) do not change significantly for the different vibronic states. For the SLO reaction, we found that the

rates and KIEs are converged by including contributions from the ground and first excited vibronic states for the reactant and the product.

Results and Discussion

Validation of linear response theory

We test the validity of the linear response approximation for this system by analyzing the energy gap calculations obtained from the molecular dynamics simulations. The energy gap distribution function $P(\mathcal{E})$ is calculated by binning the energy gap values over 100 bins in the range of -20 to -70 kcal/mol. The energy gap distribution function $P(\mathcal{E})$, which is shown in Figure **35a**, resembles a Gaussian distribution with the center at $\mathcal{E} = \langle \mathcal{E} \rangle$ and the width determined by the variance of the energy gap $\langle \delta \mathcal{E}^2 \rangle$. The free energy calculated from the energy gap distribution function is depicted in Figure **35b**. In the linear response regime, the free energy curve is a parabola with minimum $\langle \mathcal{E} \rangle$ and force constant $f_{\text{harm}} = k_B T / \langle \delta \mathcal{E}^2 \rangle$. The corresponding harmonic free energy curve from linear response theory is also depicted in Figure **35b**. The agreement between this harmonic free energy curve and the free energy curve calculated from the molecular dynamics simulations validates the linear response approximation for this system.

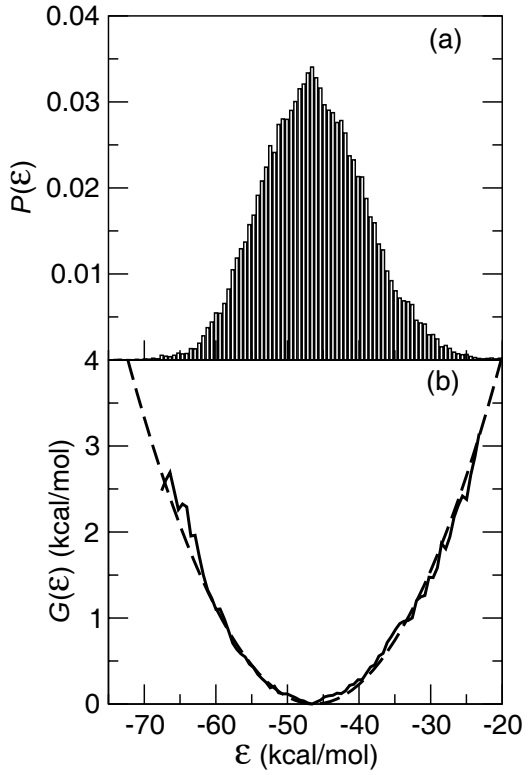

Figure **35**: (a) The energy gap distribution function $P(\mathcal{E})$ and (b) the free energy curve calculated from this distribution function using $G(\mathcal{E}) = -k_{\mathrm{B}}T \ln\left[P(\mathcal{E})\right]$ (solid) and from the linear response approximation of a parabola with minimum $\langle\mathcal{E}\rangle$ and force constant $f_{\mathrm{harm}} = k_B T \big/ \langle \delta\mathcal{E}^2 \rangle$ (dashed).

Within the framework of linear response theory, the reorganization energy can be expressed in terms of the variance $\langle \delta\mathcal{E}^2 \rangle$ according to Eq. **116**, and the average energy gap can be related to the driving force ΔG^0 and the reorganization energy λ as $\langle\mathcal{E}\rangle = \Delta G^0 + \lambda$. Since we have illustrated the validity of linear response for this system, we can use these relations to determine the constant energy shift Δ between the reactant and product state potential energy surfaces. The free energy of reaction ΔG^0 was estimated to be −5.4 kcal/mol for the SLO system based on experimental data.[14] The average energy gap and the variance of the energy gap were calculated from the

molecular dynamics simulations to be $\langle \mathcal{E} \rangle = \Delta - 46.03$ kcal/mol and $\langle \delta \mathcal{E}^2 \rangle = 51.73$ (kcal/mol)^2, respectively. Using the linear response theory relations given above, we determine that $\Delta = 8.4$ kcal/mol. The reorganization energy is calculated from the molecular dynamics simulations to be $\lambda = 43$ kcal/mol.

Time correlation functions for protein and proton donor-acceptor motions

The time correlation functions $C_\varepsilon(t)$ and $C_R(t)$ for the energy gap and *R*, respectively, are calculated from the molecular dynamics simulations described above. These time correlation functions are depicted in Figure **36**. Both time correlation functions decay quickly within 0.5 ps. The normalized spectral densities corresponding to $C_\varepsilon(t)$ and $C_R(t)$, respectively, are shown in Figure **37**. Figure **37a** depicts the spectral density of the energy gap correlation function, which corresponds to the vibrations within the protein. This spectral density exhibits several peaks in the 500 – 1500 cm^{-1} region, corresponding to the C–C and C–N single bond vibrations within the protein. The peak at ~1700 cm^{-1} most likely corresponds to the carbonyl vibrations. Figure **37b** depicts the spectral density of the *R* coordinate vibrational frequency.

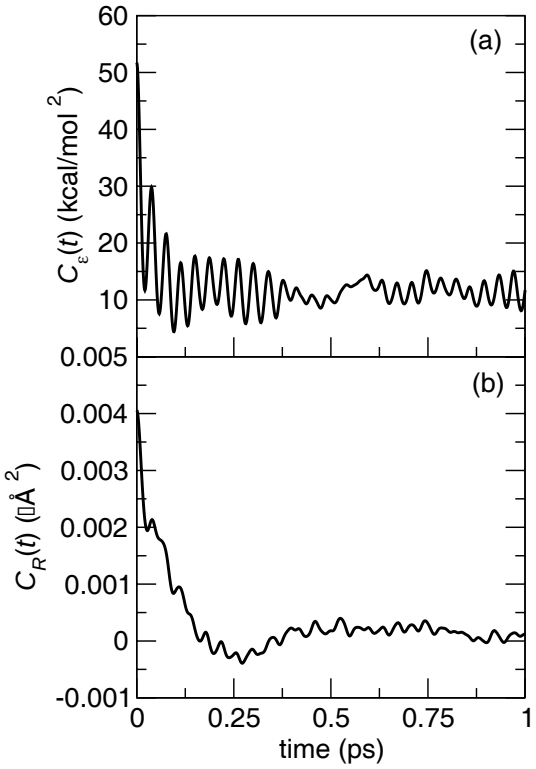

Figure **36**: Time correlation functions of (a) the energy gap and (b) the *R* coordinate.

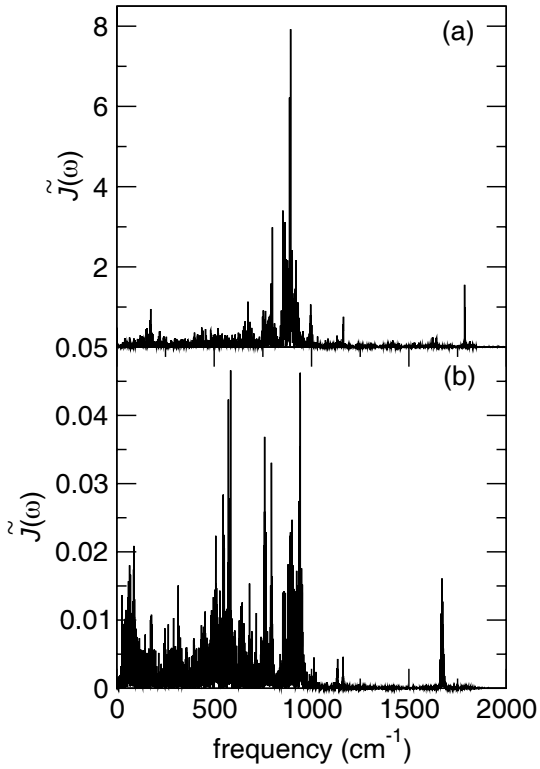

Figure **37**: Normalized spectral density corresponding to (a) $C_{\varepsilon}(t)$ and (b) $C_R(t)$. The normalized spectral density is defined as $\tilde{J}(\omega) = J(\omega) \Big/ \int_0^{\infty} \frac{J(\omega)}{\omega} d\omega$, where the spectral density $J(\omega)$ is calculated from the time correlation function using the relation $C(t) = \frac{8}{\pi\beta} \int_0^{\infty} \frac{J(\omega)}{\omega} \cos(\omega t) d\omega$.

The probability flux correlation function is calculated from Eq. **113** with the time correlation functions obtained from the molecular dynamics simulations. The normalized real part of the probability flux correlation function is depicted in Figure **38a**. The ground state rate constant is calculated by integrating this probability flux correlation function over time. As illustrated in Figure **38a**, the probability flux correlation function decays quickly in ~10 fs. The probability flux correlation function can be broken down into the quantum coherent term, the solvent damping term, and the *R* coordinate term. These components are depicted in Figure **38b**.

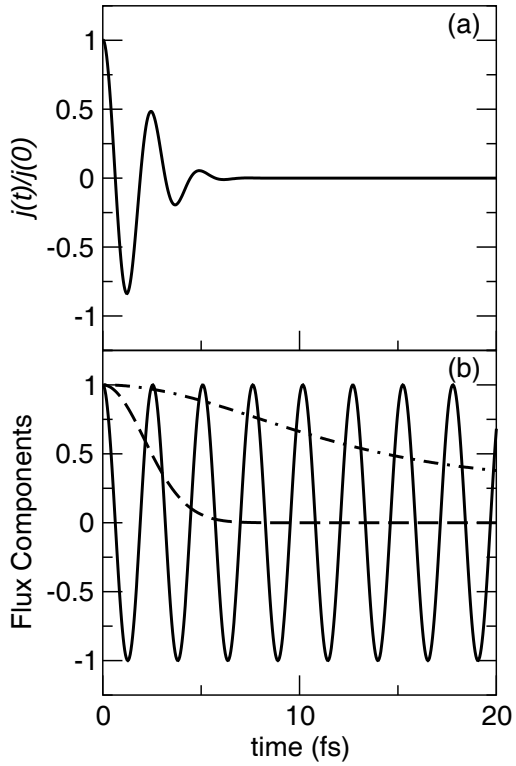

Figure **38**: (a) Time dependence of the real part of the normalized probability flux correlation function given in Eq. **113** and (b) the time dependence of dominant probability flux components calculated from molecular dynamics simulations at 303K. The components include the quantum coherent term $F_Q(t) = \exp\left[\frac{i}{\hbar}\langle\mathcal{E}\rangle t\right]$(solid), the solvent damping term $F_\varepsilon(t)$ defined in Eq. **115** (dashed), and the *R* coordinate term $F_R(t)$ defined in Eq. **118** (dot-dashed).

An analysis of the components comprising the probability flux correlation function provides insight into the roles of the protein and the proton donor-acceptor motions. The quantum coherent term, $F_Q(t)$, is a highly oscillatory function with a period determined by the average energy gap, $\langle\mathcal{E}\rangle$. As indicated by Eq. **115**, the protein/solvent damping term, $F_\varepsilon(t)$, decays on a time scale determined by the energy gap variance $\langle\delta\mathcal{E}^2\rangle$, which is directly related to the reorganization energy through Eq. **116**. Since the protein/solvent damping term decays on a much faster timescale than

the other components of the probability flux correlation function, this term dictates the decay time of the probability flux correlation function. A larger reorganization energy leads to a faster decay of the probability flux correlation function and therefore a slower overall rate. Figure **38b** illustrates that the *R* coordinate term, $F_R(t)$, is relatively constant on the timescale of the decay of the probability flux correlation function. This observation indicates that the dynamics of the *R* coordinate do not impact the time dependence of the probability flux correlation function. The magnitude of $F_R(t)$, however, greatly impacts the magnitude of the probability flux correlation function and therefore the magnitude of the overall rate. According to Eq. **119**, the magnitude of the overall rate is strongly influenced by the variance of the *R* coordinate $\langle \delta R^2 \rangle$, which is related to the frequency of the proton donor-acceptor motion as in Eqs. **117** and **118**, and the parameter α, which represents the dependence of the vibronic coupling on the *R* coordinate as in Eq. **112**.

We also tested two additional approximations invoked to study the temperature dependence of the rates and the KIEs. The first approximation is the short-time approximation, in which only equilibrium fluctuations of the solvent and protein are considered. This approximation is valid when the decay time of the probability flux correlation function is short with respect to the initial decay time of the energy gap correlation function. In this limit, only the initial value of the energy gap correlation function impacts the rate, leading to the simplified protein/solvent damping term given in Eq. **115**. In the second approximation, the *R* coordinate motion is assumed to be harmonic, and the damping effects from the solvent and protein environment are assumed to be negligible on the time scale of the decay of the probability flux correlation function. This approximation leads to the expressions for the *R* coordinate time correlation function given in Eq. **117**. The quantity $M\Omega^2$ was determined directly from the variance $k_B T / M\Omega^2 = \langle \delta R^2 \rangle = 0.00406$ Å^{-2}, and the mass *M* was determined to be *M* = 14 amu from the time dependence of the *R* coordinate term $F_R(t)$ on the timescale of the probability flux correlation function decay. Figure **39** illustrates that both of these approximations are reasonable for the PCET reaction catalyzed by SLO.

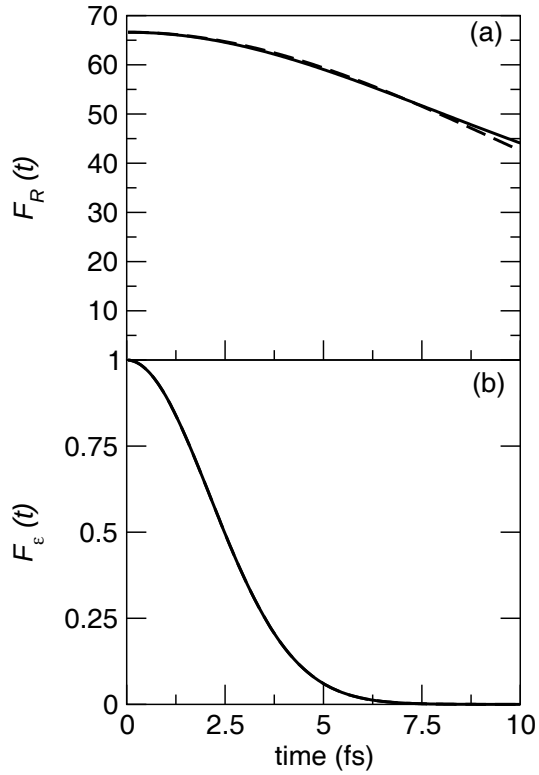

Figure **39**: (a) Comparison of the *R* coordinate term $F_R(t)$ calculated with $C_R(t)$ from classical molecular dynamics simulations (solid) to this term calculated with $C_R(t)$ for an undamped classical harmonic oscillator given in Eq. **117**.(dashed) (b) Comparison of the solvent damping term $F_\varepsilon(t)$ calculated with $C_\varepsilon(t)$ obtained from classical molecular dynamics simulations (solid) to this term calculated with the short-time approximation given in Eq. **115** (dashed). Note that the curves in are virtually indistinguished.

Temperature dependence of the KIEs

We calculated the magnitude and temperature dependence of the KIE using both the simple approximate expression in Eq. **120** and the more quantiatively accurate expression in Eq. **121**. We calculated the average energy gap and the time correlation

functions for the energy gap and the R coordinate from the molecular dynamics simulations at 303 K. The overlaps S_H and S_D and the parameters α_H and α_D were calculated from the hydrogen and deuterium vibrational wavefunctions corresponding to Morse potentials with the donor and acceptor atoms separated by the equilibrium value $\overline{R} = 2.87\,\text{Å}$ determined from the molecular dynamics simulations. The Morse potentials and the corresponding ground state hydrogen and deuterium vibrational wavefunctions are depicted in Figure **40**. Since the KIE is the ratio of two rates, the KIE is independent of the constant electronic coupling parameter V^{el}, and we did not need to determine the value of this parameter. For these calculations, we did not fit any parameters directly to the experimental kinetic data.

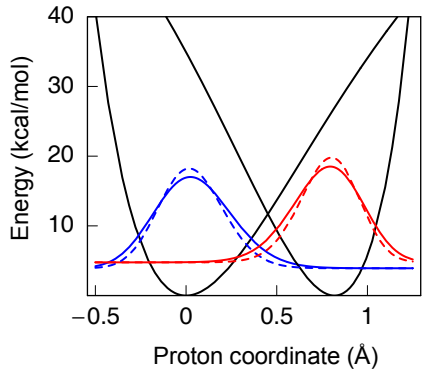

Figure **40**: Morse potentials and hydrogen (solid) and deuterium (dashed) wavefunctions for the reactant (blue) and product (red) states.

The temperature dependence of the KIE using the simple approximate expression in Eq. **120** is depicted in Figure **41**. The quantity $M\Omega^2$ is determined from the R coordinate variance $C_R(0) = \langle \delta R^2 \rangle$ obtained from the molecular dynamics simulations. Eq. **120** indicates that the temperature dependence of the KIE is determined mainly by the R coordinate variance and the parameters α_H and α_D. The ratio of the overlaps of hydrogen and deuterium strongly impacts the magnitude of the KIE but does not affect the temperature dependence. This simple approximate expression leads to qualitative agreement with the experimentally observed temperature dependence of the KIE but overestimates the magnitude of the KIE. We include the effects of the excited vibronic

states using the rate expression in Eq. **119**. For hydrogen, the contribution from the transition between the ground reactant and product states was 98% at 303 K. For deuterium, the contribution from the transition between the ground states was 70%, and the contribution from the transition between the ground reactant state and the first excited product state was 18% at 303 K. As shown in Figure **41**, including the excited states does not significantly alter the temperature dependence of the KIE but decreases the magnitude of the KIE by ~15%.

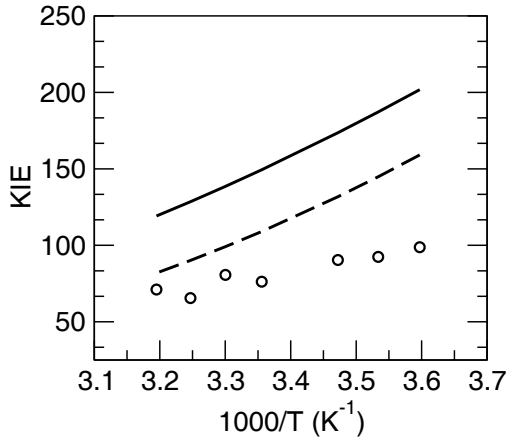

Figure **41**: Temperature dependence of the KIE obtained with the simple approximate expression in Eq. **120** (solid line) and the analogous expression including the excited vibronic states (dashed line). The experimental data are depicted with circles.

Figure **42** depicts the temperature dependence of the KIE using the more quantitatively accurate expression in Eq. **121**, as well as the numerical integration of the probability flux correlation function given in Eq. **113** in conjunction with the approximations given in Eq. **115** and Eq. **117**. Both of these approaches include the time dependence of the *R* coordinate time correlation function. The results from these two approaches are virtually identical and agree well with the experimentally observed magnitude and temperature dependence of the KIE. We emphasize that the magnitude and temperature dependence of the KIE are obtained without fitting any parameters directly to the kinetic data. This agreement between the theoretical and experimental KIEs suggests that this theoretical formulation contains the essential physical elements needed to describe PCET reactions.

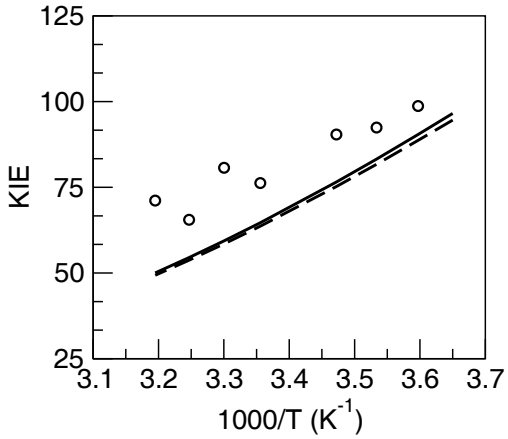

Figure **42**: Temperature dependence of the KIE obtained with the rate expression in Eq. **121** (solid line) and by numerical integration of the probability flux correlation function given in Eq. **113** in conjunction with the approximations in Eq. **115** and Eq. **117**. The solid and dashed line are virtually identical. The experimental data are depicted with circles.

Conclusions

In this paper, we examined the dynamical behavior and the temperature dependence of the rates and kinetic isotope effects for the PCET reaction catalyzed by SLO. Our calculations were based on a vibronically nonadiabatic formulation for PCET reactions in solution and proteins. This formulation includes the quantum mechanical effects of the active electrons and the transferring proton, as well as the motions of all atoms in the complete solvated enzyme system. The rate is represented by the time integral of a probability flux correlation function that depends on the vibronic coupling, the average of the energy gap and *R* coordinate, and the time correlation functions of the energy gap and *R* coordinate. The vibronic couplings can be estimated to within a constant factor by calculating the overlaps between reactant and product hydrogen vibrational wavefunctions for model systems, and the other quantities can be calculated from classical molecular dynamics simulations of the entire system.

We tested the underlying assumptions of this vibronically nonadiabatic formulation for an enzymatic system and investigated the dynamical behavior of the protein, substrate, and cofactor. Our estimates of the contributions to the vibronic couplings for this PCET reaction indicate that this reaction is vibronically nonadiabatic. Moreover, our molecular dynamics simulations of the entire solvated enzyme system validate the linear response approximation for this PCET reaction and provide an estimate of 43 kcal/mol for the total reorganization energy. We found that the dynamical behavior (i.e., the time dependence) of the probability flux correlation function is dominated by the protein/solvent reorganization energy and is not significantly influenced by the proton donor-acceptor frequency or the vibronic coupling. The magnitude of the overall rate, however, is strongly influenced by the frequency of the proton donor-acceptor motion, the magnitude and distance dependence of the vibronic coupling, and the protein/solvent reorganization energy.

These calculations reproduced the experimentally observed magnitude and temperature dependence of the KIE for the SLO enzyme reaction without fitting any parameters directly to the experimental kinetic data. The temperature dependence of the KIEs is determined mainly by the proton donor-acceptor frequency, which can be calculated from the R coordinate variance in the molecular dynamics simulations, and the distance dependence of the vibronic couplings for hydrogen and deuterium, which can be calculated from the vibrational wavefunctions for model systems. The ratio of the overlaps of the hydrogen and deuterium vibrational wavefunctions strongly impacts the magnitude of the KIE but does not significantly influence the temperature dependence. These trends are summarized in the relatively simple, approximate expression for the KIE given in Eq. **120**.

These calculations provide insight into the fundamental physical principles underlying the PCET reaction catalyzed by SLO. Future studies will focus on the impact of mutations on the dynamical behavior of the protein, substrate, and cofactor, and on the temperature dependence of the rates and KIEs for this reaction. This general theoretical formulation is applicable to a broad range of other vibronically nonadiabatic enzyme reactions.

References

1. Samuelsson, B.; Dahlen, S.-E.; Lindgren, J. A.; Rouzer, C. A.; Serhan, C. N. *Science* **1987,** *237*, 1171-76.
2. Steele, V. E.; Holmes, C. A.; Hawk, E. T.; Kopelovich, L.; Lubet, R. A.; Crowell, J. A.; Sigman, C. C.; Kelloff, G. J. *Cancer, Epidemiology, Biomarkers, & Prevention* **1999,** *8*, 467-483.
3. Rioux, N.; Castonguay, A. *Carcinogenesis* **1998,** *19*, 1393-1400.
4. Nie, D.; Hillman, G. G.; Geddes, T.; Tang, K.; Pierson, C.; Grignon, D. J.; Honn, K. V. *Cancer Research* **1998,** *58*, 4047-4051.
5. Ghosh, J.; Myers, C. E. *Proc. Natl. Acad. Sci. USA* **1998,** *95*, 13182-13187.
6. Lewis, E. R.; Johansen, E.; Holman, T. R. *Journal of the American Chemical Society* **1999,** *121*, 1395-1396.
7. Segraves, E. N.; Holman, T. R. *Biochemistry* **2003,** *42*, 5236-5243.
8. Rickert, K. W.; Klinman, J. P. *Biochemistry* **1999,** *38*, 12218-12228.
9. Knapp, M. J.; Rickert, K. W.; Klinman, J. P. *Journal of the American Chemical Society* **2002,** *124*, 3865-3874.
10. Minor, W.; Steczko, J.; Stec, B.; Otwinowski, Z.; Bolin, J. T.; Walter, R.; Axelrod, B. *Biochemistry* **1996,** *35*, 10687-10701.
11. Tomchick, D. R.; Phan, P.; Cymborowski, M.; Minor, W.; Holman, T. R. *Biochemistry* **2001,** *40*, 7509-7517.
12. Knapp, M. J.; Seebeck, F. P.; Klinman, J. P. *Journal of the American Chemical Society* **2001,** *123*, 2931-2932.
13. Lehnert, N.; Solomon, E. I. *J. Biol. Inorg. Chem.* **2003,** *8*, 294-305.
14. Hatcher, E.; Soudackov, A. V.; Hammes-Schiffer, S. *Journal of the American Chemical Society* **2004,** *126*, 5763-5775.
15. Glickman, M. H.; Wiseman, J. S.; Klinman, J. P. *Journal of the American Chemical Society* **1994,** *116*, 793-794.
16. Hwang, C.-C.; Grissom, C. B. *Journal of the American Chemical Society* **1994,** *116*, 795-796.
17. Jonsson, T.; Glickman, M. H.; Sun, S.; Klinman, J. P. *Journal of the American Chemical Society* **1996,** *118*, 10319-10320.
18. Borowski, T.; Krol, M.; Chruszcz, M.; Broclawik, E. *Journal of Physical Chemistry B* **2001,** *105*, 12212-12220.
19. Borowski, T.; Broclawik, E. *Journal of Physical Chemistry B* **2003,** *107*, 4639-4646.
20. Tejero, I.; Eriksson, L. A.; Gonzalez-Lafont, A.; Marquet, J.; Lluch, J. M. *Journal of Physical Chemistry B* **2004,** *108*, 13831-13838.

21. Kuznetsov, A. M.; Ulstrup, J. *Canadian Journal of Chemistry* **1999,** *77*, 1085-1096.

22. Tresadern, G.; McNamara, J. P.; Mohr, M.; Wang, H.; Burton, N. A.; Hillier, I. H. *Chemical Physics Letters* **2002,** *358*, 489-494.

23. Knapp, M. J.; Klinman, J. P. *European Journal of Biochemistry* **2002,** *269*, 3113-3121.

24. Mincer, J. S.; Schwartz, S. D. *Journal of Chemical Physics* **2004,** *120*, 7755-7760.

25. Olsson, M. H. M.; Siegbahn, P. E. M.; Warshel, A. *Journal of the American Chemical Society* **2004,** *126*, 2820-2828.

26. Olsson, M. H. M.; Siegbahn, P. E. M.; Warshel, A. *Journal of Biological Inorganic Chemistry* **2004,** *9*, 96-99.

27. Siebrand, W.; Smedarchina, Z. *Journal of Physical Chemistry B* **2004,** *108*, 4185-4195.

28. Soudackov, A.; Hatcher, E.; Hammes-Schiffer, S. *Journal of Chemical Physics* **2005,** *122*, 014505.

29. Hatcher, E.; Soudackov, A.; Hammes-Schiffer, S. *Chemical Physics* **2005,** *319*, 93-100.

30. Hatcher, E.; Soudackov, A.; Hammes-Schiffer, S. *Journal of Physical Chemistry B* **2005,** *109*, 18565-18574.

31. Borgis, D.; Lee, S.; Hynes, J. T. *Chemical Physics Letters* **1989,** *162*, 19-26.

32. Borgis, D.; Hynes, J. T. *Journal of Chemical Physics* **1991,** *94*, 3619-3628.

33. Suarez, A.; Silbey, R. *Journal of Chemical Physics* **1991,** *94*, 4809-4816.

34. Trakhtenberg, L. I.; Klochikhin, V. L.; Pshezhetsky, S. Y. *Chemical Physics* **1982,** *69*, 121-134.

35. Kiefer, P. M., Hynes, J. T. *J. Phys. Chem. A* **2004,** *108*, 11793-11808.

36. Mayer, J. M. *Accounts of Chemical Research* **1998,** *31*, 441-450.

37. Clark, K. B.; Culshaw, P. N.; Griller, D.; Lossing, F. P.; Simoes, J. A. M.; Walton, J. C. *Journal of Organic Chemistry* **1991,** *56*, 5535-5539.

38. Warshel, A., *Computer Modeling of Chemical Reactions in Enzymes and Solutions*. John Wiley & Sons, Inc.: New York, 1991.

39. Dahl, J. P.; Springborg, M. *Journal of Chemical Physics* **1987,** *88*, 4535.

40. Morris, G. M.; Goodsell, D. S.; Halliday, R. S.; Huey, R.; Hart, W. E.; Belew, R. K.; Olson, A. J. *Journal of Computational Chemistry* **1998,** *19*, 1639-1662.

41. Bashford, D., Karplus, M. *Biochemistry* **1990,** *29*, 10219--10225.

42. Gordon, J. C., Myers, J. B., Folta, T., Shoja, V., Heath, L. S., Onufriev, A. *Nucleic Acids Res.* **2005,** *33*.

43. Jorgensen, W. L. *Journal of the American Chemical Society* **1981,** *103*, 335.

44. Jorgensen, W. L.; Chandreskhar, J.; Madura, J. D.; Impey, R. W.; Klein, M. L. *Journal of Chemical Physics* **1982,** *79*, 926-935.

45. Cornell, W. D.; Cieplak, P.; Bayly, C. I.; Gould, I. R.; Merz, K. M., Jr.; Ferguson, D. M.; Spellmeyer, D. C.; Fox, T.; Caldwell, J. W.; Kollman, P. A. *Journal of the American Chemical Society* **1995,** *117*, 5179-5197.

46. Bayly, C., Cieplak, P., Cornell, W., Kollman, P. A. *J. Phys. Chem.* **1993,** *97*, 10269-10280.

47. Frisch, M. J.; Trucks, G. W.; Schlegel, H. B.; Scuseria, G. E.; Robb, M. A.; Cheeseman, J. R.; Montgomery, J. A., Jr.; Vreven, T.; Kudin, K. N.; Burant, J. C.; Millam, J. M.; Iyengar, S. S.; Tomasi, J.; Barone, V.; Mennucci, B.; Cossi, M.; Scalmani, G.; Rega, N.; Petersson, G. A.; Nakatsuji, H.; Hada, M.; Ehara, M.; Toyota, K.; Fukuda, R.; Hasegawa, J.; Ishida, M.; Nakajima, T.; Honda, Y.; Kitao, O.; Nakai, H.; Klene, M.; Li, X.; Knox, J. E.; Hratchian, H. P.; Cross, J. B.; Adamo, C.; Jaramillo, J.; Gomperts, R.; Stratmann, R. E.; Yazyev, O.; Austin, A. J.; Cammi, R.; Pomelli, C.; Ochterski, J. W.; Ayala, P. Y.; Morokuma, K.; Voth, G. A.; Salvador, P.; Dannenberg, J. J.; Zakrzewski, V. G.; Dapprich, S.; Daniels, A. D.; Strain, M. C.; Farkas, O.; Malick, D. K.; Rabuck, A. D.; Raghavachari, K.; Foresman, J. B.; Ortiz, J. V.; Cui, Q.; Baboul, A. G.; Clifford, S.; Cioslowski, J.; Stefanov, B. B.; Liu, G.; Liashenko, A.; Piskorz, P.; Komaromi, I.; Martin, R. L.; Fox, D. J.; Keith, T.; Al-Laham, M. A.; Peng, C. Y.; Nanayakkara, A.; Challacombe, M.; Gill, P. M. W.; Johnson, B.; Chen, W.; Wong, M. W.; Gonzalez, C.; Pople, J. A. *Gaussian03*, revision C.03; Gaussian, Inc.: Pittsburgh, PA, 2003.

48. Zhou, Z.; Khan, S. U. M. *Journal of Physical Chemistry* **1989,** *93*, 5292-5295.

49. Hoops, S. C., Anderson, K. W., Merz, K. M. *J. Am. Chem. Soc.* **1991,** *113*, 8262-8270.

50. Lin, W., Welsh, W. J., Harris, W. R. *Inorg. Chem.* **1994,** *33*, 884-890.

51. Melchionna, S., Cozzini, S. *DLPROTEIN*, 2.1; Cambridge, UK.

52. Smith, W.; Forester, T. R. *DL_POLY_2.14*, CCLRC: Daresbury Laboratory, Warrington, England, 2003.

53. Verlet, L. *Physical Review* **1967,** *159*, 98-103.

54. Ryckaert, J. P.; Ciccotti, G.; Berendsen, H. J. C. *Journal of Computational Physics* **1977,** *23*, 327.

55. Ewald, P. P. *Ann. Phys.* **1921,** *64*, 253-287.

56. Hoover, W. G. *Physical Review A* **1985,** *31*, 1695-7.

57. Nose, S. *Molecular Physics* **1984,** *52*, 255-68.

58. Humphrey, W., Dalke, A., Schulten, K. *Journal of Molecular Graphics* **1996,** *14*, 33-38.

Chapter 7

Summary and Conclusions

Proton-coupled electron transfer (PCET) reactions are the simultaneous transfer of an electron and a proton. These types of reactions occur in many chemical and biological systems such as lipoxygenase. The proton-coupled electron transfer reaction in soybean lipoxygenase-1 is extraordinary because the experimentally measured kinetic isotope effect was determined to be unusually large.[1] In addition, a weak temperature dependence of the rates and kinetic isotope effects was seen. The proton donor-acceptor vibrational mode is thought to play a significant role in this reaction.

The PCET reaction in soybean lipoxygenase was modeled using a multistate continuum theory developed in the Hammes-Schiffer group. The proton donor-acceptor vibrational mode was included using a classical and quantum representation. The temperature dependence of the rates and kinetic isotope effects were reproduced using this formulation in both the classical and quantum regimes of the proton donor-acceptor mode. The weak temperature dependences of the rates were due to the relatively small free energy barrier, which was determined by the balance between the free energy and the reorganization energy of the system. The unusually large kinetic isotope effect of 81 was determined to be due to the small overlap of the reactant and product vibrational wavefunctions, as well as the dominance of the ground vibronic states.

The proton donor-acceptor vibrational mode was examined for this system. Analysis of this mode showed that the distance that had the highest contribution to the rate was 2.7Å. This dominant distance was determined by a balance between the coupling of the reactant and product vibronic states and the Boltzmann probability of the distances. Furthermore, this distance was much smaller than the equilibrium distance of the proton donor and acceptor. The temperature dependence of the rates and kinetic isotope effects were reproduced with the proton donor-acceptor distance fixed to the dominant distance. Therefore, the proton donor-acceptor vibrational mode is important

in facilitating the PCET reaction in soybean lipoxygenase by allowing the proton donor and acceptor to get to distances smaller than the equilibrium distance.

Because the proton donor-acceptor vibrational mode plays an important role in the PCET reactions, the Hammes-Schiffer group developed a formulation that treats this vibrational mode dynamically.[2] This formulation is similar to the formulation that Borgis and Hynes derived for proton transfer systems.[3] A dynamical nonadiabatic rate expression was derived. This theory accounts for the dynamical correlation between the vibrational mode and the solvent modes. In this formulation, the solvent is treated explicitly, and a probability flux correlation function is calculated from quantities obtained from molecular dynamics simulations performed on the reactant surface. The PCET rate is calculated by integrating the probability flux correlation function over time.

Molecular dynamics simulations were performed with model PCET systems to calculate the probability flux correlation function. The solvent damping term, which is a function of the energy gap, governs the decay of the probability flux correlation function. Therefore, the time dependence of the probability flux correlation function is determined by solvent motion. The proton donor-acceptor term (i.e. the *R*-coordinate term) in the flux expression does not decay on the timescale of the probability flux decay. Therefore, the *R*-coordinate term does not affect the time dependence of the probability flux correlation function. Although the proton donor-acceptor vibrational mode does not affect the time dependence of the flux, the frequency of this mode affects the magnitude of the rate. As the proton donor-acceptor vibrational frequency decreases, the rate increases because the lower frequency vibrational mode can sample smaller distances, which leads to larger overlap between vibrational wavefunction which, in turn leads to a larger coupling and therefore a larger rate.

Calculating the dynamical nonadiabatic rate constant numerically from molecular dynamics can be fairly tedious. Therefore, a closed analytical dynamical nonadiabatic rate expression was also developed for PCET reactions. This expression is similar to the expression derived by Borgis and Hynes for nonadiabatic proton transfer reactions.[3] In this expression two assumptions are made; a short-time approximation for the solvent and an undamped quantum harmonic oscillator approximation for the proton donor-acceptor

mode. The validity of these approximations was tested using a PCET model system. The short-time approximation for the solvent was shown to be valid for PCET systems because the decay of the energy gap time correlation function occurs on a longer timescale than the decay of the probability flux correlation function, and so only the initial value of the energy gap correlation function is important for the reaction. Representing the proton donor-acceptor vibrational mode as an undamped quantum harmonic oscillator was also a good approximation because the solvent damping effects on the proton donor-acceptor mode are negligible on the timescale of the probability flux decay. Since all of the approximations made for the analytical expression were tested and determined to be valid, the closed analytical expression can be used for PCET systems.

The dynamical nonadiabatic rate expression was applied to the PCET reaction in soybean lipoxygenase. Molecular dynamics simulations of the entire solvated protein were performed in order to calculate the input quantities necessary for the dynamical rate expression. The reorganization energy was also calculated for the entire system from molecular dynamics simulations. The dynamical behavior of the PCET reaction in soybean lipoxygenase was similar to that of the PCET reaction in model systems. Using the rate expression, the temperature dependence of the kinetic isotope effect was examined. The physical basis for the magnitude and temperature dependence of the KIE in soybean lipoxygenase was elucidated using the dynamical PCET nonadiabatic rate expression.

References

(1) Knapp, M. J.; Rickert, K. W.; Klinman, J. P. *Journal of the American Chemical Society* **2002**, *124*, 3865.

(2) Soudackov, A. V.; Hatcher, E.; Hammes-Schiffer, S. *Journal of Chemical Physics* **2005**, *122*, 014505.

(3) Borgis, D.; Hynes, J. T. *Journal of Chemical Physics* **1991**, *94*, 3619.

Appendix A

Thermochemical Calculations of the ET, PT and PCET reactions in Soybean Lipoxygenase

This appendix outlines the method for estimating the experimentally determined driving forces (i.e., reaction free energies) for ET, PT, and PCET.

Electron Transfer

The electron transfer reaction from linoleic acid to the iron complex is given in Eq. **A.1**

$$CH + HO\text{-}Fe(III) \rightarrow CH^{+} + HO\text{-}Fe(II) \qquad \text{Eq. } \mathbf{A.1}$$

Eq. **A.1** is the sum of Eq. **A.2** and Eq. **A.3** :

$$CH \rightarrow CH^{+} + e^{-} \qquad \text{Eq. } \mathbf{A.2}$$

$$HO\text{-}Fe(III) + e^{-} \rightarrow HO\text{-}Fe(II) \qquad \text{Eq. } \mathbf{A.3}$$

The reduction potential for Eq. **A.2** is E^{o}=2.7 V (vs NHE) for arachidonic acid in acetonitrile.[49] We estimate that the potential will be lower in water by approximately 0.4 V,[50] leading to E^{o}=2.3 V (vs NHE) in water. Equation (Eq. **A.3**) is the sum of Eq. **A.4** and Eq. **A.5**:

$$HO\text{-}Fe(III) + e^{-} + H^{+} \rightarrow H_2O\text{-}Fe(II) \qquad \text{Eq. } \mathbf{A.4}$$

$$H_2O\text{-}Fe(II) \rightarrow HO\text{-}Fe(II) + H^+ \qquad \text{Eq. } \mathbf{A.5}$$

The reduction potential for Eq. **A.4** in SLO1 is E^o=0.6 V at pH=8,[51] leading to E^o= 0.6+ 0.059(8) V = 1.1 V at pH=0. The pK_a for H_2O-Fe(II) in SLO1 has been determined to be ≥ 11.5.[2] Using a pK_a of 11.5, ΔG^o = 1.368 pK_a kcal/mol = 15.73 kcal/mol. Therefore, the overall free energy of the reaction in Eq. A1 is estimated to be ΔG^o = [–23.061(–2.3 + 1.1) + 15.73] kcal/mol = 43 kcal/mol.

Proton Transfer

The proton transfer reaction from linoleic acid to the hydroxide ligand on iron in SLO1 is given in Eq. **A.6**

$$CH + [HO\text{-}Fe(III)]^{2+} \rightarrow C^- + [H_2O\text{-}Fe(III)]^{3+} \qquad \text{Eq. } \mathbf{A.6}$$

Eq. **A.6** is the sum of Eq. **A.7** and Eq. **A.8**:

$$CH \rightarrow C^- + H^+ \qquad \text{Eq. } \mathbf{A.7}$$

$$[HO\text{-}Fe(III)]^{2+} + H^+ \rightarrow [H_2O\text{-}Fe(III)]^{3+} \qquad \text{Eq. } \mathbf{A.8}$$

The free energy of the reaction in Eq. **A.7** for 1,4 pentadiene in DMSO is estimated to be 43 kcal/mol (where the enthalpy was measured to be 40 kcal/mol and the entropy contribution is approximated as 3 kcal/mol).[52] Estimating a decrease in the pK_a of ≈3 units in water relative to DMSO,[53-55] the free energy of the reaction in Eq. **A.7** for linoleic acid in water is estimated to be ΔG^o = 39 kcal/mol. The pK_a for H_2O-Fe(III) in SLO1 has been determined to be < 6.[56] Using a pK_a of 5, ΔG^o = –1.368 pK_a kcal/mol =

−6.84 kcal/mol for the reaction in Eq. **A.8**. Therefore, the overall free energy of the reaction in Eq. **A.6** is estimated to be ΔG^o = [39 – 6.84] kcal/mol = 32 kcal/mol.

PCET

The PCET reaction from linoleic acid to the iron complex in SLO1 is given in Eq. **A.9.**

$$CH + HO\text{-}Fe(III) \rightarrow C\bullet + Fe(II)\text{-}OH_2 \qquad \text{Eq. } \mathbf{A.9}$$

Eq. **A.9** is the sum of Eq. **A.10** and Eq. **A.11**:

$$Fe(III)\text{-}OH + H\bullet \rightarrow Fe(II)\text{-}OH_2 \qquad \text{Eq. } \mathbf{A.10}$$

$$CH \rightarrow C\bullet(aq) + H\bullet \qquad \text{Eq. } \mathbf{A.11}$$

Based on the reduction potential[51] of Eq. **A.4** and the conversion to an aqueous bond enthalpy,[57] the free energy change associated with Eq. **A.10** is estimated to be ΔG^o = –82 kcal/mol.[12] The bond strength of 1,4 pentadiene is 76.6 kcal/mol,[58] and assuming negligible entropy change upon reaction, ΔG^o = 76.6 kcal/mol for the reaction in Eq. **A.11**. Therefore, the overall free energy of the reaction in Eq. **A.9** is estimated to be ΔG^o = [−82 + 76.6] kcal/mol = –5.4 kcal/mol.

Appendix B

Hybrid EVB-LEPS Potential

This appendix presents the hybrid EVB-LEPS potential for a linear model PCET system. The diagonal matrix elements of the gas phase Hamiltonian in the nonorthogonal VB basis are given by the following expressions in Eq. **B.1**.

$$\begin{aligned}
\left(h_o\right)_{1a,1a} &= U_a^{\mathrm{LEPS}}\left(r_p,R\right)+U_1^{\mathrm{harm}}\left(R\right)\\
\left(h_o\right)_{1b,1b} &= U_b^{\mathrm{LEPS}}\left(r_p,R\right)+U_1^{\mathrm{harm}}\left(R\right)+\Delta E_{1b}\\
\left(h_o\right)_{2a,2a} &= U_a^{\mathrm{LEPS}}\left(r_p,R\right)+U_2^{\mathrm{harm}}\left(R\right)+\Delta E_{2a}\\
\left(h_o\right)_{2b,2b} &= U_b^{\mathrm{LEPS}}\left(r_p,R\right)+U_2^{\mathrm{harm}}\left(R\right)+\Delta E_{2b}
\end{aligned} \qquad \text{Eq. } \mathbf{B.1}$$

The proton interface is described with a LEPS potential.[53-55] The corresponding diabatic LEPS potentials are expressed in terms of the Coulomb (Q) and exchange (J) integrals for bonded pairs shown in Eq. **B.2**

$$\begin{aligned}
U_a^{\mathrm{LEPS}}\left(r_p,R\right) &= Q_{\mathrm{D_pH}}+Q_{\mathrm{A_pH}}-\frac{1}{2}J_{\mathrm{A_pH}}+J_{\mathrm{D_pH}}\\
U_b^{\mathrm{LEPS}}\left(r_p,R\right) &= Q_{\mathrm{D_pH}}+Q_{\mathrm{A_pH}}-\frac{1}{2}J_{\mathrm{D_pH}}+J_{\mathrm{A_pH}}
\end{aligned} \qquad \text{Eq. } \mathbf{B.2}$$

where the *a* and *b* subscripts designate the states with the proton bonded to the donor and acceptor, respectively. The Coulomb and exchange integrals are expressed in terms of the energies of singlet and triplet states for bonded pairs given in Eq. **B.3**

$$\begin{aligned}
Q_{\mathrm{XY}} &= \frac{{}^1E_{\mathrm{XY}}\left(1+k_{\mathrm{XY}}\right)+{}^3E_{\mathrm{XY}}\left(1-k_{\mathrm{XY}}\right)}{2\left(1+k_{\mathrm{XY}}\right)}\\
J_{\mathrm{XY}} &= \frac{{}^1E_{\mathrm{XY}}\left(1+k_{\mathrm{XY}}\right)-{}^3E_{\mathrm{XY}}\left(1-k_{\mathrm{XY}}\right)}{2\left(1+k_{\mathrm{XY}}\right)}
\end{aligned} \qquad \text{Eq. } \mathbf{B.3}$$

which are parameterized using the Morse and anti-Morse potentials given in Eq. **B.4**

$$
\begin{aligned}
{}^{1}E_{\mathrm{XY}} &= D_{\mathrm{XY}}\left(\mathrm{e}^{-2\beta_{\mathrm{XY}}\left(R_{\mathrm{XY}}-R_{\mathrm{XY}}^{\mathrm{o}}\right)}-2\,\mathrm{e}^{-\beta_{\mathrm{XY}}\left(R_{\mathrm{XY}}-R_{\mathrm{XY}}^{\mathrm{o}}\right)}\right) \\
{}^{3}E_{\mathrm{XY}} &= \frac{1}{2}D_{\mathrm{XY}}\left(\mathrm{e}^{-2\beta_{\mathrm{XY}}\left(R_{\mathrm{XY}}-R_{\mathrm{XY}}^{\mathrm{o}}\right)}+2\,\mathrm{e}^{-\beta_{\mathrm{XY}}\left(R_{\mathrm{XY}}-R_{\mathrm{XY}}^{\mathrm{o}}\right)}\right)
\end{aligned}
\qquad \text{Eq. } \mathbf{B.4}
$$

For simplicity, the scaling Sato parameters k_{XY} were set to 0.5 for all pairs of atoms for all models. The harmonic potentials for the *R*-mode, shown in Eq. **B.5** , in ET states 1 and 2 differ from each other only by different equilibrium values,

$$
U_i^{\mathrm{harm}}\left(R\right)=\frac{1}{2}M\Omega_{\mathrm{DA}}^{2}(R-R_i^{0})^{2} \qquad \text{Eq. } \mathbf{B.5}
$$

where M and Ω_{DA} are the reduced mass and frequency for the *R*-mode, respectively. The off-diagonal elements, given in Eq. **B.6** , in the non-orthogonal basis are approximated by constant terms

$$
\begin{aligned}
\left(h_{\mathrm{o}}\right)_{1a,1b} &= \left(h_{\mathrm{o}}\right)_{2a,2b} = V^{\mathrm{PT}} \\
\left(h_{\mathrm{o}}\right)_{1a,2a} &= \left(h_{\mathrm{o}}\right)_{1b,2b} = V^{\mathrm{ET}} \\
\left(h_{\mathrm{o}}\right)_{1a,2b} &= \left(h_{\mathrm{o}}\right)_{1b,2a} = V^{\mathrm{ET}}\sigma
\end{aligned}
\qquad \text{Eq. } \mathbf{B.6}
$$

where V^{PT} is the PT electronic coupling and V^{ET} is the ET electronic coupling. The overlap integral σ is set to 0.5, as in the standard two-state LEPS model for triatomic collinear systems. The total overlap integral matrix **S** and the gas-phase Hamiltonian $\mathbf{h}_0^{\lambda}$ in a symmetrically orthogonalized basis are given by Eq. **B.7** and Eq. **B.8** , respectively.

$$\mathbf{S} = \begin{bmatrix} 1 & \sigma & 0 & 0 \\ \sigma & 1 & 0 & 0 \\ 0 & 0 & 1 & \sigma \\ 0 & 0 & \sigma & 1 \end{bmatrix} \qquad \text{Eq. } \mathbf{B.7}$$

$$\mathbf{h}_0^{\lambda} = \mathbf{S}^{-\frac{\mathbf{1}}{\mathbf{2}}}\mathbf{h}_0\mathbf{S}^{-\frac{\mathbf{1}}{\mathbf{2}}} \qquad \text{Eq. } \mathbf{B.8}$$

Appendix C

The *R* Dependence of the Coupling

This Appendix provides the motivation for the form of the coupling given in Eq. **74** in chapter 4, Eq. **90** in chapter 5 and Eq. **112** in chapter 6. The PCET nonadiabatic coupling $V_{\mu\nu}$ can be approximated as the product of a constant ET coupling V^{ET} and the overlap $S(R)$ between the reactant and product proton vibrational wavefunctions, shown in Eq. **C.1**

$$V(R) \approx V^{\mathrm{ET}} S(R). \qquad \text{Eq. } \mathbf{C.1}$$

For a simple model based on two ground state harmonic oscillator wavefunctions with centers separated by *R*, the overlap has the form given in Eq. **C.2**

$$S(R) \approx \exp\left[-\alpha\left(R - R^{*}\right)^{2}\right], \qquad \text{Eq. } \mathbf{C.2}$$

where R^{*} is the distance at which both reactant and product PT potentials become single wells centered at the middle of the PT interface and the overlap between the wavefunctions reaches its maximum value. We define $\overline{R}$ to be the equilibrium value of the *R* coordinate on the reactant surface, where $\overline{R} > R^{*}$. Note that the coupling in Eq. **74** in chapter 4 is given in terms of $\delta R = R - \overline{R}$, where $\overline{R}$ is the equilibrium value of the *R* coordinate on the reactant surface, and typically $\overline{R} > R^{*}$.

Eq. **C.2** can be rewritten as Eq. **C.3** .

$$\begin{aligned} S(R) &\approx \exp\left[-\alpha\left(R-\bar{R}-R^{*}+\bar{R}\right)^{2}\right] \\ &= S\left(\bar{R}\right)\exp\left[-\alpha'\,\delta R-\alpha\,\delta R^{2}\right] \end{aligned} \qquad \text{Eq. } \mathbf{C.3}$$

where $\alpha' = 2\alpha\left(\bar{R}-R^{*}\right)$. To first order in δR, the overlap becomes Eq. **C.4** .

$$S(R) \approx S\left(\bar{R}\right)\exp\left[-\alpha'\,\delta R\right], \qquad \text{Eq. } \mathbf{C.4}$$

which leads to the form of the coupling given in Eq. **74** in chapter 4

Appendix D

Supporting Information for Chapter 6

This appendix shows figures, equations, results and input quantities not given in chapter 6 of this thesis.

	Fe(III)	Fe(II)
Equilibrium Distances (Å):		
Fe – His499 Nε2	2.16	2.18
Fe – His504 Nε2	2.14	2.19
Fe – His690 Nε2	2.18	2.14
Fe – Asn694 Oδ1	2.18	2.22
Fe – Ile839 O1	2.05	2.23
Fe – Wat842 O	1.86	2.17
Experimental Force Constants (kcal/mol-Å^2):		
$Fe(H2O)_6$	366	230
$Fe(NH3)_6$	232	148

Table **D.1**: DFT B3LYP results for the Fe-ligand distances and experimental force constants calculated by Ref. 38 in Chapter 6.

	278K	**283K**	**288K**	**298K**	**303K**	**308K**	**313K**
Experiment[a]	98.73	92.44	90.4	76.23	80.69	65.51	71.10
Theory (GS)[b]	132	124	116	101	94	88	82
Theory[c]	105	96	88	74	68	62	57

Table **D.2:** The temperature dependence of the KIE for the temperature range 278K – 303K. a Experimental data from Ref. 9 in Chapter 6. b Theoretical calculations include only the contributions from the ground reactant and product vibronic states calculated from the numerical integration of the probability flux in conjunction with Eqs. **115** and **117**. c Theoretical calculations include the contributions from both ground and excited reactant and product vibronic states calculated from the numerical integration of the probability flux in conjunction with Eqs. **115** and **117**.

The expression for $C_R(t)$ as an undamped quantum harmonic oscillator is given in Eq. **D.1**

$$C_R(t) = \frac{\hbar}{2M\Omega}\left[\coth\left(k_B T/2\hbar\Omega\right)\cos\Omega t + i\sin\Omega t\right]. \qquad \text{Eq. D.1}$$

An analytical expression for the nonadiabatic rate constant can be derived using the above approximation for $C_R(t)$ in Eq. **D.1** and by using the approximation for the solvent damping term of the probability flux correlation function given in Eq. **115** in chapter 6. The rate expression shown in Eq. **D.2** is similar to that given in Eq.**119** in chapter 6

$$k = \sum_\mu P_\mu \sum_\nu \left|V^{\mathrm{el}} S^{(0)}_{\mu\nu}\right|^2 \exp\left[\frac{\hbar^2\alpha^2_{\mu\nu}}{M\Omega^2}\coth\left(\frac{\Omega}{2k_B T}\right)\right]\sqrt{\frac{2\pi}{\left(2\lambda_z k_B T + \lambda_\alpha \Omega\coth\left(\frac{\Omega}{2k_B T}\right)\right)}}$$
$$\times\exp\left[-\frac{\left(\Delta G^0 + \lambda_z + \lambda_\alpha\right)^2}{4\lambda k_B T + 2\lambda_\alpha\Omega\coth\left(\frac{\Omega}{2k_B T}\right)}\right], \qquad \text{Eq. D.2}$$

where λ_z is the solvent reorganization energy and $\lambda_\alpha = \frac{\hbar^2\alpha^2}{2M}$. Numerical integration of the probability flux correlation function using the approximations in Eq. **D.1** and Eq. **115** in chapter 6 leads to the following results illustrated in Figure **D.1**. The mass and frequency are calculated by using Eq. **117** in chapter 6 to match the time-dependence of $C_R(t)$ calculated from the molecular dynamics simulations. The mass is 14 amu and the frequency is 353 cm^{-1}. Also in Figure **D.1**, the results from the analytical expression given in Eq. **D.2** are shown. In Figure **D.1** only the excited state results are shown. Using the mass and frequency obtained from the approximation of the classical undamped harmonic oscillator as inputs into the quantum undamped harmonic oscillator

approximation can be viewed as adding a quantum correction to the classical approximation.

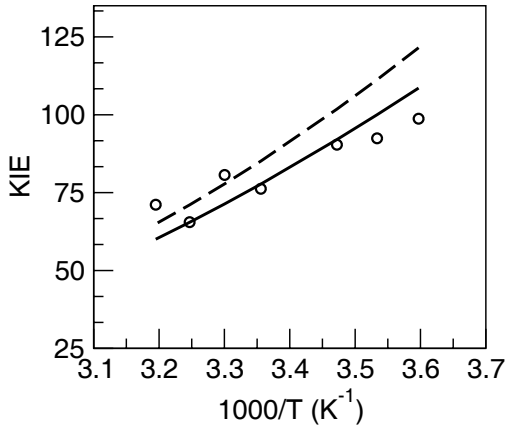

Figure **D.1**: Temperature dependence of the KIE obtained with the rate expression in Eq. **D.2** (solid line) and by numerical integration of the probability flux correlation function given in Eq. **113** in chapter 6 in conjunction with the approximations in Eq. **D.1** and Eq. **115** in chapter 6 where $M = 14\,\text{amu}$ and $\Omega = 353\,\text{cm}^{-1}$. The experimental data are depicted with circles.

VITA

Elizabeth Rose Hatcher

Born: December 28th 1979

Education: B.S. from Ohio State University in June 2001

Publications:

- Hatcher, E., Soudackov, A., Hammes-Schiffer, S., "Proton–Coupled Electron Transfer in Soybean Lipoxygenase", *Journal of American Chemical Society*, **2004**, 126, 5763 – 5775
- Soudackov, A., Hatcher, E. , Hammes-Schiffer, S., "Quantum and Dynamical Effects of Proton Donor–Acceptor Vibrational Motion in Nonadiabatic Proton–Coupled Electron Transfer Reactions", *Journal of Chemical Physics*, **2005**, 122, 014505
- Hatcher, E., Soudackov, A., Hammes-Schiffer, S., "Comparison of Dynamical Aspects of Nonadiabatic Electron, Proton, and Proton–Coupled Electron Transfer Reactions", *Chemical Physics*, **2005**, 319, 93 – 100
- Hatcher, E., Soudackov, A., Hammes-Schiffer, S., "Nonadiabatic Proton-Coupled Electron Transfer Reactions: Impact of Donor-Acceptor Vibrations, Reorganization Energies, and Couplings on Dynamics and Rates", *Journal of Physical Chemistry B.*, **2005**, 109, 18565 – 18574
- Hatcher, E., Soudackov, A., Hammes-Schiffer, S., "Proton-Coupled Electron Transfer in Soybean Lipoxygenase: Dynamical Behavior and Temperature Dependence of the Kinetic Isotope Effects", *submitted.*